Title	Short-term flow variations under the control of basal conditions in a temperate valley glacier
Author(s)	SUGIYAMA, Shin; 杉山, 慎
Degree Grantor	北海道大学
Degree Name	博士(地球環境科学)
Dissertation Number	甲第6481号
Issue Date	2003-03-25
DOI	https://doi.org/10.14943/doctoral.k6481
Doc URL	https://hdl.handle.net/2115/28088
Type	doctoral thesis
File Information	thesis.pdf

Short-term flow variations under the control of basal conditions in a temperate valley glacier

SUGIYAMA Shin

Ph. D. dissertation

Graduate School of Earth Environmental Science
Hokkaido University

February, 2003

ABSTRACT

This thesis studies how a temperate valley glacier flows under the control of basal conditions. To investigate the influence of basal conditions on the glacier flow field, field measurements were carried out with high temporal resolutions at Lauteraargletscher in the Swiss Alps during the ablation season. The measurements and subsequent data analyses focus on the relationship between surface velocity and subglacial water pressure, surface vertical movement (uplift), and temporal variations in vertical strain. A glacier flow model is developed to study general effects of basal perturbation on the flow field, and is used to interpret the observed short-term flow variations.

Clear diurnal variations in surface velocity were observed in the mid ablation season, and the velocity was correlated with subglacial water pressure during this period. The glacier was accelerated significantly when the water pressure raised up close to the overburden pressure. Detailed examination of the relationship showed that the velocity is larger when the pressure increases than it decreases under the identical water pressure. This hysteresis is understood as the result of pushing force conveyed through ice from a few kilometers upper reach of the glacier.

Diurnal variations were also found in vertical strain, which was tensile during the daytime and compressive during the nighttime with an order of 10^{-4}. This observation implies that the glacier flow regime switched from extending to compressive flow in a diurnal manner. Non-uniformly distributed basal lubrication and its diurnal evolution can cause such change in the flow regime. The short-term variations in vertical strain and the hysteresis in surface velocity indicate that the glacier flow is not a local phenomenon, but influenced by neighbouring flow conditions.

Uplifts were frequently observed with surface velocity variations. Surface vertical displacement was compared with vertical strain to determine the mechanism of the uplifts, and it was concluded that vertical straining was the major cause in most cases. However, a sudden upward movement measured at a motion event cannot be ascribed to vertical strain, and volume increase in subglacial water cavities is a plausible reason of the uplift.

General effects of spatially limited basal perturbation on the flow field was investigated with a finite element flow model. Transmission of basal motion to the surface through non-linear viscous material (ice) was computed by numerical experiments. It was shown that the rate of the transmission is dependent on the spatial scale of the basal perturbation. The experiments also showed that the influence of local basal motion can reach a horizontal distance of 10 times ice thickness.

The relationship between surface velocity and water pressure was simulated including the effect of spatially distributed basal lubrication. The observed velocity hysteresis was reproduced by allocating more lubricated bed condition in the upper reach of the glacier. The diurnal vertical strain was also reproduced qualitatively by assuming diurnal evolution of a basal slippery zone.

The field measurements show that subglacial water pressure controls short-term flow variations in temperate valley glaciers. Furthermore, detailed examinations of the data insist that the flow of a glacier is not determined by local water pressure alone, because the influence of neighbouring basal condition cannot be neglected. Numerical investigations also confirm the importance of basal lubrication in up- and downglacier areas to compute a flow field. Therefore, the mechanical interaction with surrounding ice mass should be taken into account, when glacier flow variations under the control of basal conditions are discussed.

CONTENTS

LIST OF FIGURES

LIST OF TABLES

CHAPTER 1

GENERAL INTRODUCTION

1.1 Glacier Flow Mechanisms and Basal Processes

Glaciers flow with two mechanisms, internal ice deformation and basal motion. Owing to its viscous nature, ice deforms as a consequence of gravity acting on itself. On the other side, glaciers flow near the bed by various processes when the bed is lubricated with melt water. Here, the term *basal flow* or *basal motion* is used to represent all the basal processes which move glacier ice forward. Basal motion takes a dominant role in intra-annual flow variations of a temperate glacier. This is because basal flow velocity is expected to fluctuate as a result of the changes in the conditions at the glacier bed such as, water pressure variations, changes in properties of sediments, evolution of the hydraulic system. These conditions are not spatially uniform within a glacier and temporally fluctuate in a relatively short time when the glacier is subjected to seasonal ablation. Accordingly, glacier flow variations during the ablation season are not predictable, and it is not well understood how they are controled by basal conditions. Not only in valley glaciers, basal motion crucially contribute to the dynamics of Antarctic and Greenland ice sheets as well. Therefore, it is one of the major subjects in the current glaciology to understand the basal flow processes and how it influences the overall glacier flow.

Basal processes have been studied theoretically since Weertman (1957) proposed the first model of ice sliding on a temperate bedrock. He formulated a sliding law by taking pressure melting and refreezing (regelation) and creep enhancement as the mechanisms of sliding over basal obstacles. Among the important analytical studies on the sliding over a periodically wavy bedrock (Lliboutry, 1968; Nye, 1969; Kamb, 1970), Lliboutry introduced the formation of basal water cavities. In his theory, ice sole separates from the bed at the lee side of a bedrock bump when the ice glides over the bump. Basal stress concentrates on the upstream side of the bump consequently, and it enhances ice deformation. This process is further studied by numerical modeling (Iken, 1981), and basal sliding laws with taking into account of cavity formation have been proposed (Schweizer and Iken, 1992; Truffer and Iken, 1998). One of the key findings in the field of glacier dynamics is the deformation of subglacial sediments. Boulton and Hindmarsh (1987) proposed a new process of glacier flow based on their observation under a glacier. When a glacier is underlained by an unlithified sediment layer, the sediment layer may deform and carry the ice mass on it forward. Iverson and others (1995) measured shear strain rate and strength of the sediment layer under Storglaciären in Sweden, and the results showed distinctive basal flow regime which is specific to a glacier on a soft bed. Sediment deformation drew an attention in connection with the ice streams in the West Antarctica. After a seismic sounding study suggested the existence of a thick water saturated sediment layer under Whillans Ice Stream (Blankenship and others, 1986), bed conditions of ice streams have been intensively studied. Based on the direct observation in bottom reaching boreholes (Engelhardt and Kamb, 1997, 1998; Tulaczyk and others, 2000a, b; Kamb, 2001), it has been shown that basal flow is dominant in streaming flow and mechanical properties of the sediments take a key role in the basal flow process.

There are many basal flow processes, and most of them are controlled by subglacial water and its pressure. The most essential example is the reduction of the friction at the ice-bed boundary, which is expected when water submerges small obstacles on the bed. Water cavity formation and its sustainability are also controled by water pressure. Once a water cavity is formed, water pressure is considered to push the ice sole forward with hydraulic-jack effect (Röthlisberger, 1981). In a water saturated sediment layer, porosity and pore water pressure are important variables to determine mechanical properties of the layer (Iverson and others, 1998, 1999; Tulaczyk and others, 2000a). Tulaczyk and others (2000a, b) studied the effects of water on mechanical properties of sediments retrieved from the bed of Whillans Ice Stream, and argued that the basal melt rate switches on and off the streaming flow of the ice stream. In general, basal flow is enhanced by high water pressure through bed lubrication, water cavity formation, hydraulic-jack effect, and weakening of a subglacial sediment layer.

1.2 Short-term Flow Variations in Temperate Valley Glaciers

Because of the influence of melt water on basal motion, flow velocity of temperate glaciers varies significantly during the ablation season (summarized in Willis, 1995). More than 100-200% increase in the surface velocity within a day or less is often observed on temperate valley glaciers. Some of them are triggered by sudden water input due to a rainstorm or drainage of a supraglacial lake (Nolan and Echelmeyer, 1999), and others are presumably caused by the surface melt condition most frequently in early spring (Iken and Bindschadler, 1986; Gudmundsson, 2002; Mair and others, 2001, 2002) but also in other times in the ablation season (Naruse and others, 1992; Bassi, 1999; Gudmundsson and others, 2000). Such speed up is called in different ways as, *motion event* (Gudmundsson, 2002), *speed up event* (Truffer and others, 2001), *spring event*, *high-velocity event* (Mair and others, 2001, 2002) or *mini surges* (Kamb and Engelhardt, 1987; Raymond and Malone, 1986). Because all these phenomena are sudden changes in glacier motion which are intrinsically originated from the common cause (basal water condition), hereafter they are referred to as a *motion event* without regard to the season or the source of water input to avoid confusion. Not only at motion events, temperate glaciers change their flow velocity over various time scales from a day to months. These velocity changes often have a correlation with surface melt rate or precipitation, and the subglacial drainage condition also concerns with the flow variations. It has been suggested from field observations that subglacial water pressure takes an important role in short-term flow variations.

The relationship between subglacial water pressure and surface velocity is studied in several glaciers. Iken and Bindschadler (1986) measured surface velocity several times a day with subglacial water pressure at Findelengletscher in Switzerland. They plotted surface velocities against water pressure, and found that the velocity increases as the pressure rises up. In their plot, surface velocity appears to have an asymptote at the water pressure equal to the ice overburden pressure. Jansson (1995) made similar measurements at Storglaciären in Sweden, and also found velocity increase under high water pressure condition. He applied a power function to the data from Findelengletscher and Storglaciären to get an empirical relationship between the velocity and pressure. Measurements at Variegated Glacier in Alaska by Kamb and Engelhardt (1987) have slightly different background, because they were conducted on a surging-type glacier within a few years before it surged. Water pressure dependence of the surface velocity at Variegated Glacier was similar to those at Findelengletscher, except the water pressure often rose above the overburden pressure. The results obtained in the three glaciers agree in terms of two characteristics. Surface velocity increases nonlinearly as subglacial water pressure rises up, and the velocity increase is significant when the pressure approaches to the overburden pressure. Although a general feature of the relationship between water pressure and glacier flow is shown by these studies, detail of the relationship is not clear because the measurement intervals are rather long. Flow velocity measurement with higher temporal resolution for a longer period is needed for further investigation, but such measurement is difficult to achieve with traditional instruments such as a theodolite or an electric distance meter.

Another important aspect of short-term flow variation in temperate glaciers is vertical movements of the surface. Iken and others (1983) measured the horizontal and vertical displacement of stakes on Unteraargletscher in Switzerland with intervals down to a few hours. The glacier surface moved upward by 150 mm when horizontal velocity increased, and this incidence was called *uplift*. They proposed an idea that the uplift was caused by volume increase of subglacial water cavities. Detailed examination showed that the highest horizontal velocity was obtained when the rate of elevation increase took its maximum rather than the elevation itself. This observation conforms to the theoretical prediction, because Iken's (1981) numerical investigation showed that the rate of cavity volume increase is more relevant to the basal flow velocity rather than the volume itself. Similar uplift is also observed by Kamb and Engelhardt (1987) at Variegated Glacier during motion events. Glacier surface motion in the vertical direction can be understood as a consequence of elevation change of the glacier sole and/or thickness change of the ice. Among the factors which may induce these two changes, substantial contribution is expected from vertical strain of ice because strain rate regime can be altered during a motion event. Therefore, vertical strain over the ice thickness should be measured to determine the cause of uplift, but very few measurements have been carried out with sufficiently high temporal resolution (Gudmundsson, 2002; Harrison and others, 1993).

1.3 Influence of Basal Motion on the Glacier Flow Field

Short-term flow velocity variations observed on the surface are caused by variations in basal motion, but one must be aware that the surface observation collects information transfered from the bed to the surface through ice. Because ice flows as a viscous material, basal motion diffuses away from the point to the surrounding area and only a part of the motion reaches the surface. Correspondingly, basal velocity at a point cannot be determined from surface observations even if the basal conditions at that point are well specified. When the bed is partly lubricated, basal stress at the point is reduced and transfered to other regions of the bed to support the total gravitational force acting on the glacier. Consequently, stress increases at some other regions and it enhances ice deformation there. This deformation controls the basal flow at the lubricated region through stress coupling of ice. These processes indicate that basal flow velocity at a point is determined by the enhanced deformation nearby and the stress transfered from the surrounding ice mass by mechanical coupling. Therefore, the influence of basal conditions on glacier flow cannot be local, but spatial distribution of the conditions determines the flow field of a glacier.

The foregoing idea is well accepted in glaciology, but clear observation of the internal glacier flow field under the influence of basal motion are missing, because of the difficulty of flow measurements within a glacier. Borehole tilt measurement is one of the means to obtain internal velocity (Raymond, 1971; Copland and others, 1997; Harper and others, 1998), but temporal resolution of the measurement is usually more than a week. Basal flow velocity has been directly measured in boreholes using a drag spool (Blake and others, 1994; Engelhardt and Kamb, 1998) or a video camera (Pohjola, 1993), but such measurements are still limited to a few glaciers and the interpretation of data taken under a glacier is not straightforward. Therefore, short-term flow variations have been observed mostly on the surface of glaciers, and a high resolution measurement within a glacier is demanded.

Theoretical investigation is an alternative approach to study the influence of basal motion on the flow field. Balise and Raymond (1985) studied two dimensional flow fields with perturbed basal motion in different spatial scales. Although their analytical solution is restricted to a Newtonian fluid, it was clearly shown that the propagation of basal motion to the surface is strongly dependent on the length scale of the perturbation. Perturbation analysis was also applied to non-linearly viscous glaciers by Bahr and others (1994) to evaluate the accuracy of the calculation of englacial velocity distribution from surface observations. They concluded that the errors in calculated englacial velocities increase at an exponential rate with depth, which hinders the calculation of basal perturbation with wavelength less than the ice thickness. It implies that short-length scale information at the bed is filtered out and not able to appear on the surface. The transmission of slipperiness and topographic anomaly from the bed to the surface was further studied by Gudmudsson and others (Gudmundsson and others 1998; Gudmundsson, 2003). His method was used to interpret the stripe observed on the surface of an ice stream in Antarctica, and can be a strong tool to deduce the bed condition from surface observations. Blatter and others (Blatter, 1995; Blatter and others, 1998) developed a numerical scheme to introduce higher order stress components into non-Newtonian flow, and computed glacier flow field on a partly sliding bed. This scheme was utilized to simulate three-dimensional flow field measured in Haut Glacier d'Arolla, Switzerland (Hubbard and others, 1998), and the prescribed basal boundary condition is discussed with the subglacial water pressure distribution. All these previous studies indicate that the inclusion of longitudinal deviatoric stress components is necessary in glacier flow modelling to deal with a spatially non-uniform basal condition unless the horizontal length scale is much larger than the ice thickness.

1.4 Objectives of This Study

The objective of this study is to find the cause and the physical process of short-term flow variations in temperate valley glaciers. This objective is achieved by field measurement and numerical investigation.

In the observational part, measurements are carried out with high temporal resolution during the ablation season at Lauteraargletscher, a temperate valley glacier in Switzerland. Specifically, objectives of the measurements are to obtain clear observational data for the following three items.

(1) Relationship between surface flow velocity and subglacial water pressure

(2) Vertical movement of the glacier surface (uplift)

(3) Temporal variations in the vertical strain within a glacier

Hourly surface velocities are compared with subglacial water pressure to obtain their relationship with regard to the overburden pressure. The possibility of subglacial water cavity opening is discussed by comparing vertical strain with surface uplift. From the vertical strain measured at different depths, vertical distribution of the strain and its temporal variation are computed. The results obtained in the field measurements are combined to hypothesise about the cause and process of the short-term flow variation.

In the theoretical part, flow fields in a longitudinal cross section of a conceptional glacier are computed with prescribed basal boundary conditions with a numerical flow model. The model is used to investigate the general pattern of the flow field under the condition of spatially non-uniform basal motion. Then, the measured short-term flow variations are simulated with the model by prescribing spatial distribution and temporal variation of basal lubrication in order to test the hypothesis proposed for the field data. The numerical experiments give an insight into the effects of spatially distributed basal slipperiness on the flow field.

CHAPTER 2

FIELD MEASUREMENTS

In order to study the influence of the basal condition on the glacier flow field, measurements were made on (flow velocity), within (vertical strain), and under (water pressure) a temperate valley glacier. The measurements were performed with high temporal resolution, so that the reaction of the glacier flow to rapid changes in water pressure can be detected. This field study mainly focuses on intradaily flow variations, but the observations made throughout the ablation season are expected to show seasonal changes in the flow regime and the basal condition.

2.1 Study Site

The field measurements were carried out at Lauteraargletscher, one of the constituents of a valley glacier system in the Bernese Alps, Switzerland (Fig. 2.1a). Lauteraargletscher is about 5 km long, 1 km wide, and considered to be temperate according to temperature measurements in other glaciers in the Alps. It originates at 3100 m a.s.l., and merges with Finsteraargletscher at 2400 m a.s.l. into the common tongue of the glacier system, Unteraargletscher. From the confluence area, Unteraargletscher descends 6 km eastwards and terminates at 2000 m a.s.l.. Including the other tributary, Strahlegggletscher, the glacier system has a surface area of 28 km^2 in total.

The history of glaciological study in this region goes back to the 19th century. Following the pioneering works by Hugi and Agassiz (1840), systematic glacier measurements have been carried out since the early 20th century by requests of a hydroelectric power company. In terms of the dynamic behaviour of the glacier, intra annual variations in the surface velocity were already recognized in the early measurements with an automatic camera (Haefeli, 1970), and recent studies on Unteraargletscher revealed details of subdaily flow variations. Iken and others (1983) carefully measured survey poles on the glacier several times a day during a motion event in early summer, and studied surface upward movement associated with fast flow velocity. Observations with an automatic theodolite system showed that motion events usually occur several times in the ablation season on Unteraar- and Lauteraargletscher (Bassi,

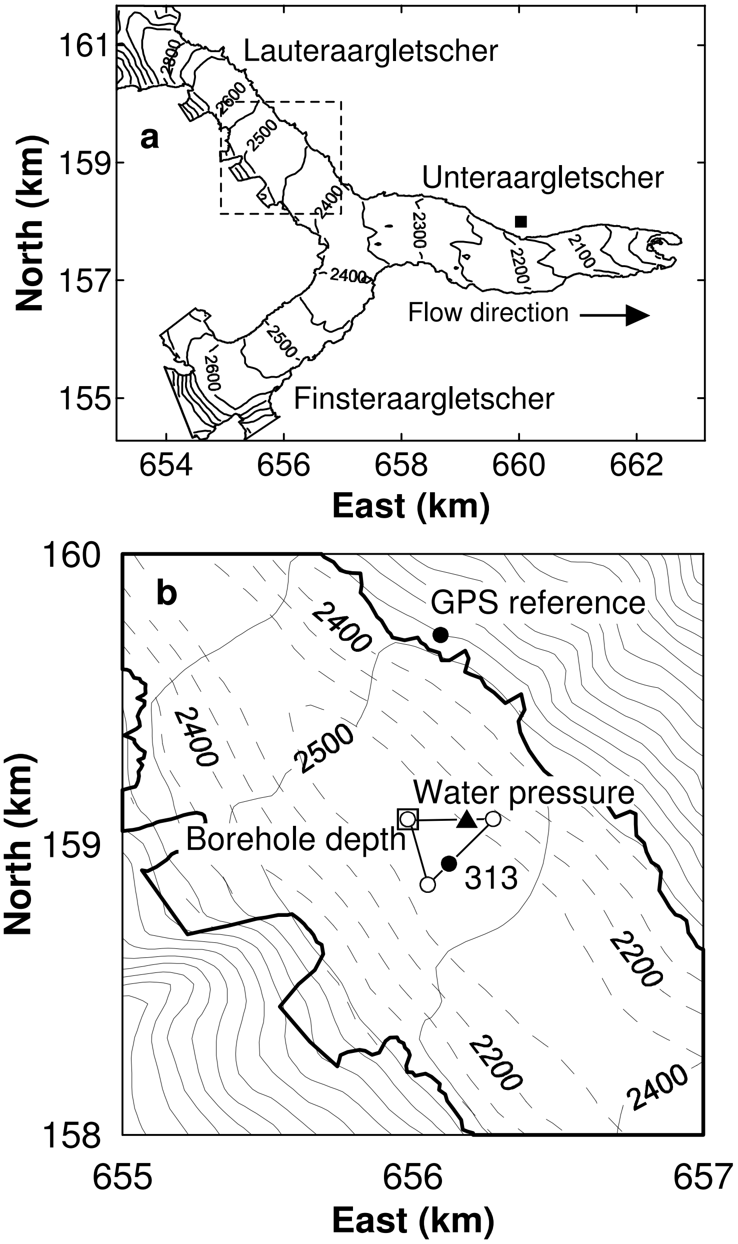

Figure 2.1: *(a) Map of Unteraargletscher and its tributaries. The solid square is the location of the meteorological station. (b) The study area on Lauteraargletscher (smaller square in (a)). Solid and broken contour lines indicate the surface and bed topography, respectively. Elevations are in meters above sea level. Solid circles are positions of a pair of GPS antennas for continuous measurement of surface flow. Open circles connected with solid lines are the strain array, the open square is the location of the boreholes, and the solid triangle is the location of the water pressure measurements. Coordinates correspond to the official Swiss coordinate system.*

1999; Gudmundsson and others, 2000). Gudmundsson and others (1999) estimated the basal motion at the middle part of Unteraargletscher as more than 50% of the total forward motion from tilt measurements in a borehole.

Ice thickness and basal conditions of the glaciers have been studied by seismic reflection and radio-echo soundings (Knecht and Süsstrunk, 1952; Funk and others, 1994; Bauder, 2001). The results indicate that Unteraargletscher is underlain by a sediment layer. Fischer and others (2001) performed stress measurements in the sediment layer to discuss its hydraulic and mechanical properties. The layer gets thinner in the upglacier direction and disappears at the confluence area implying a hard bed condition under Lauteraargletscher.

From June to October 2001, a camp was set on Lauteraargletscher to drill boreholes and conduct glacier flow measurements. Apart from meteorological observation, all measurements were made on Lauteraargletscher at an altitude of 2480 m a.s.l.. Maximum ice thickness at the measurement site is estimated to be 400 m by radio-echo sounding (Funk and others, 1994; Bauder and others, 2002), which was confirmed by the drilling down to the bed. In contrast to Unteraargletscher, where a thick debris layer covers nearly 70% of the surface (Sugiyama, 2003), Lauteraargletscher has an almost clean surface. Crevasses are observed only near the lateral margins, and the surface is fairly flat with a slope of 4 ° at the study site. The seasonal snow line passed by the camp in late July and the snow line altitude at the end of the ablation season was approximately 2600 m a.s.l. in 2001.

2.2 Methods

2.2.1 GPS survey

A 6 m long aluminum pole was installed into the glacier surface at the site 313 (Fig. 2.1), and three-dimensional position of the pole was determined using static relative GPS measurements (Hofmann-Wellenhof and others, 2001). One of the GPS receivers (TOPCON GP-SX1) was fixed at the top of the pole and the other one on the north flank of the glacier as a reference station. L1 phase signals from GPS satellites were continuously collected by the receivers and stored in data loggers to obtain hourly positions of the pole relative to the reference station by using commercial software (TOPCON WAVE).

Strictly speaking, the GPS measurement in this study gives the position of a particle of ice near the glacier surface in a frame fixed outside of the glacier. Therefore, *surface velocity* or *surface displacement* refers to the movement of the particle near the surface, and surface melting is not relevant to the discussion of the vertical displacement in this study.

The distance between the two receivers was 700 m in horizontal and 100 m in vertical direction, and this relatively short distance was crucial to obtain the necessary accuracy of the GPS measurement. The accuracy was evaluated after the field season by using the same survey method with two fixed receivers standing apart 120 m horizontally and 12 m vertically.

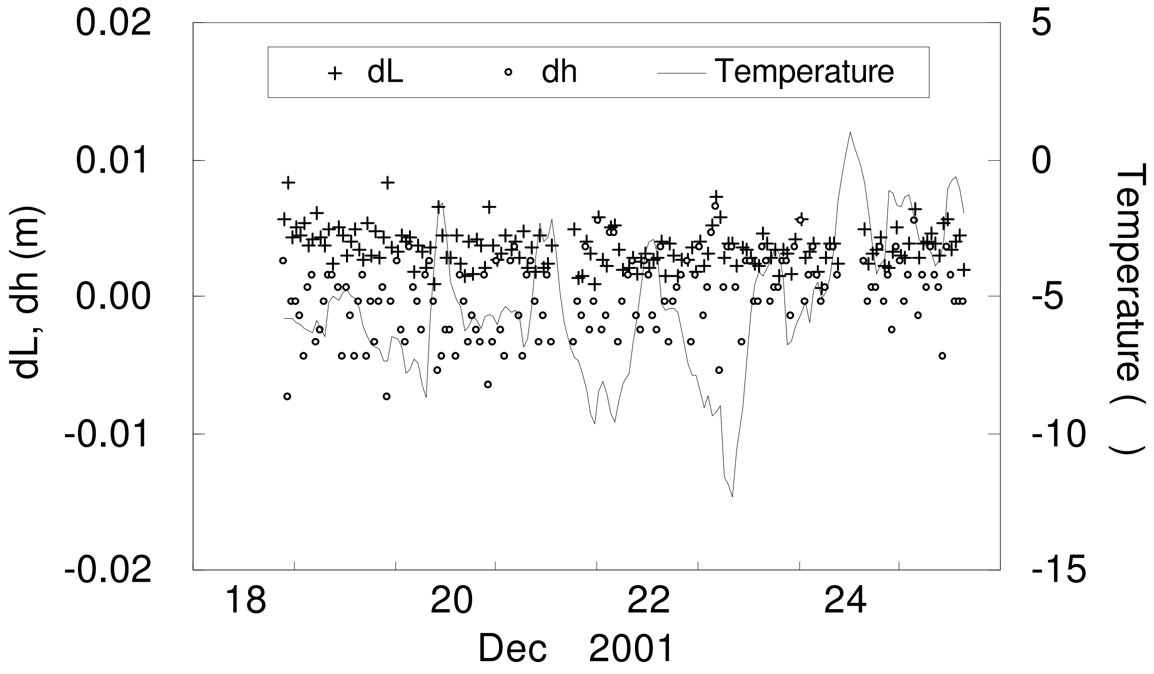

Figure 2.2: *The accuracy test of GPS measurement. A fixed receiver was surveyed for 7 days with static relative measurements. Horizontal distance (cross) and vertical displacement (open circle) relative to the 7 days mean position are plotted every hour.*

Continuous test measurements for 7 days gave standard deviations of 1.4 mm and 2.8 mm in horizontal and vertical directions, respectively (Fig. 2.2). On the glacier, the survey pole froze in the ice immediately after the installation because winter coldness keeps the subsurface ice temperature below the melting point throughout the year. In addition, the length of the pole above the surface was maintained to be shorter than 1.5 m. Accordingly, measurement errors due to the leaning of the pole by ice melting or wind blowing are considered to be negligible.

Hourly surface flow velocity in the horizontal direction was calculated from a four-hours running mean of the horizontal displacement of the pole from its original position on 15 June 2001. When the continuous survey was interrupted for a few hours, the data gaps were interpolated by spline interpolation. In addition to the continuous measurement at the site 313, twice a day (within 2-hrs of 6:00 and 18:00) from 22 to 27 August, the positions of three other poles forming a triangle with sides of about 300 m (strain array in Figure 2.1b) were surveyed. These surveys are used in the section 3.2 to examine the horizontal surface strain pattern.

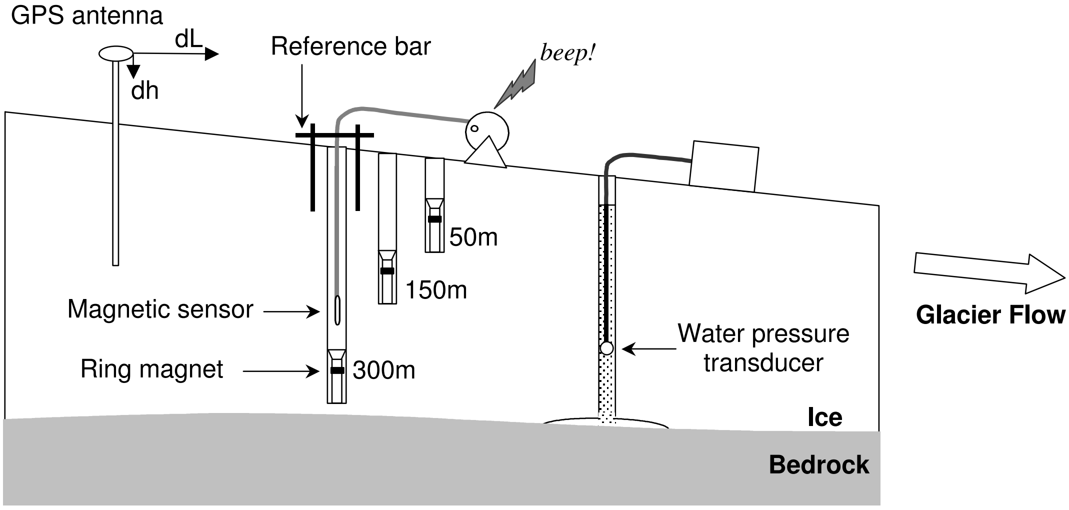

Figure 2.3: *Schematic diagram of the field measurements.*

2.2.2 Borehole depth

Vertical strain was measured by repeated high-accuracy borehole depth measurements (Gudmundsson and others, 1997; Gudmundsson, 2002; Sugiyama and Gudmundsson, 2003). A hot water technique (Iken, 1988) was used to drill 50, 150, and 300-m deep boreholes of about 100-mm diameter with roughly 5-m spacings. A 1-m long, 64-mm diameter plastic pipe with a 12-mm thick ring-shaped magnet on its upper rim was placed at the bottom of each borehole. A metal weight was fixed to the plastic pipe with a string to lower the equipment smoothly down to the bottom of the borehole, and it was removed after the installation by cutting the string to prevent pressure melting due to its own weight at the lower edge of the pipe. The distance from the magnets to the reference bars drilled into the surface ice directly above each of the boreholes was measured 1-8 times a day with a measuring tape equipped with a magnetic sensor on its end. When the magnetic sensor was lowered into the bottom of the borehole, a signal indicates the position of the ring magnet and the distance from the magnet to the reference bar was read by the measuring tape. The schematic diagram of the borehole depth measurement is shown in Figure 2.3, and the instruments of the measurement and the way of reading the depth at the reference bar are shown in Figure 2.4. Judging from repeated measurements, and from daily inspection of the magnetic sensor using a 1-m deep borehole where no vertical stretching was expected, the measurement error was estimated to be ±3 mm. Elastic stretching of the measuring tape made of TEFLON is negligibly small and thermal expansion was ignored based on the stable temperature in the borehole at the ice melting point.

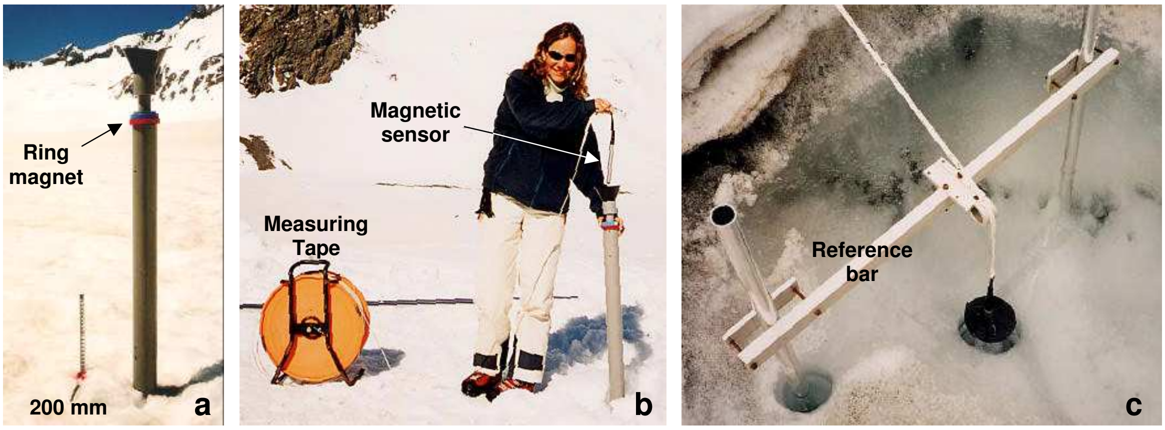

Figure 2.4: *The instruments of the borehole depth measurement. (a) A plastic pipe with a ring magnet installed in the borehole. (b) The plastic pipe and a measuring tape with magnetic sensor on its top. (c) The way of reading the depth at the reference bar fixed on the surface.*

Change in the distance between the magnetic ring in the borehole and the reference bar is a consequence of vertical normal strain and horizontal shear strain. Assuming a laminar flow with simple shear and Glen's flow law with an exponent parameter $n = 3$ (Paterson, 1994), the length of an originally vertical borehole deformed after a unit time is;

$$s = \int_{z_0}^{h} \sqrt{1 + \left(\frac{du}{dz}\right)^2} dz = \int_{z_0}^{h} \sqrt{1 + \left[\frac{d}{dz}\left\{u_s - u_s\left(\frac{h-z}{h}\right)^4\right\}\right]^2} dz, \tag{2.1}$$

where z is the vertical coordinate measured from the bed, u is the horizontal flow velocity, z_0 is the coordinate of the borehole bottom, u_s is the horizontal velocity on the surface, and h is the total ice thickness. The specific values at the study site of $h = 400$ m and $u_s = 0.1$ m day^{-1} give an extension rate of 4×10^{-6} m day^{-1} for 300-m borehole, which is smaller by three orders of magnitude than measured depth changes. Thus, we neglect the contribution of shear strain to the change in the borehole depth.

The 300-m borehole was closed in August at the depth of 170 m below the surface, possibly because the water level in the borehole was too low to counteract the hydrostatic pressure of ice. Without signals from the magnetic ring, borehole depth measurements were continued by feeling the decreased tension of the measuring tape when the sensor contacts to the pinched-off point in the borehole. The error of this measurement was estimated to be ±5 mm from repeated measurements.

2.2.3 Water pressure

Subglacial water pressure was registered every 15-30 minutes from 30 June to 28 September in 2001 with a vibrating wire pressure transducer lowered into a 380-m bottom-reaching borehole. The borehole was located about 200 m from the GPS and borehole depth measurement sites (Fig. 2.1b), and the pressure transducer was installed 100 m above the bed. Measurement accuracy of the transducer (Geokon Model 4500) is equivalent to the water level of 3.5 m.

Two more transducers were installed in two other bottom-reaching boreholes: one located at the borehole depth measurement site and the other near the right glacier margin. The water levels in the three boreholes fluctuated in phase, which indicates all the boreholes connected to a common subglacial drainage system. Because two of the boreholes were disconnected from the drainage system in the early August, the data obtained from the 380-m borehole is presented here.

2.2.4 Air temperature, precipitation, and surface ablation

A meteorological station was established on the left bank of Unteraargletscher at an altitude of 2400 m a.s.l. (Fig. 2.1a). Air temperature and precipitation were measured at intervals of 30 minutes from 12 June to 30 September. A ventilated thermistor sensor (Vaisala T107) and a tipping bucket rain gauge (Joss-Tognini) were used for the temperature and precipitation measurements, respectively. Surface snow or ice ablation was measured every one or two days by stake measurements at the GPS measurement site. The densities of 600 kg m^{-3} for snow and 900 kg m^{-3} for ice were used to obtain daily ablation in water-equivalent from the measurements.

2.3 Results

Continuous GPS survey and borehole depth measurements were carried out for 1-2 weeks in each month from June to September 2001. Figure 2.5 shows the movement of the survey stake in a vertical plane along the flow line, and horizontal flow velocity during the study period. The vertical motion of the stake was generally downward from June to October, but clear upward movements were observed in the measurements in June and July. Both of these uplift events were accompanied by sharp increases in the flow velocity. In this study, the details of these short-term fluctuations in the horizontal velocity and the vertical displacement obtained in the four measurement periods are focused on.

2.3.1 Period I (from 22 June to 5 July)

A series of data taken from 22 June to 5 July is shown in Figure 2.6. The snow line altitude was approximately 2400 m a.s.l. and the study site was still covered with 1 to 2 m of snow

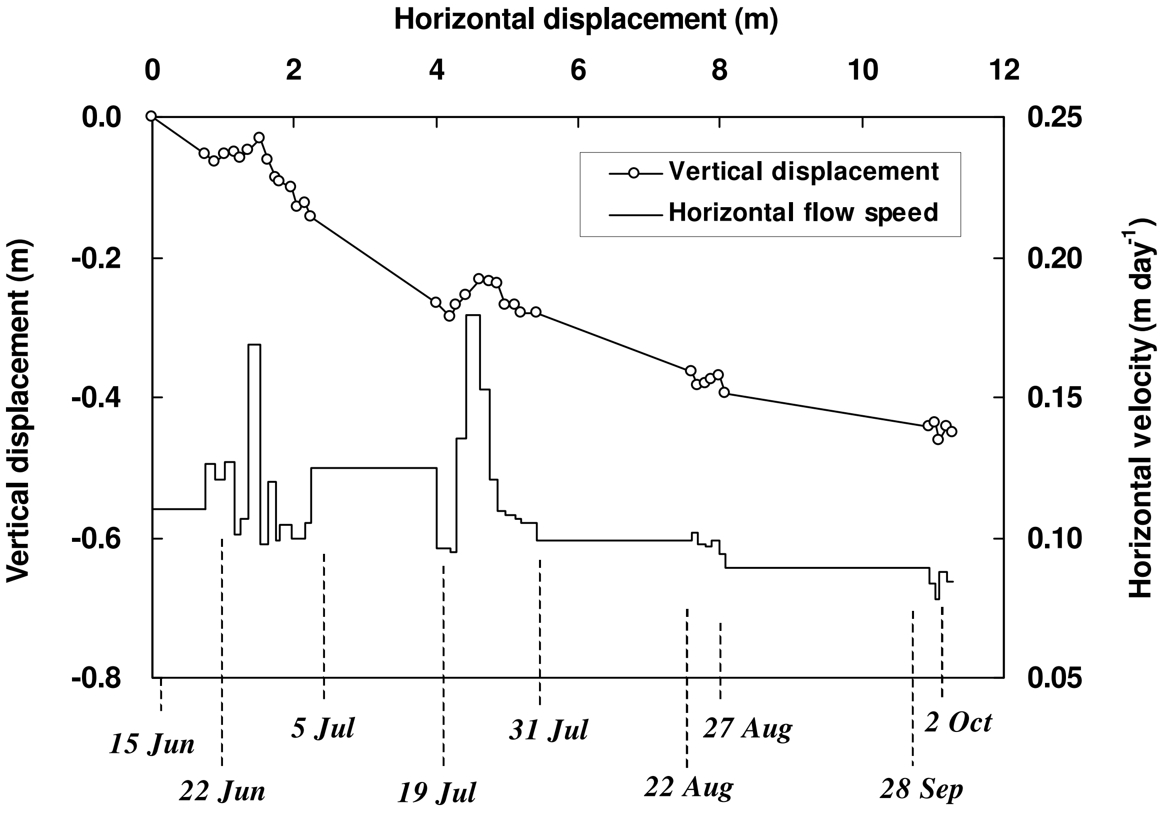

Figure 2.5: *Stake movement in a vertical plane (open circle) and horizontal surface flow velocity against horizontal displacement obtained by GPS measurement from 15 June to 2 October 2001.*

during this period.

After the period of fine weather with snow melt of 30-50 mm w.e. day^{-1}, heavy rainstorm started at 15:00 on 27 June and the precipitation reached 6.3 mm hr^{-1} at 18:00 (Fig. 2.6e). Horizontal flow velocity started to increase at 17:00 and the maximum velocity of 0.2 m day^{-1}, approximately 200% of the velocity before the storm, was recorded at 22:00 (Fig. 2.6b). When the flow velocity reached its maximum, the glacier surface rapidly moved 20 mm upward (Fig. 2.6a). It is inferred that the intense water input by the rainstorm raised subglacial water pressure and triggered a motion event accompanied by uplift of the glacier surface. On the next day, flow velocity returned to the pre-storm level and then remained there until the end of this observation period. Before the motion event, the vertical displacement remained at a constant level but increased a few centimeters around midnight every day. After the event, it started to decrease without diurnal signals.

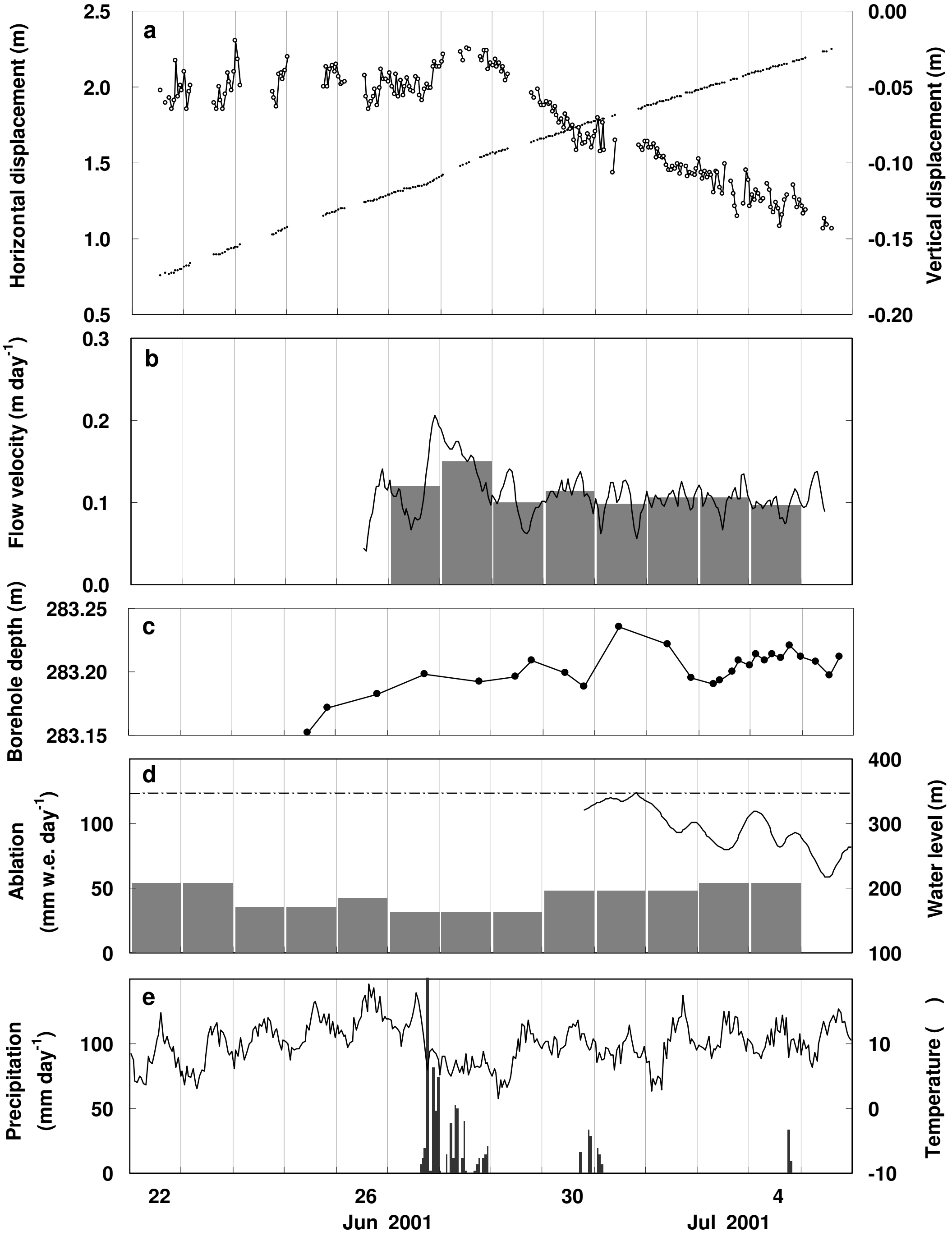

Figure 2.6: *Time series of data taken in Period I. (a) Horizontal (dot) and vertical displacement (open circle) of the stake from its original position on 15 June 2002. (b) Horizontal surface velocity (solid line) and its daily average. (c) Borehole depth. (d) Surface ablation and water level (solid line) in the borehole, and the dash-dotted line indicates the overburden pressure. (e) Air temperature (solid line) and precipitation.*

The borehole depth decreased at the motion event following the steady increase until 27 June (Fig. 2.6c). After the event, it showed irregular fluctuations represented by 50 mm deepening from 30 June to 1 July. This incident coincided with a surface uplift (Fig. 2.6a) and water level increase close to the overburden pressure (Fig. 2.6d).

2.3.2 Period II (from 18 to 31 July)

In the beginning of the second observation period, weather was cold with occasional snowfalls. Then on 21 July, daily mean air temperature rose up sharply by about 10 °C causing intense surface melting. The warm weather lasted and the daily ablation of 60-80 mm w.e. day^{-1} took place for ten days until the end of this observation period. The glacier surface condition turned from water saturated snow to bare ice, and many moulins opened in the study area.

Clear diurnal variations in the surface velocity were established as a result of substantial melt water input in the daytime (Fig. 2.7b). The maximum velocity occurred in the evening and the minimum velocity in the morning. On 23 and 24 July, the maximum velocity of a day was more than twice as large as the minimum. The diurnal velocity fluctuation became smaller on 26 July. Water level showed diurnal variations as well and its daily maximums coincided with flow velocity peaks. The maximum water pressures were more than the overburden pressure from 22 to 25 July, when the diurnal signal is clear in the velocity. These are strong implications of a correlation between surface velocity and subglacial water pressure. From 26 July to the end of this observation period, the amplitude of the diurnal signal in water level gradually increased while the daily mean level decreased. It should be noted that this change took place under the nearly constant ablation and meteorological condition.

The vertical displacement of the glacier surface appears to correlate with the borehole depth variation until 27 July (Figs. 2.7a and c). It is implied that the vertical displacement was predominantly caused by vertical straining. From 22 to 25 July, however, the surface is diurnally lifted up in the evening and this diurnal signal is not clearly seen in the borehole depth change. On 27 July, borehole depth started to show diurnal fluctuations by a magnitude of 10^{-4} of the ice thickness. This observation indicates that the glacier was thickening in the daytime and thinning at night.

2.3.3 Period III (from 22 to 27 August)

In the late August, the seasonal snow line was about 1 km upglacier from the study site. Fine weather caused steady surface ablation, a rate of 50 mm w.e. day^{-1}, and melt water was fed into moulins well developed at the study area.

Clear diurnal fluctuations in the surface velocity were again observed from 22 to 27 (Fig. 2.8b), but the amplitude of the fluctuation and the daily mean velocity were more uniform and at lower level than those observed in July. The water level changed more than 100

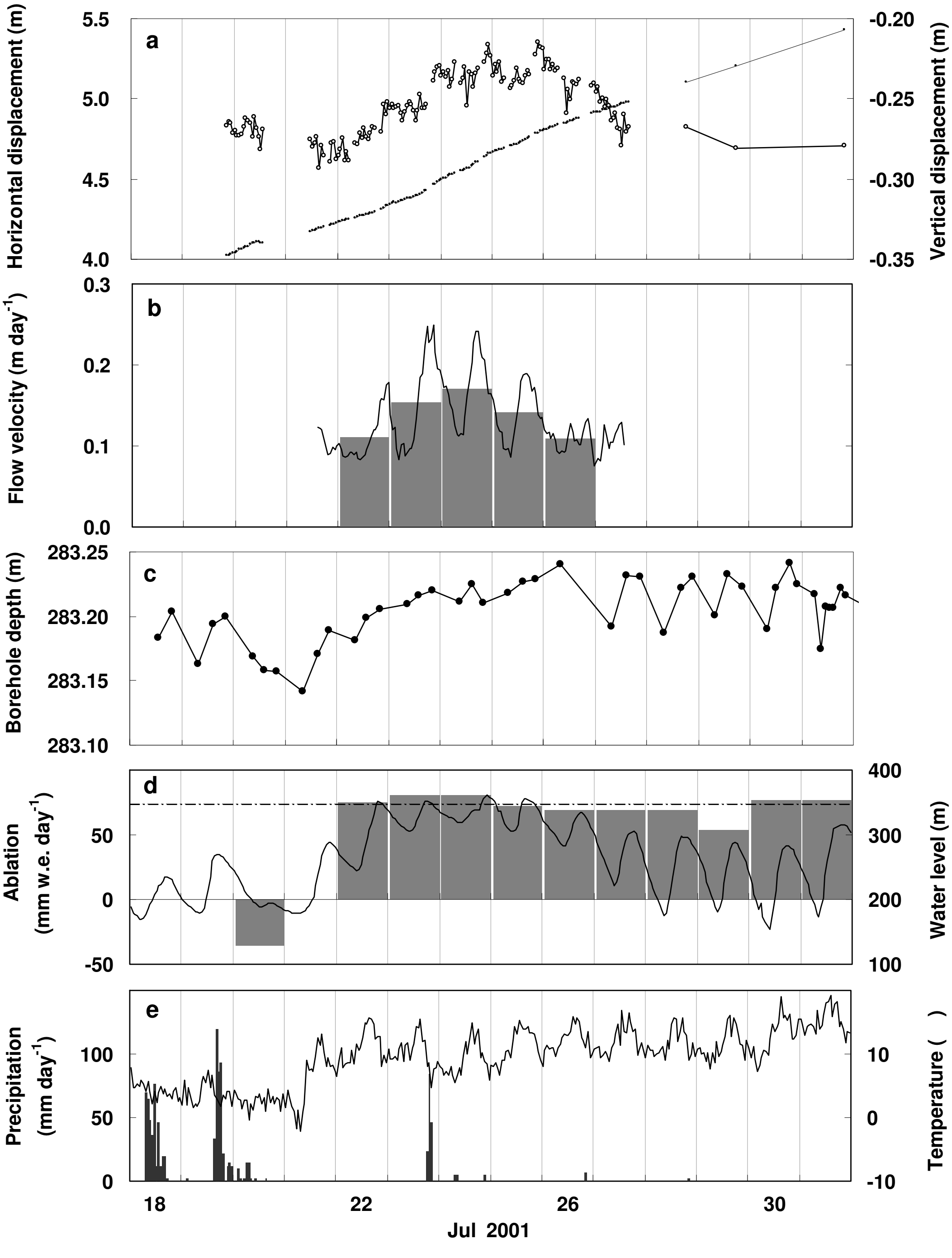

Figure 2.7: *Time series of data taken in Period II. (a) Horizontal (dot) and vertical displacement (open circle) of the stake from its original position on 15 June 2002. (b) Horizontal surface velocity (solid line) and its daily average. (c) Borehole depth. (d) Surface ablation and water level (solid line) in the borehole, and the dash-dotted line indicates the overburden pressure. (e) Air temperature (solid line) and precipitation.*

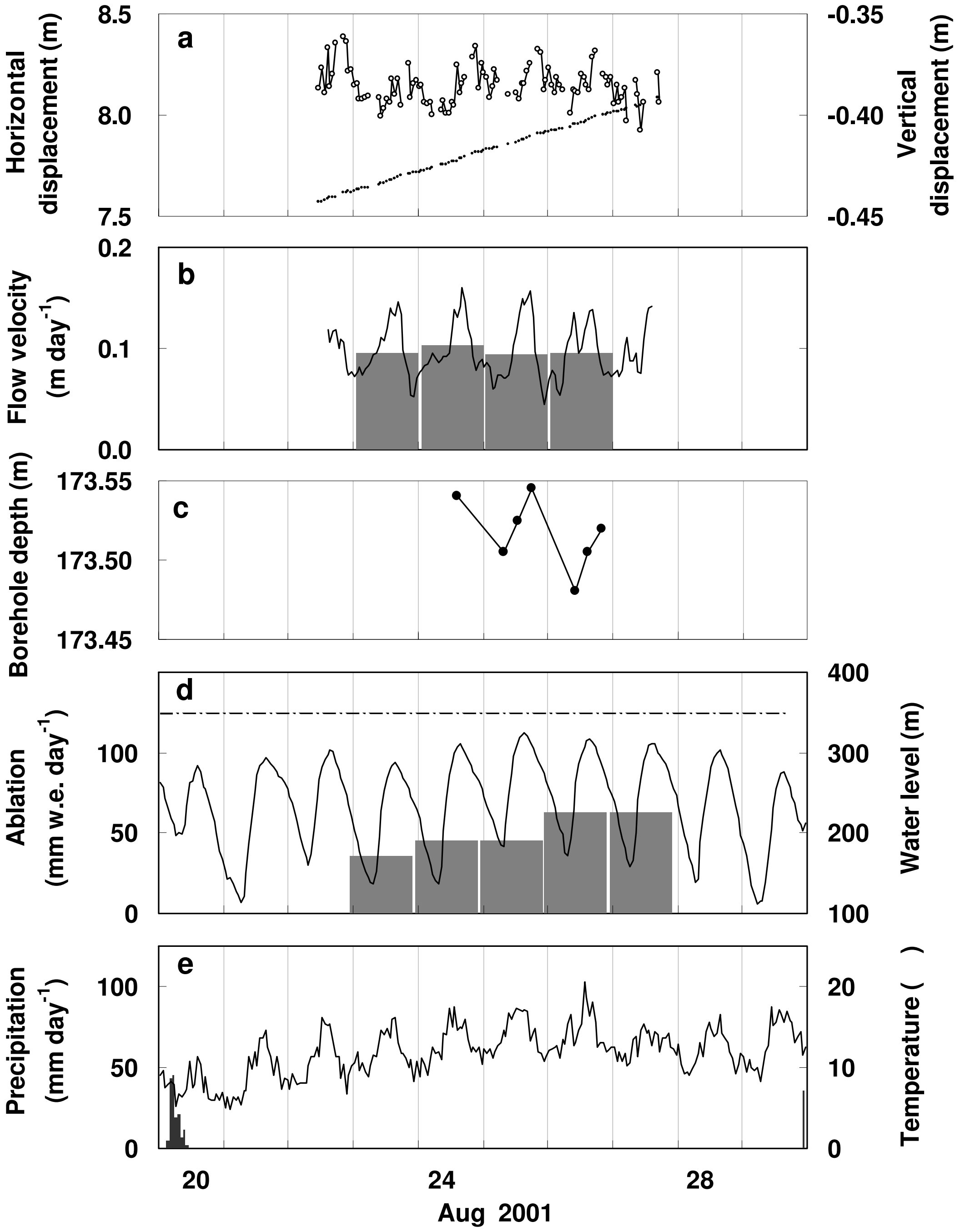

Figure 2.8: *Time series of data taken in Period III. (a) Horizontal (dot) and vertical displacement (open circle) of the stake from its original position on 15 June 2002. (b) Horizontal surface velocity (solid line) and its daily average. (c) Borehole depth. (d) Surface ablation and water level (solid line) in the borehole, and the dash-dotted line indicates the overburden pressure. (e) Air temperature (solid line) and precipitation.*

m a day in a diurnal manner, but it never exceeded the overburden pressure (Fig. 2.8d). Because the borehole for the depth measurement closed at 170 m from the surface, the measurement was continued by feeling the decreased tension as described in the method section. This measurement confirmed that the depth varied in the same diurnal manner as in July (Fig. 2.8c). Diurnal signals were also found in the vertical displacement, increase during the daytime and decrease at night (Fig. 2.8a). Surface velocity, vertical displacement, water level, and borehole depth, all these appear to oscillate in phase throughout this observation period.

2.3.4 Period IV (from 28 September to 3 October)

According to the records of meteorological station at the glacier, air temperature dropped at the beginning of September and cold weather with snow precipitation persisted until the end of September. The study site was covered with 0.5 m of fresh snow and the surface ablation had been reduced when the measurements were restarted on 28 September.

Surface velocity was steady at low level and clear uplift was not observed during the measurement period (Figs. 2.9a and b). The depth of the borehole, closed at 120 m from the surface, was measured and it was increasing monotonically (Fig. 2.9c). Water level measurement in a limited period shows little fluctuation in the subglacial water pressure, and implies the possibility that the connection to the basal drainage system was abandoned (Fig. 2.9d).

2.4 Summary

GPS survey and borehole depth measurements were carried out with continuous water pressure measurement during the ablation season in Lauteraargletscher. Main observational facts obtained in the field measurements are summarized below.

- Motion event triggered by a heavy rain storm was observed on 27 June with uplift. Surface velocity increased by 100% and the surface moved upward by 20 mm within a few hours. Borehole depth turned to decrease at this event.
- Clear diurnal variations in the surface velocity were observed in July and August. Surface velocity increased during the daytime and dropped at night. Water pressure varied diurnally as well, and the pressure variations were in phase with the surface velocity.
- The glacier surface moved in the vertical direction over different time scales. For example, sudden uplift at motion event on 27 June, diurnal uplift in August, and longer-term up and downward movement in July.
- Borehole depths changed significantly. The most conspicuous changes are diurnal variations in July and August, deepening in the daytime and shortening at night.

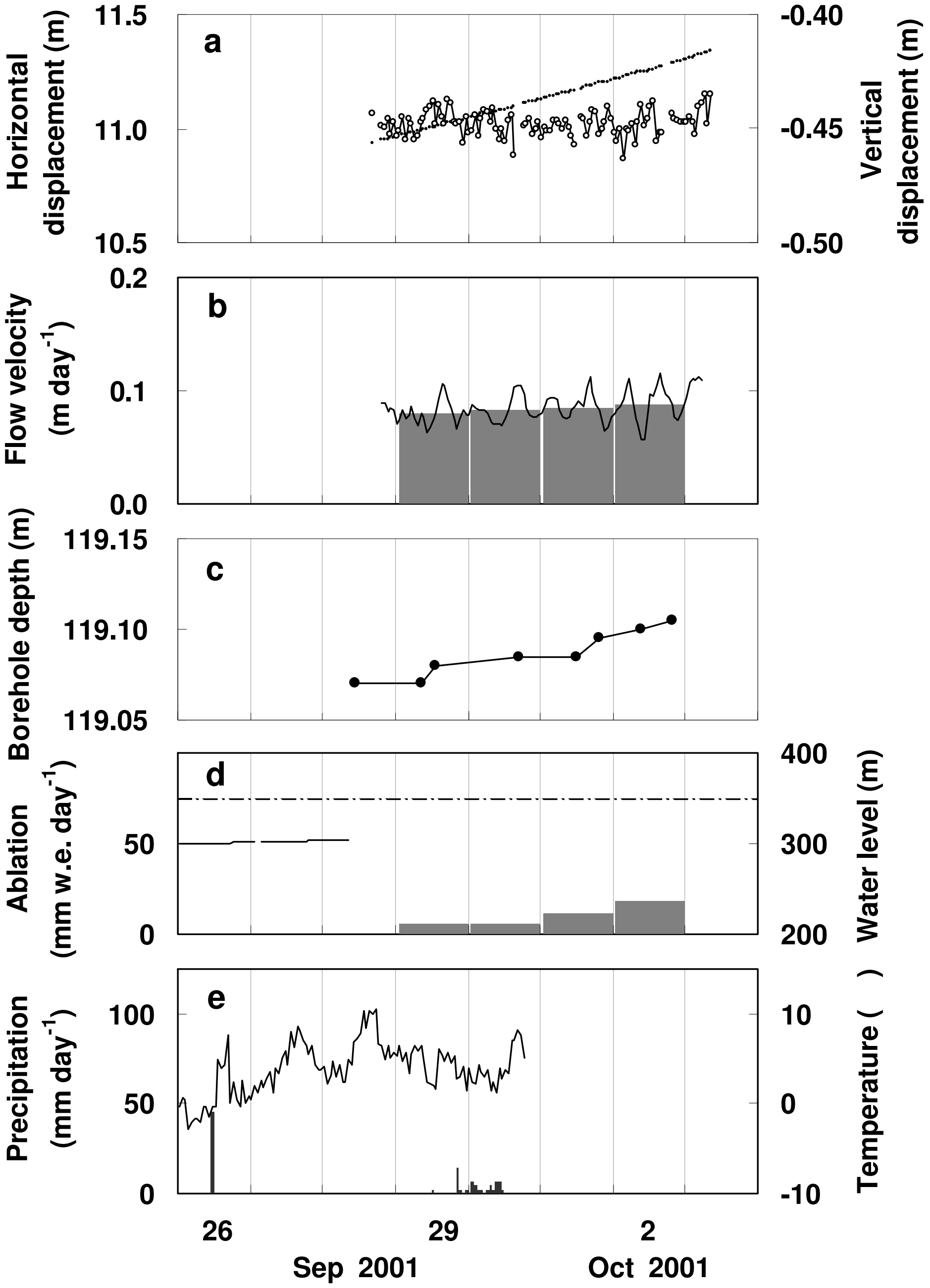

Figure 2.9: *Time series of data taken in Period IV. (a) Horizontal (dot) and vertical displacement (open circle) of the stake from its original position on 15 June 2002. (b) Horizontal surface velocity (solid line) and its daily average. (c) Borehole depth. (d) Surface ablation and water level (solid line) in the borehole, and the dash-dotted line indicates the overburden pressure. (e) Air temperature (solid line) and precipitation.*

The surface velocity and water pressure variations listed above are basically consistent with those observed at the other temperate valley glaciers. However, the measurements clearly depicted each of the summer event with high resolutions, and displayed the seasonal contrast in the short-term flow variations. Moreover, the significant variations in the borehole depth have never been obtained. These points are examined in detail in the next chapter, and their cause-and-effect relationship is discussed.

CHAPTER 3

FIELD DATA ANALYSES AND INTERPRETATIONS

Observed short-term flow variations are analyzed in detail and interpreted in this chapter. The relationship between surface velocity and subglacial water pressure is examined with a temporal resolution of 1 hour. Vertical distribution of the strain rate is derived from the borehole depths data, and the vertical strain is compared with the vertical displacement of the surface to determine the cause of the surface uplifts. Based on the seasonal evolution of the subglacial hydraulic condition which is infered from the water pressure variation, it is proposed that spatially non-uniform basal lubrication caused the diurnal variations in the flow velocity and vertical strain rate.

3.1 Diurnal Variations in the Surface Velocity

3.1.1 Relation between water pressure and surface velocity

Horizontal surface velocity fluctuated diurnally in July and August when substantial melt water was produced on the surface. Because the velocity oscillated in phase with the borehole water level, it is implied that high water pressure lubricated the bed and enhanced basal motion. In order to examine the effect of subglacial water pressure on the surface velocity, hourly surface velocities measured in the periods of 21-27 July and 22-27 August are plotted against the effective pressure P_e in Figure 3.1. The effective pressure was obtained from measured water pressure P_w and the ice overburden pressure P_i,

$$P_e = P_i - P_w. \tag{3.1}$$

The overburden pressure was calculated from the local ice thickness determined from the hot water drilling records.

A scatter plot of the data points from the two observation periods (Fig. 3.1a) shows that surface velocity increases as effective pressure approaches zero. This relationship is similar to the observation by Iken and Bindschadler (1986) at Findelengletscher, and those by Kamb and Engelhardt (1987) at Variegated Glacier. Presumably, the basal ice decoupled from the

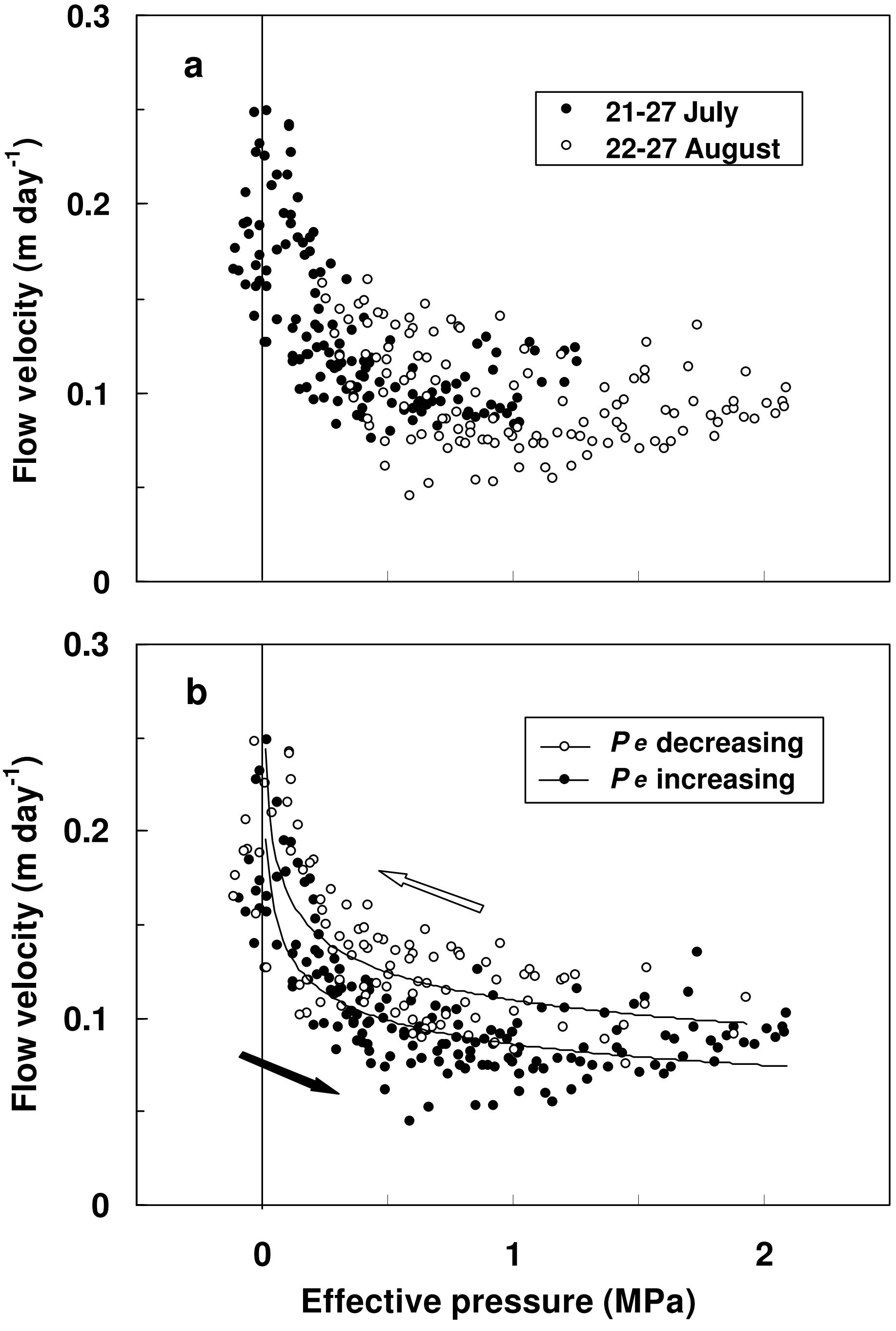

Figure 3.1: *(a) A plot of surface flow velocity against water pressure measured in Period II (solid circles) and Period III (open circles). (b) The same plot as (a) but the open and solid circles are the data taken when the effective pressure was decreasing and increasing, respectively. Solid lines are regression curves (Equation (3.2))for the effective pressure decreasing and increasing phases.*

bed when the overburden pressure is canceled by subglacial water pressure. Although the velocity is clearly correlated to the effective pressure in Figure 3.1a, the velocities scatter over broad rage up to ±20-30%. This scattering can be attributed partly to GPS measurement errors, but another plot in Figure 3.1b reveals two distinct relationships. Figure 3.1b is the plot of the same data set as Figure 3.1a, but the data points are distinguished by the periods when the effective pressure was decreasing or increasing. There is a clear difference between the two data sets, where surface velocity is larger when the effective pressure is decreasing, i.e. subglacial water pressure is increasing. This bimodal pressure dependence of the velocity (hysteresis) has never been reported before, and was observable in this study owing to the high temporal resolution in the velocity measurement.

3.1.2 Cause of the hysteresis

One of the clues to interpret the hysteresis in the surface velocity is the results of velocity measurements with three GPS's running at the borehole depth measurement site, 1.5 km upglacier and downglacier from the study site. These GPS's were operated independently from the one at the site 313 with another reference station fixed near the meteorological station.

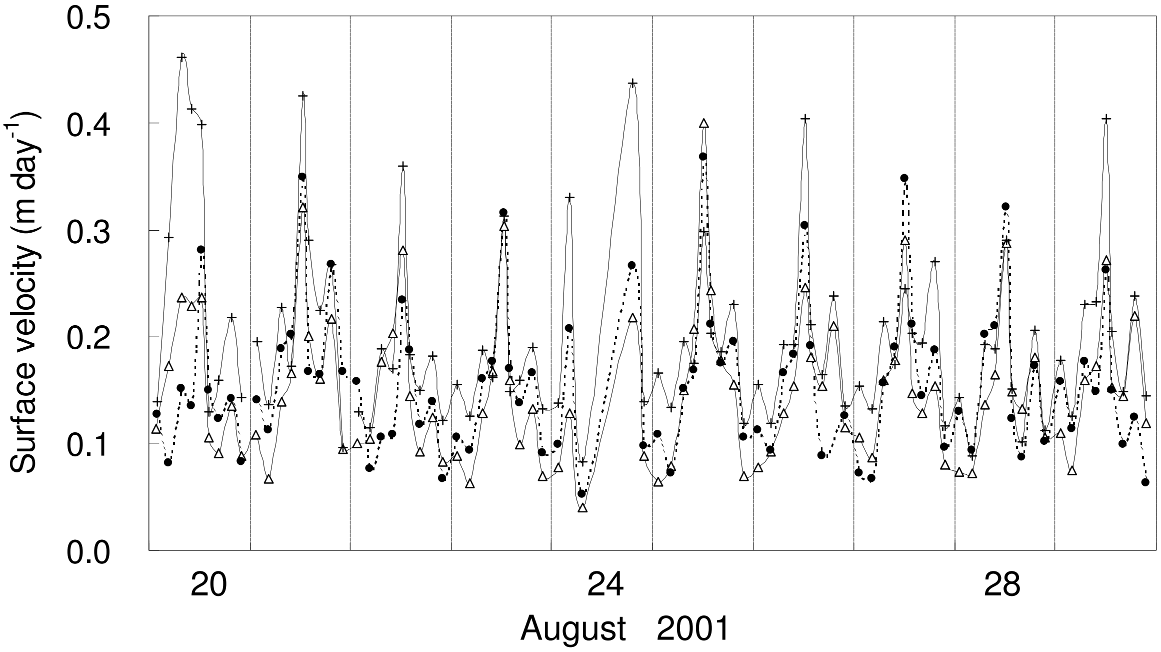

Figure 3.2: *Surface velocities during Period III measured at the borehole depth measurement site (dot), 1.5 km upper (cross) and lower reaches (triangle) from the study site.*

Positions were determined 9 times a day and the relative positioning error was larger than that in the measurement at 313 because of the method employed for the survey (rapid static positioning) and longer distance to the reference station. Other details of the measurement method are described by Gudmundsson (2002). Figure 3.2 shows surface velocity variations obtained by these GPS measurements. Temporal velocity changes are not smooth because of the positioning error, but general features displayed by Figure 3.2 are as follows. Diurnal variations in the surface velocity are observed in all of the three sites, and the rate of velocity increase in the daytime is larger in the upper reach of the glacier. A clear example is the data on 24 August. During this period, horizontal strain on the surface and vertical strain measured in the borehole showed strong compressive flow during daytime, as described in the following section 3.2.2, and such strain regime is consistent with the GPS measurements described above. If the flow regime during the second observation period is assumed to be similar to Figure 3.2, following interpretation can be made for the hysteresis in the surface velocity against subglacial water pressure. During the daytime, when subglacial water pressure increases, the study site is pushed by the upper reach because the glacier is more accelerated in the upper part of the glacier. At night, when the pressure decreases, the upper reach has already slowed down and no pushing force acts on the study site. Because of the pushing force conveyed from upper reach, surface velocity at the study site is higher when the water pressure increases.

It is not surprising to see the surface velocity at one point to be influenced by other regions through stress coupling. However, not many field observations have been reported in relation to this matter. Hanson and others (1998) studied diurnal variations in surface velocity and subglacial water pressure at Storglaciären in Sweden, and found that the velocity increased before the local water pressure started to increase. They attributed the observation to the longitudinal stress conveyed from the upper reaches where velocity increased earlier of a day than the study site. Mair and others (2001) also discussed the stress coupling with surrounding ice during a motion event at Haut Glacier d'Arolla in Switzerland. The influence of the neighbouring basal condition can be determined quantitatively only with the consideration of length scales and viscous properties of ice. If the horizontal scale of the basal uniformity is much larger than the ice thickness, longitudinal stress components are regarded to be negligible. This approximation is successfully applied for the Antarctic and Greenland ice sheet modelling (Hutter, 1983), but it is not a realistic assumption for valley glaciers. The influence of a spatially distributed basal condition on the flow field is investigated quantitatively with a numerical flow model in Chapter 4, and the hypothesis proposed for the observed velocity hysteresis is evaluated.

3.1.3 Comparison with other glaciers

The relationship between surface velocity and subglacial water pressure obtained in this study is compared with those observed at other glaciers by using a power function,

$$u_s = kP_e{}^{\gamma}. \tag{3.2}$$

u_s is the surface velocity in mm day^{-1}, P_e is the effective pressure at the bed in MPa, k and γ are fitting parameters. This empirical equation was used by Jansson (1995) to fit the field data measured in Storglaciären and in Findelengletscher (Iken and Bindschadler, 1986). He found the identical regression parameter $\gamma = -0.40$ for the two glaciers and suggested that the basal motion is controled by the same basal process in the glaciers. The data plotted in Figure 3.1 require two different regression curves for the two pressure transient phases. Best fitting to each of the data sets gives, $k = 110$ and $\gamma = -0.18$ with a correlation coefficient of $r = 0.66$ for the effective pressure decreasing phase, $k = 86$ and $\gamma = -0.20$ with $r = 0.68$ for the increasing phase (Fig. 3.1b). The fitting parameters are summarized in Table 3.1 with those obtained for Findelengletscher and Storglaciären.

If it is assumed that γ is relevant to the dominant basal flow process of the glacier, the bed condition of Lauteraargletscher is suggested to be different from those in Storglaciären and Findelengletscher. As described in the section 2.1, the subglacial sediment layer under Unteraargletscher gets thinner in the upglacier direction and vanishes at the confluence area. Thus, Lauteraargletscher is considered to be underlain by hard bedrock, and it contrasts with the study site in Storglaciären where subglacial sediment layer exits (Hooke and others, 1997). In Findelengletscher, a subglacial sediment layer is expected because two reflecting horizons are observed in seismic soundings (Iken and Bindschadler, 1986).

Even if the parameters in Equation (3.2) have relations to the bed conditions, however, it is likely that the relationship is not spatially and temporally uniform in a glacier. In addition, as discussed in the previous subsection, the relationship may be affected by neighbouring bed conditions when the bed is inhomogeneous. Therefore, the parameters obtained from each measurement cannot be simply compared, and similar measurements on other glaciers are needed for further discussion.

3.2 Variations in the Strain Regime

3.2.1 Calculation of vertical and horizontal strain rates

To discuss the observed temporal changes in strain regime, vertical and horizontal strain rates are computed from the results of the borehole depth measurements and the survey of the strain array, respectively. The methods of the computations are described below.

Table 3.1: *Fitting parameters of the relationship between surface velocity and subglacial water pressure obtained at various glaciers. (↗) and (↘) indicate the effective water pressure increasing and decreasing phases, respectively.*

Glacier	k	γ	Ref.
Lauteraargletscher (↗)	86	-0.20	This study
Lauteraargletscher (↘)	110	-0.18	This study
Findelengletscher	371	-0.40	Iken and Bindschadler, 1986
Storglaciären	30	-0.40	Jansson, 1995

Successive measurements of the borehole depths were used to determine the vertical strain-rate distribution. The borehole depth changes plotted in Figures 3.3b, 3.4b, and 3.5b represent the sum of vertical normal strain and horizontal shear strain between the magnets in the borehole and the surface. However, it can be assumed that the depth change equals the total vertical strain over the borehole depth based on the discussion in the section 2.2.2. Accordingly, the rate of the borehole depth change is the vertical flow velocity relative to the surface at the depth of the each borehole bottom. Vertical flow velocities at 50, 150, and 300 m were measured at the same time and then linearly interpolated (relative vertical velocity is zero at $z = 0$ m) to obtain vertical velocity distribution at the measurement time. The vertical distribution computed for the every measurement is temporally interpolated to each 0.25-day interval, and plotted in Figures 3.3c and 3.4c. From the spatially interpolated data, vertical strain rate distribution was calculated as the derivative of the velocity with respect to the depth.

From 22 to 27 August, two-dimensional horizontal strain rate on the glacier surface was computed from the displacements of three poles surveyed twice a day using the method described in Appendix A. Surface strain rate was determined as a function of compass bearing for each period of 6:00-18:00 and 18:00-6:00 everyday. Then the strain is temporally interpolated and shown in Figure 3.5c. Strain ellipse, representing deformation of a unit circle due to horizontal strain field on the surface, was obtained for each survey interval and shown in a magnified form in Figure 3.6. Parameters of the ellipses determined for the intervals are tabulated in Table 3.2.

3.2.2 Spatial and temporal variations in the strain rates

Here, the discussion is focused on the measurements during Period I, II and III. The vertical strain distribution obtained for Period I shows how the ice responded to the heavy rainstorm on 27 June, which caused the clear change in surface velocity (Fig. 3.3a). Before this event, the depths of the three boreholes increased monotonically (Fig. 3.3b), and the vertical strain rates were positive (tensile) and constant with time throughout the depth (Fig. 3.3c). On 28 June, the strain rate became negative. The compression started near the surface and then moved deeper into the ice. In the following days, rather complex patterns of temporal and spatial variations in vertical strain were observed. For example, large temporal variations in borehole depths were observed with the 300-m borehole becoming 50-mm deeper over the night from 30 June to 1 July. Although the surface velocity reverted to its pre-storm pattern, the motion event on 27 June left a lasting impact on the englacial strain-rate distribution.

The 50-m borehole closed off by 18 July, but the strain rate distribution is available from the measurements in the other two boreholes. From 27 July to 1 August, large diurnal fluctuations in vertical strain were observed with the depths of the boreholes changing by up to 30-40 mm a day (Fig. 3.4c). In the daytime, the vertical strain rate in the shallower region was tensile, on the order of 10^{-3} day^{-1}, while at night it became compressive. Weaker, but similar, diurnal signals also occurred throughout most of the period of 18-27 July. Furthermore, the strain rate was vertically non-uniform, particularly from 30 July to 1 August, with the deeper regions being compressive while the shallower regions were tensile.

By 22 August, the 150-m borehole was frozen and the 300-m borehole was closed at 173-m below the surface. Although the vertical strain is obtained only from upper half of the ice thickness, diurnal oscillations in the strain were still clearly observable (Fig. 3.5b). The horizontal strain rate from 22 to 27 August showed diurnal oscillations in the direction of and perpendicular to the glacier flow except on 24 August (Figs. 3.5c and 3.6). Strain ellipses in Figures 3.6a and b represent the general surface strain regimes during the daytime (6:00-18:00) and nighttime (18:00-6:00). Their distinguishing features are compressive strain along the flow direction in the daytime and transverse tensile strain at night of about 10^{-4} day^{-1}. Combined with the vertical strain rate measured in the borehole, the ice deformation in the upper half of the glacier can be described as follows. From morning to evening, ice contracts horizontally in the flow direction and expands vertically. From evening to the next morning, it expands horizontally across the flow direction and contracts vertically.

3.2.3 Interpretation of the strain rate regime

The important aspect of the vertical strain measurements in Period I is the temporal reversal in vertical strain rate at the rainstorm. Similar strain-rate reversal has been observed previously during a motion event in Unteraargletscher (Gudmundsson, 2002). Until the event on 27 June, the observed steady and uniformly distributed tensile vertical strain rate is consistent with the spatial distribution of annual surface velocities that shows compressive flow at the study site (Gudmundsson and Bauder, 1999). The compressive vertical strain rate from 27 to 28 June is presumably related to spatially uneven acceleration of the glacier as a response to the large amount of water input by the rainstorm. This event may have triggered changes in subglacial hydrology, which caused the subsequent vertical strain rate fluctuations.

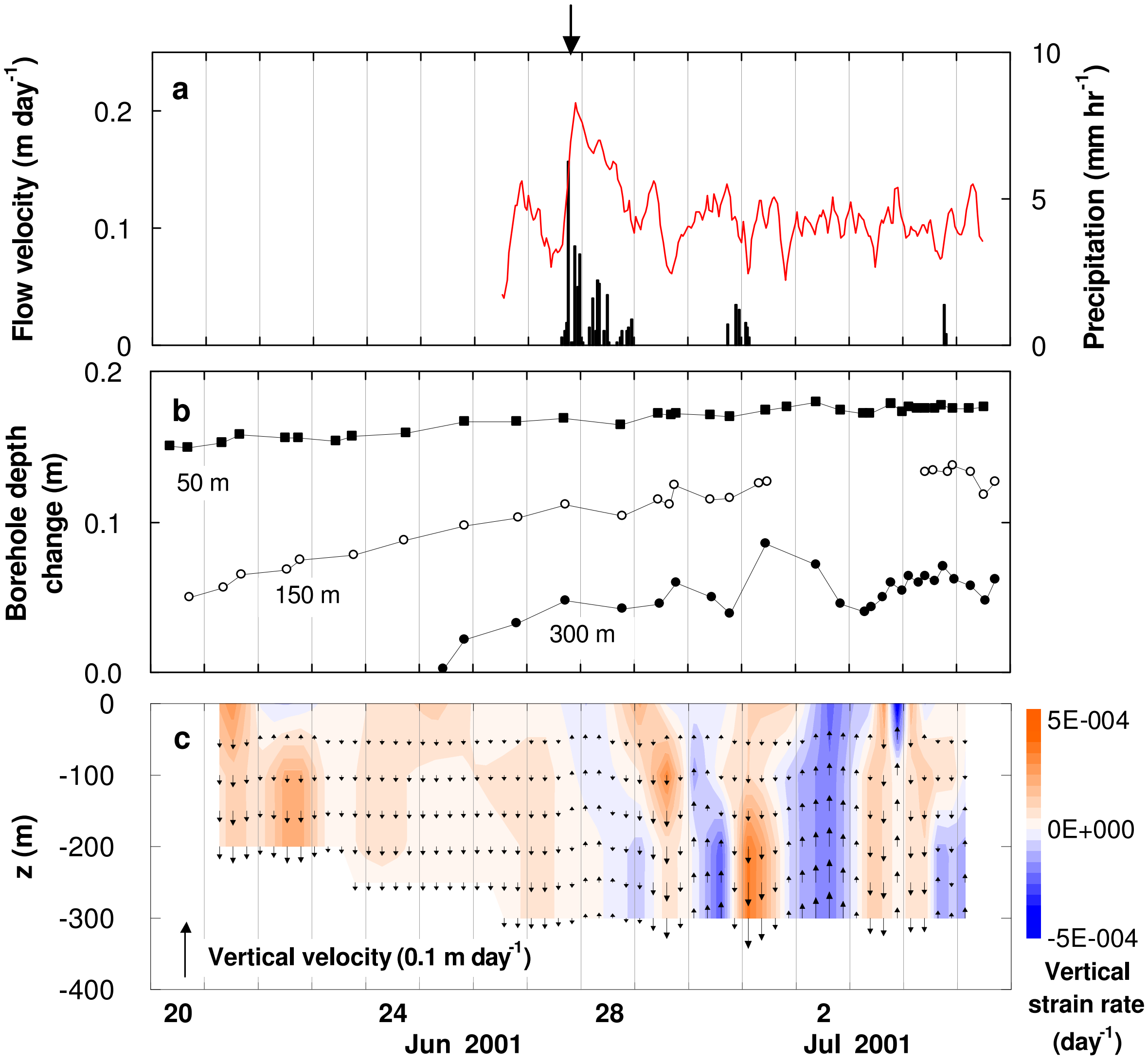

Figure 3.3: *(a) Horizontal surface velocity (red line) and hourly precipitation rate. (b) Borehole depth changes in the 50-m (solid square), 150-m (open circle), and 300-m (solid circle) boreholes. (c) Depth distribution of vertical velocity relative to the surface (vector plot), and vertical strain rate (contour plot) during Period I. Ticks on the temporal axes indicate 0:00 local time. The arrow in (a) shows the motion event described in the text. In (b), measurements in the 150-m borehole were interrupted 1-4 July because snow temporarily clogged in the borehole. In (c), z-axis is pointing upward from the origin at the glacier surface.*

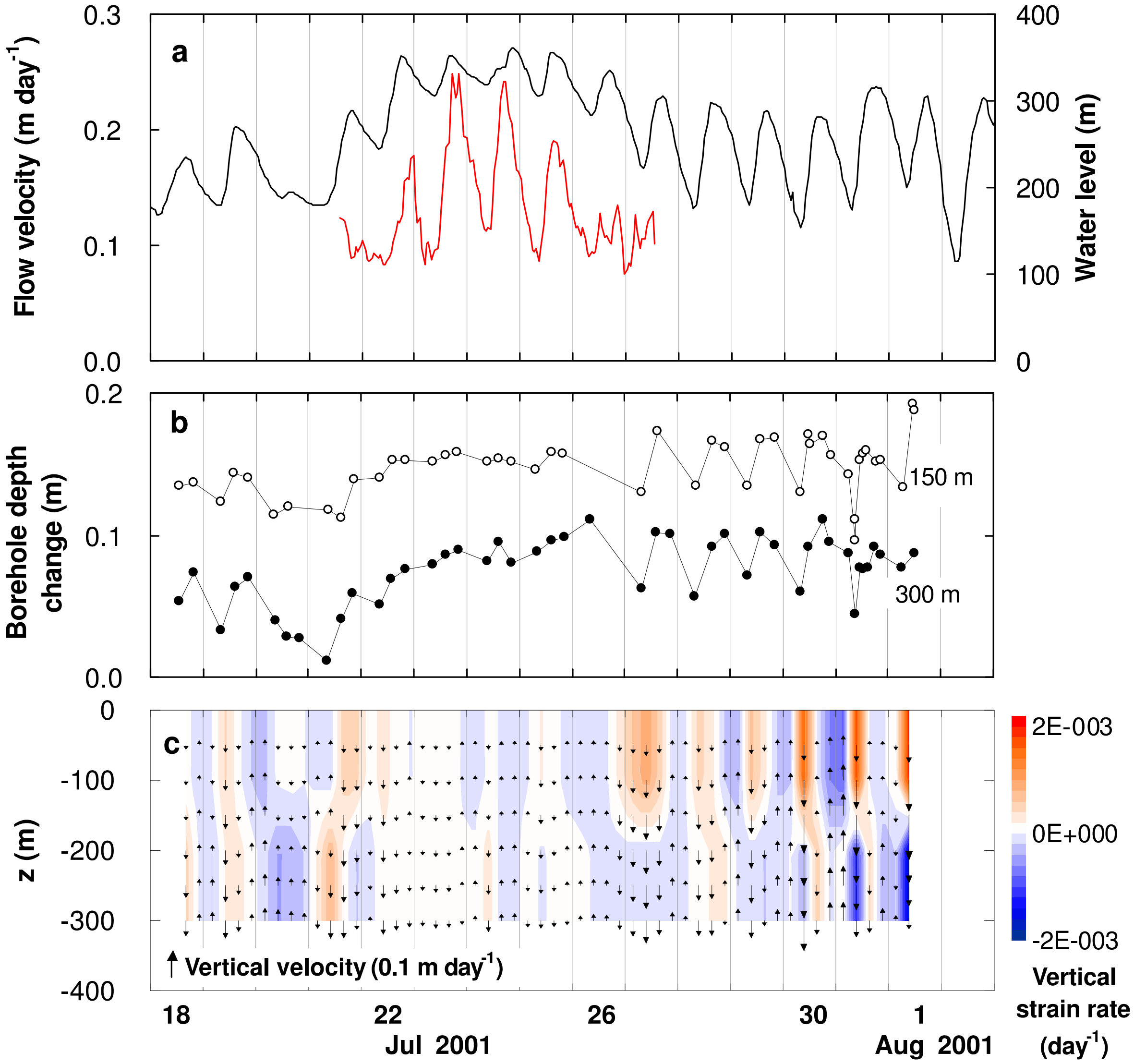

Figure 3.4: *in (a) Horizontal surface velocity (red line) and borehole water level. (b) Borehole depth changes in the 150-m (open circle), and 300-m (solid circle) boreholes. (c) Depth distribution of vertical velocity relative to the surface (vector plot) and vertical strain rate (contour) during Period II. Ticks on the temporal axes indicate 0:00 local time. In (c), z-axis is pointing upward from the origin at the glacier surface.*

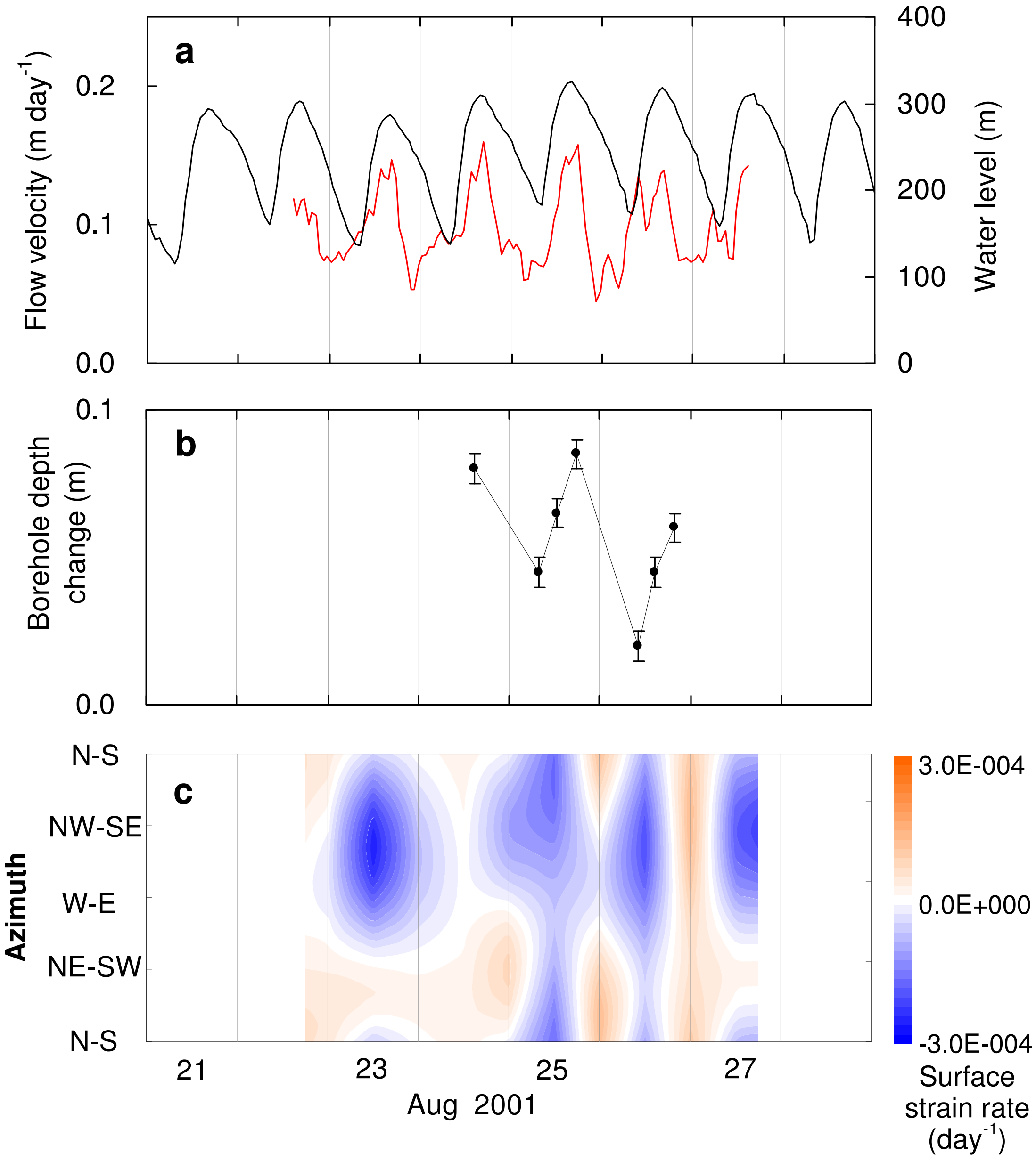

Figure 3.5: *(a) Horizontal surface velocity (red line) and borehole water level. (b), Changes in the 173-m borehole depth. (c), Horizontal strain rate on the surface during Period III. Strain rates were measured twice a day at 0:00 and 12:00, and the contours estimated by linear interpolation along the time axis. Ticks on the temporal axes indicate 0:00 local time.*

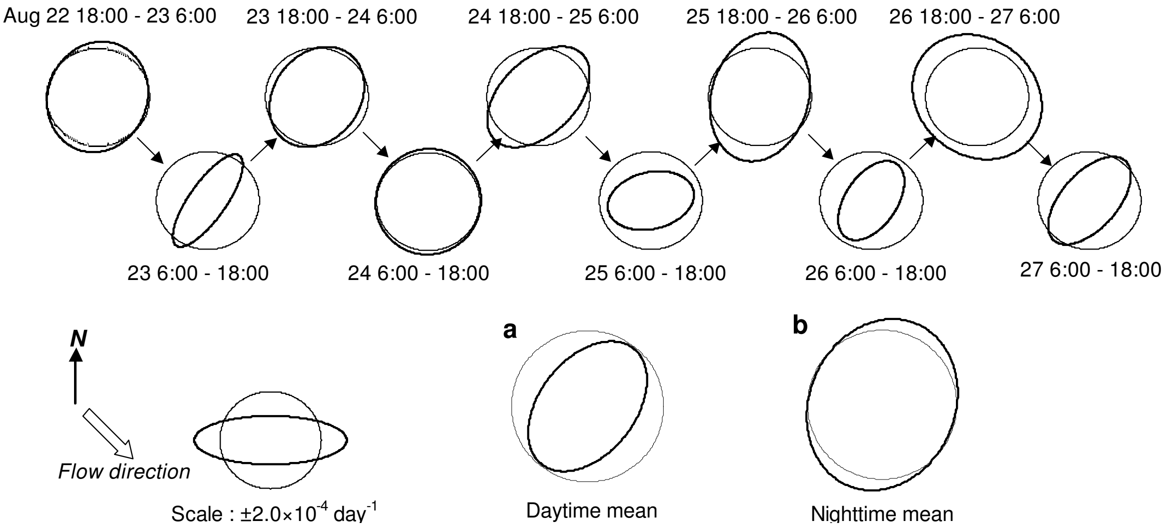

Figure 3.6: *Strain ellipses computed for each survey interval from 22 to 27 August (Period III). Circles and ellipses with thick line represent the original state and after the deformation, respectively. (a) and (b) show the mean strain rate during the daytime (6:00-18:00) and nighttime (18:00-6:00). Strain rate is shown in a magnified form by a factor of* 2.5×10^3. *The scale shows* 2×10^{-4} *day*$^{-1}$ *of tensile strain rate in W-E and the equivalent compression in N-S.*

One of the most important findings in this study is the diurnal fluctuations in the strain rate at the end of July and in August. Subglacial water pressure variation during these periods give insight to the cause of the strain oscillation. The observed water level is well correlated with flow velocity and borehole depth change (Figs. 3.4a, b, 3.5a, b). Furthermore, during the periods of diurnal strain rate oscillations, water levels changed by more than 100 m a day, indicating large amount of water drainage overnight in the subglacial hydrological system. The drainage efficiency was expected to increase progressively in the upglacier direction through the ablation season as it has been observed in other valley glaciers (Nienow and others, 1998). Evidence for this is seen in the water level trend from 23 July to 2 August (Fig. 3.4a). While surface melt rate remained approximately constant, diurnal peak-to-peak variation in water level increased with time and the daily minimum level decreased. This observation suggests the following interpretation of the diurnal fluctuations in the strain regime. When water pressure increases in the daytime, the glacier accelerates. The acceleration is larger in the upper reach because the subglacial drainage system there has not developed as well as that in the study area, and so the water pressure is higher in the upper reach. Faster flow in the upper reach causes longitudinal compression in the study area, which affects the vertical and surface strain regime in the daytime. At night, the flow velocity in the upper reach decreases to about the same velocity as that in the study area and then the longitudinal

Table 3.2: *Parameters of the strain ellipses obtained for the survey intervals. A and B are the major and minor axes of the ellipse ($A \geq B$), α is the bearing of the major axis, and $h^2 - 1$ represents the dilatation. α is measured counterclockwise from the north. See Appendix A for the details of the parameters.*

	6:00 – 18:00				18:00 – 6:00			
Date	$A-1$	$B-1$	α	h^2-1	$A-1$	$B-1$	α	h^2-1
Aug. 2001	(10^{-4})		(°)	(10^{-4})	(10^{-4})		(°)	(10^{-4})
22					0.29	-0.07	-14.0	0.22
23	0.21	-1.28	-31.7	-1.07	0.14	-0.34	-26.1	-0.20
24	0.17	0.04	-10.6	0.21	0.44	-0.51	-44.6	-0.07
25	-0.34	-0.80	14.1	-1.14	0.68	-0.11	-13.0	0.56
26	-0.20	-0.99	-33.7	-1.19	0.71	0.33	39.4	1.04
27	0.13	-0.90	-41.4	-0.76				
mean	-0.05	-0.74	-38.9	-0.79	0.36	-0.05	-23.1	0.31

compression disappears. This interpretation is supported by the GPS measurements along the flow line (Fig. 3.2). Larger acceleration in the upper reach is now understood as the result of seasonal evolution in the subglacial hydraulic efficiency. Both of the observations, diurnal variation in the strain regime and the velocity hysteresis discussed in the previous section, are originated from the uneven acceleration along the glacier. They figure out the influence of spatially non-uniform basal condition on the glacier flow field.

Interestingly, the vertical strain rate was not uniform with depth when the vertical strain varied diurnally. This sort of vertically non-uniform strain rate has been suggested theoretically to be associated with short-scale spatial variation in basal motion (Balise and Raymond, 1985; Vonmoos, 1999). When basal lubrication is not uniform along a glacier, as we expect for the periods of diurnal strain rate signals at Lauteraargletscher, predicted vertical strain rate is no longer constant with depth. Because these previous theoretical works have been limited to small amplitude perturbations and linear rheology, non-uniformity in vertical strain-rate distribution is further studied in the next chapter with a numerical flow model based on more realistic ice rheology.

3.3 Mechanism of Uplift

From June to August, conspicuous surface movements in vertical direction were observed by continuous GPS measurements. For example, sudden uplift by a few centimeters on 27 June, or diurnal up and downward movement in August. The rates of these vertical displacements are much larger than the estimated measurement errors. The mechanism of these uplifts is discussed in this section by comparing the GPS data to the borehole depth measurement result.

3.3.1 Causes of surface vertical movement

Vertical displacement of a glacier surface consists of three components, the perpendicular component of sliding along the inclined bed, the vertical strain averaged over the glacier thickness, and the volume changes in subglacial water cavities (Hooke and others, 1989). Iken and others (1983) evaluated the contribution of other factors to the surface vertical displacement, such as opening of crevasses, expansion of grain edge veins, or volume change in subglacial sediments, but they concluded that the the contribution is not significant. Therefore, it is assumed that the vertical component of surface flow velocity w_s is given as,

$$w_s = u_b \tan\beta + <\dot{\varepsilon}> h + \dot{V} \tag{3.3}$$

where β is the bed inclination, $\dot{\varepsilon}$ is the vertical strain rate, $\dot{V}$ is the vertical component of basal cavity opening rate, and the brackets indicate average over the glacier thickness.

The first term of the right hand side of Equation (3.3) can be subtracted from the measured vertical displacement as a steady long-term effect. This term does not contribute significantly to the short-term vertical movement because it is roughly evaluated as -7.7 mm day^{-1} at most while the short-term vertical displacements discussed here are more than a few centimeters per day. This preliminary evaluation of the first term was made with assumptions that the basal sliding accounted for all of the surface velocity in summer 2001 ($u_b = 0.11$ m day^{-1}) and the glacier bed has the same inclination as the surface ($\beta = 4°$). A better estimation was made from the vertical surface velocity and the vertical strain rate averaged from 25 June to 1 August. The vertical strain rate was obtained from the rate of the 300 m borehole depth change, and long-term volume changing rate of water cavity was assumed to be negligible compare to the other terms ($\dot{V} = 0$). Substitution of $w_s = -6.3$ mm day^{-1}, $<\dot{\varepsilon}> h = 1.8$ mm day^{-1}, and $\dot{V} = 0$ in Equation (3.3) yields $u_b \tan\beta = -8.1$ mm day^{-1} as the long-term effect of the basal sliding on the vertical movement of the surface. A similar but larger value than the preliminary rough estimation indicates that the basal sliding accounts for the major part of the total glacier flow in summer. After the subtraction of this steady downward movement, surface elevation change measured by GPS is compared with borehole depth change, which represents the vertical strain. If there is a discrepancy between them, residual uplift can be attributed to the water cavity opening. It is controversial whether the 300-m borehole depth change well represents the vertical strain over the glacier thickness or not, because measurements in the boreholes of different depths showed that the vertical strain rate was not always uniform from the bed to the surface. As a better estimate, however, the strain measured at the upper 300 m is regarded as the total strain over the whole thickness in the following interpretation.

3.3.2 Interpretations of the uplifts

Figures 3.7a-d show the vertical displacement of the surface, from which the basal sliding effect is excluded, and the borehole depth change. Before the mechanism of each uplift is examined, the possibility of atmospheric effect in the diurnal signals of the GPS measurements is discussed. Suspected are 10-30 mm uplifts at midnight observed from 22 to 27 June, from 22 to 25 July, and from 22 to 27 August. Because diurnal variations in atmospheric conditions may produce diurnal signals in GPS data, one should be careful whether they are real or artifacts. Judging from the following observations, however, they seem to be actual surface movement but not the consequences of atmospheric condition change. First, the diurnal variations were not always obtained under similar weather conditions. From 28 June to 5 July, for example, there is no diurnal signal in vertical displacement although the diurnal temperature variations are similar to those of the period from 22 to 25 June (Fig. 2.6a). Diurnal uplift is also missing from 28 September to 3 October, and surface velocity hardly changed during these two periods. It suggests that the diurnal signals are more relevant to the glacier dynamics rather than the climatological conditions. Moreover, vertical displacement correlated to the diurnal vertical strain from 22 to 27 August is convincing evidence that the GPS measurement is reliable. Therefore, it is plausible that the diurnal signals in the vertical displacement are not artifacts.

At the motion event on 27 June, the uplift cannot be ascribed to vertical straining because the vertical strain rate was compressive during the upward movement from 27 to 28 June. (Fig. 3.7a). It implies that the uplift was caused by the volume increase of subglacial water cavities. Water cavity opening is also suggested by the coincidence of the horizontal flow velocity peak with the maximum vertical velocity rather than the maximum displacement (Figs. 2.6a and b), because it conforms to the theoretical prediction that the sliding velocity is larger when the volume of cavities is increasing rather than the volume is its maximum (Iken, 1981). After the motion event, the surface moved downward probably due to the closing of the cavities. The borehole depth increased by 50 mm over the night from 30 June to 1 July, and the surface moved upward by 20 mm around the midnight. This uplift appears to be a consequence of the tensile vertical strain.

Upward surface movement from 21 to 25 July (Fig. 3.7b) and subsequent lowering are consistent with the borehole depth change. Therefore, the surface movement was generally controled by the vertical straining of ice during this period, and the regional flow regime turned from compressive to extending flow. A possible reason of the compressive flow from 21 to 25 July is larger acceleration in the upper reach of the glacier, because the subglacial drainage is expected to be less efficient upglacier and such condition is preferable to increase subglacial water pressure. Superimposed on the long-term variation, vertical displacement

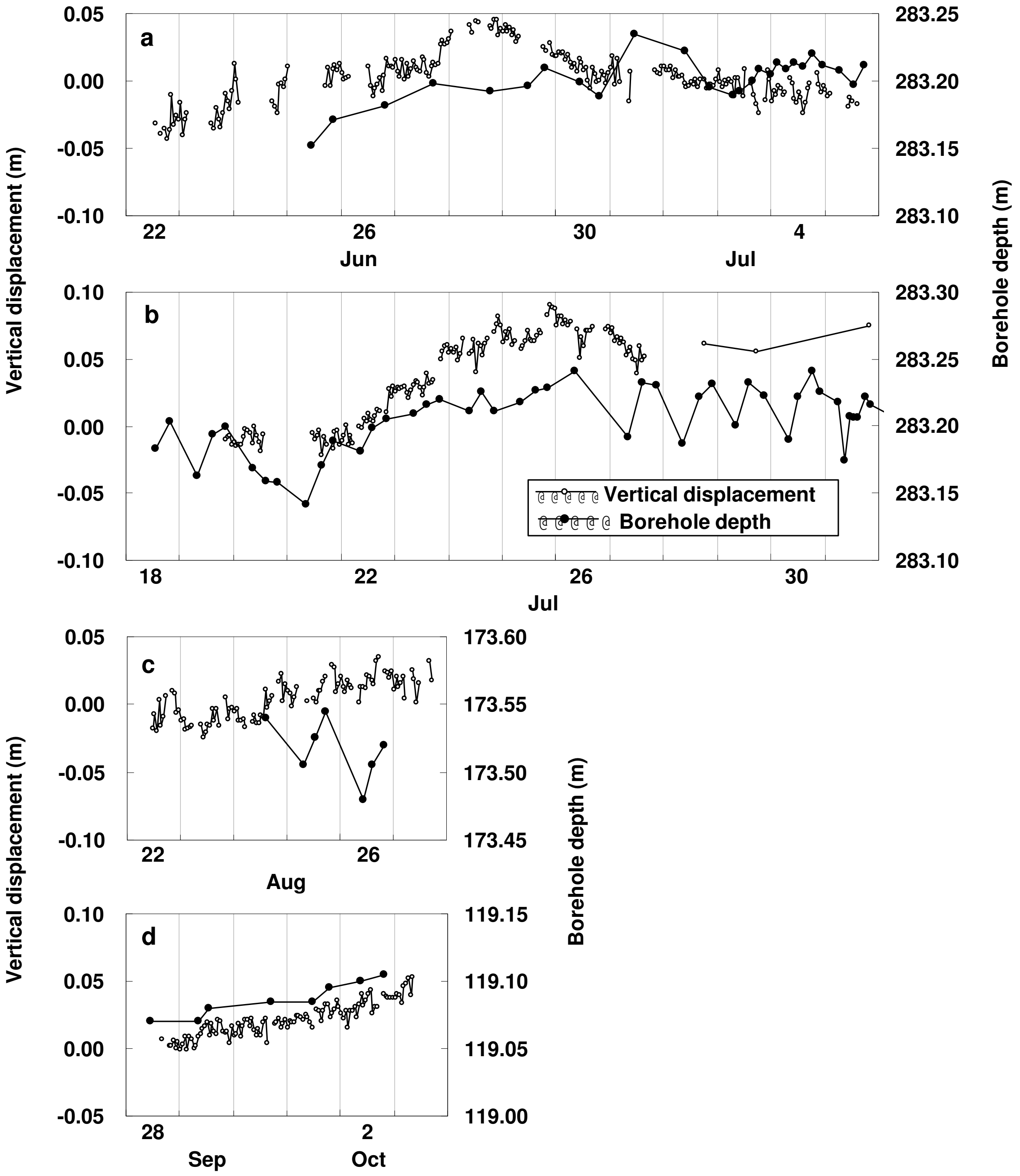

Figure 3.7: *Vertical displacement of the surface after the subtraction of estimated basal sliding effect (open circle) and the borehole depth change (solid circle).*

shows upward movement in the nights from 22 to 26 July. They seem to be the results of cavity opening because borehole depth does not show vertical extension and subglacial water pressure is very high at night during this period (Fig. 2.7d).

In August, it is rather difficult to determine the total vertical strain from the borehole depth measurement because the depth of the borehole is shorter than before. However, an apparent correlation between vertical displacement and borehole depth was observed (Fig. 3.7c). Therefore, the diurnal signal in the vertical displacement can be attributed to the diurnal variation in the vertical strain. Similar diurnal variation of borehole depth, deepening during the daytime and thinning at night, was also found in the latter half of Period II (Fig. 2.7c). The diurnal vertical strain variation conforms to the larger acceleration observed in the upper reach of the glacier (Fig. 3.2), because compressive flow establishes tensile vertical strain during the daytime.

In Period IV, from 28 September to 3 October, measured borehole depth is less than one third of the ice thickness. However, the steady upward movement of the surface is reasonably interpreted that the glacier was gradually thickening owing to compressive flow (Fig. 3.7d), because the annual surface velocity distribution shows that the flow is slightly compressive at the study site (Gudmundsson and Bauder, 1999). It is suggested that the glacier flow regime was switched to the winter mode as a result of reduction in the water supply to the bed. Internal ice deformation may have accounted for the dominant part of the flow velocity during this period.

3.4 Influence of Subglacial Drainage Condition on Water Pressure

The field measurements demonstrated that the subglacial water pressure controls glacier flow variation during the ablation season in temperate valley glaciers. Therefore, it is important to study the mechanism of water pressure variations to understand the nature of the flow regime changes. One of the control factors of water pressure is the amount of water supplied to the bed, and it consists of surface melt water and precipitation on the glacier. Another important factor is the subglacial drainage condition, which is considered to evolve from the beginning till the end of the ablation season. Due to the change in the drainage condition, water pressure reacts differently to the surface melt rate and precipitation as the ablation season progresses. To study the seasonal change in the subglacial drainage condition and their effect on the water pressure, pressure variation throughout the summer is examined with meteorological records in Figure 3.8.

Until the observation period in July (Period II), diurnal oscillation in the water pressure is not significant. This feature can be attributed to the snow which covered the study site until the late July in 2001, because a snow layer stores melt water and damps the diurnal signal in water input to the bed. There are sharp increases in water pressure up to overburden pressure on 6 and 15 July, and they coincided with heavy precipitation. Motion event observed on 27 June seems to be a similar incidence as those on 6 and 15 July. Nienow and others (1998) reported the results of dye tracing experiments in Haut Glacier d'Arolla, and concluded that a hydraulically efficient basal channel system develops upglacier with the snow line over the course of the ablation season. Their conclusion agrees with our observation, because very high pressure induced by precipitation in July suggests poor subglacial drainage efficiency, while precipitation in August, after the snow layer disappeared, is less influential on the water pressure.

In Period II, during the days with high air temperature, water pressure increased and kept close to the overburden pressure until 25 July. This observation period corresponds to the change of the surface condition at the study site from snow to ice. Consequently, surface ablation increased because of low albedo on the ice surface, and melt water started to drain into the bed directly through moulins and crevasses. Subsequently, under similar meteorological conditions, the mean water pressure started to decrease while the amplitude of the diurnal oscillation increased. It is infered that a large amount of water was supplied to the bed and the basal channel system developed during this period. Subglacial drainage efficiency increased, and it induced the changes in the mean water pressure and the amplitude

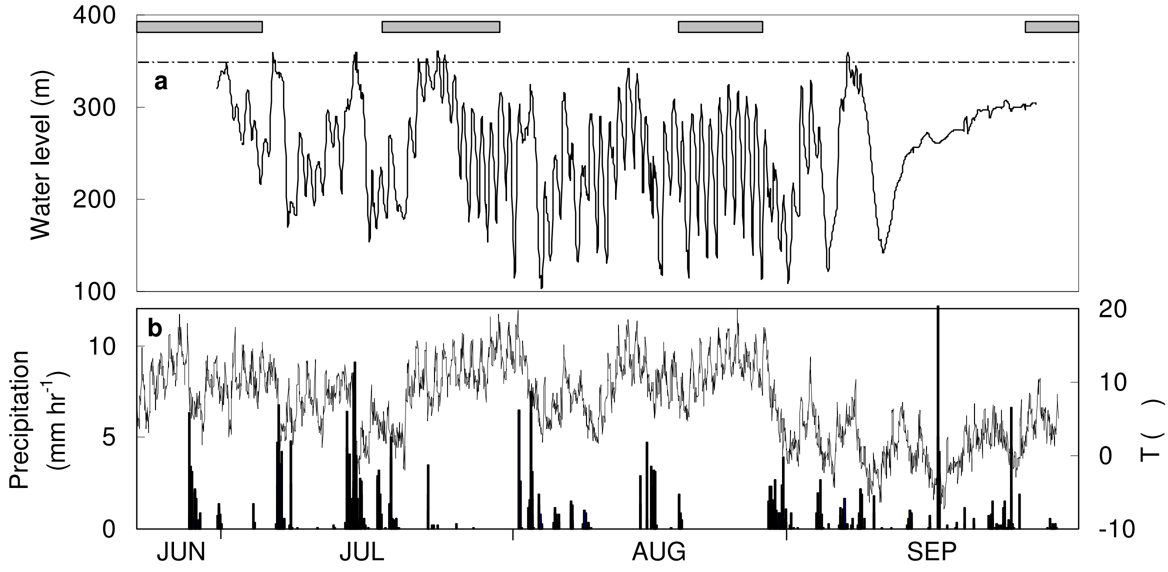

Figure 3.8: *(a) Subglacial water pressure variation, (b) hourly air temperature (solid line) and precipitation data through the summer 2001. In (a), the dash-dotted line indicates overburden pressure, and the shaded bars show the periods of GPS and borehole depth measurements.*

of the diurnal oscillation.

In August, meteorological conditions are similar to those in July, but the water pressure variation is unlike. The amplitude of the diurnal variations is generally large, whereas pressure never exceeds the overburden pressure. In addition, the daily mean pressure is more correlated with air temperature than with precipitation. These are indications of high drainage efficiency at the bed because of the following reasons. When the drainage channel system develops, water pressure drops rapidly early in the morning as the result of large drainage over the night, which increases the amplitude of the diurnal variation. The maximum pressure, on the other hand, does not rise up to the overburden level under the efficient drainage condition. Sudden water input by precipitation is less influential, and the pressure generally follows the amount of water input which is controled by the surface melt rate.

Diurnal pressure variation disappears soon after the air temperature drops in September. The absence of diurnal signal can be ascribed to the reduction of the ablation, but another possible reason is that the basal conduit system collapsed owing to insufficient water pressure and the basal hydrological system disconnected.

The observations described above suggest that there are two distinguishable hydrological basal conditions at the study site during the ablation season. One is a poor drainage condition characterized by the high sensitivity of water pressure to sudden water input. The other one is an efficient drainage condition characterized by large amplitude in diurnal water pressure variations and relatively low mean daily pressure. At the study area, the transition in 2001 occurred in the late July, when the surface snow layer disappeared and a large amount of melt water started to drain into the bed.

3.5 Summary

GPS measurement with high temporal resolution revealed the detail of short-term variation of horizontal and vertical surface movement in a temperate valley glacier during the ablation season. Horizontal velocity is mainly controled by subglacial water pressure, and the velocity increases significantly when the pressure rises close to the overburden pressure. Detailed analysis of the relationship between surface velocity and subglacial water pressure showed bimodal pressure dependence of the velocity. This finding suggests that glacier flow at a point is influenced by the motion of the surrounding ice mass through stress coupling.

The influence of surrounding ice flow condition is also confirmed by the vertical strain rate variations. The short-term strain rate variations observed from June to August cannot be interpreted by changes in local flow condition alone. Diurnal strain variations in Period II and Period III are understood as the results of spatially distributed basal condition and its temporal evolution. Surface velocity variations along the flow line, and the surface strain rate analysis support the idea that compressive flow is enhanced at the study site when the bed is more lubricated upglacier.

Vertical displacement of the surface was compared with vertical strain measured within the glacier to determine the mechanism of uplift. Two intrinsically different types of uplifts were observed, one originates from vertical straining and the other one is presumably caused by the volume increase of subglacial cavities. Therefore, uplift accompanied by high water pressure cannot be simply related to subglacial cavities alone, because compressive flow established by velocity increase in the upper reach may cause tensile vertical strain at the study site.

Subglacial water pressure variation determines flow variations during the ablation season in temperate valley glaciers. The surface melt rate and precipitation affect the water pressure, but the surface snow layer and subglacial drainage condition also take a crucial role in the pressure variation. When the surface is covered with snow, diurnal variation is less significant and heavy precipitation raises water pressure up to overburden pressure. After the snow line ascends upglacier, the amplitude of diurnal variation increases while the mean pressure decreases. Water pressure is more directly controled by surface melt rate and less sensitive to sudden precipitation in the late ablation season. Absorption of water by a snow layer, development of moulins after the snow disappeared, and increase in the subglacial drainage efficiency are the likely reasons of the changes.

CHAPTER 4

NUMERICAL INVESTIGATION ON THE FLOW FIELD

In this chapter, a numerical glacier flow model is developed and utilized to determine the effect of spatially non-uniform basal lubrication on the flow field. The model computes stress and strain fields in a longitudinal cross section of a glacier under prescribed basal slipperiness conditions. This numerical work aims to verify the hypotheses proposed for the observed short-term flow variations. Starting from the general investigation on how basal motion spreads into the flow field, diurnal variations in the velocity and strain rate are reproduced by prescribing temporal evolution of a spatially non-uniform basal slipperiness.

4.1 Methods

4.1.1 Field equations

The problem to be solved is the two-dimensional flow of incompressible viscous material governed by Stokes equations:

$$\nabla \cdot \mathbf{u} = 0, \tag{4.1}$$

$$\nabla p - \mu \triangle \mathbf{u} = \rho \mathbf{g}, \tag{4.2}$$

where $\mathbf{u}$=(u, w) is the velocity vector, p is the hydrostatic pressure, μ is the viscosity, ρ is the density of ice, and $\mathbf{g} = (g_x, g_z)$ is the gravity vector. The derivation of the Stokes equation is described in Appendix A. Parallel sided slab geometry is employed, and a Cartesian coordinate system is used with the x-axis along the bed pointing downglacier, and the z-axis normal to the bed pointing upward. Glen's flow law (Glen, 1952, 1955) in the generalized form (Nye, 1953) is used as the constitutive relationship:

$$\dot{\varepsilon}_{ij} = \frac{1}{2\mu}\tau_{ij}^{n} = A\tau_{e}^{n-1}\tau_{ij}, \tag{4.3}$$

$$\tau_{ij} = \sigma_{ij} - p\delta_{ij} \tag{4.4}$$

$$\tau_{e}^{2} = \frac{1}{2}(\tau_{xx}^{2} + \tau_{zz}^{2}) + \tau_{xz}^{2} \tag{4.5}$$

where $\dot{\varepsilon}_{ij}$ and τ_{ij} are the components of the strain rate and deviatoric stress tensors, respectively, and τ_e is the effective stress.

The rate factor A and the flow-law exponent n are material parameters. The commonly accepted value of $n = 3$ is used for the flow-law exponent, and a rate factor is taken as $A = 10\,\mathrm{MPa}^{-3}\,\mathrm{a}^{-1}$, which gives modeled surface velocities similar to the annual mean velocity observed at the study area. Taking into account the reduction in shear stress due to the valley shape by using a shape factor of 0.5 (Nye, 1965), this value of the rate factor is equivalent to $10{\times}0.5^{-3} = 80\ \mathrm{MPa}^{-3}\ \mathrm{a}^{-1}$ in the three dimensional case. It compares favourably with $75\ \mathrm{MPa}^{-3}\ \mathrm{a}^{-1}$ which was used by Gudmundsson (1999) in a three dimensional numerical modelling of Unteraargletscher.

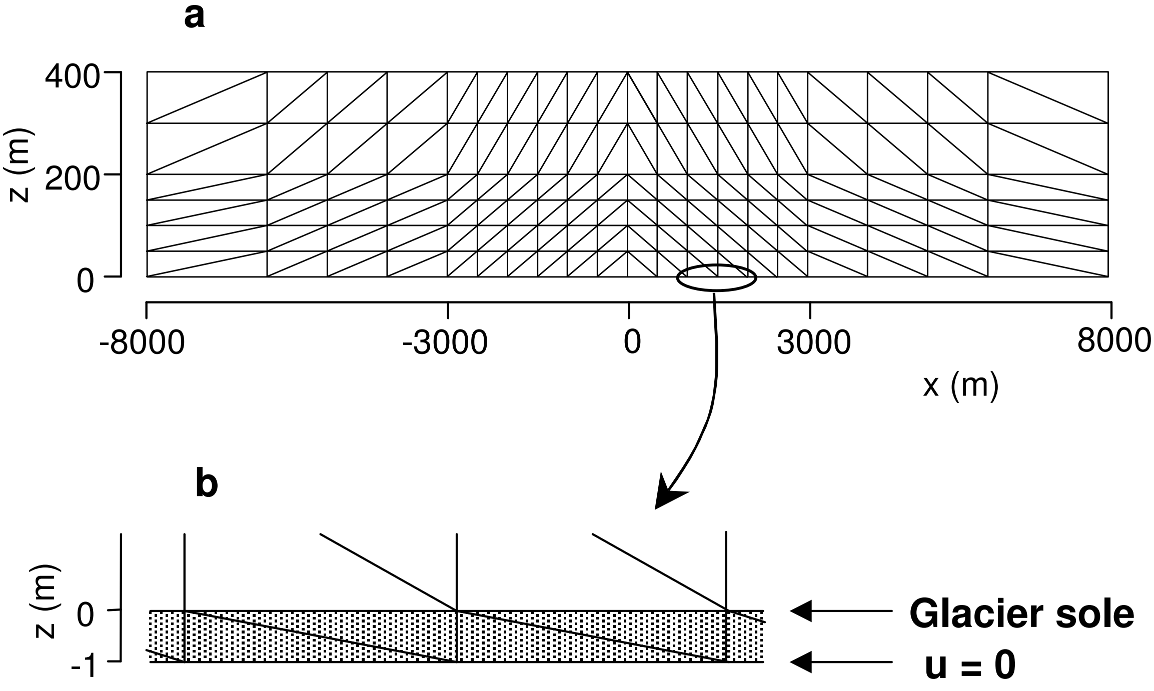

Figure 4.1: *Finite-element mesh used in this study. (a) All elements and coordinates used for the longitudinal cross-section model of a conceptional glacier with its head at $x = -8000$ m. (b) Enlargement of the mesh near the glacier bed. Shaded region indicates the 1-m thick subglacial thin layer used to introduce basal motion.*

4.1.2 Numerical scheme and model description

Equations (4.1)-(4.3) are solved with the finite-element method that is coded for this study (Sugiyama and others, 2003). Figure 4.1a shows the finite-element mesh used in the computation. The geometry of the 6-km central part of the finite-element grid is a simplified longitudinal cross-section of Lauteraargletscher. The mesh is finer at the deeper region where larger stresses and strain rates are expected, and it is horizontally uniform and symmetric to prevent the influence of the mesh irregularity. Based on the field observations (Funk and others, 1994; Bauder, 2001), the ice thickness and surface slope are assumed to be 400 m and 4°, respectively. To minimize boundary effects, the numerical grid was extended an additional 6-km upstream and 6-km downstream from this central section. We used Galerkin method with quadratic shape functions (Zienkiewicz and Taylor, 2000) to compute velocity and pressure fields. The theoretical basis and discretization scheme of the finite-element method are described in Appendices B and C. Starting from the solution of a linearly viscous flow, a new effective viscosity distribution was calculated from the previously determined strain-rate field, and the calculation repeated until the horizontal velocity field converged within 10^{-5} m a^{-1}. The flow diagram of the computation is shown in Figure 4.2. After the convergence, velocity components are known at each node and mid-point, and the maximum resolution of the velocity field is 250 m longitudinally and 25 m vertically.

4.1.3 Boundary conditions

Basal motion is simulated by introducing a thin deformable sub-basal layer into the finite element model. The viscosity of this layer can be regarded as the effective viscosity of subglacial sediments, or, which in the case of Lauteraargletscher is more appropriate, as being related to the form drag generated by sub-grid bed roughness. Spatially varying basal slipperiness is generated by giving different viscosity values to some of the elements of the sub-basal layer. A non-slip boundary condition is applied for the bottom nodes of the sub-basal layer (Fig. 4.1b).

Ignoring the effects of longitudinal stresses within the sub-basal layer, the deformational velocity of the layer is determined by the viscosity of the sub-basal layer, the layer thickness, and the shear stress at the top of the layer. This gives rise to a sliding law of the form

$$u_b = 2dA'\tau_b^{n'} \equiv c(x)\tau_b^{n'}, \qquad (4.6)$$

where u_b is the basal flow velocity, d is the layer thickness, τ_b is the basal shear traction, A' and n' are the parameters of the layer. Basal flow velocity is established by prescribing the basal flow coefficient $c(x)$. When the basal motion occurs due to the deformation of a subglacial sediment layer, n' should be determined by the mechanical property of the sediments. When basal ice slides over a bedrock, however, it can be related to the viscous property of ice. Because the basal flow process under the Lauteraargletscher is not certain and the mechanical properties of basal ice is not well understood, $n' = 1$ is assumed for simplicity. This assumption decides the basal velocity distribution, but does not affect how it spreads into the glacier. This method of introducing basal motion through a sub-basal layer has been used before (e.g. Vieli and others, 2000). It has an advantage to be able to determine the basal velocity and stress distributions naturally by prescribing some kind of *slipperiness* of the bed ($c(x)$), instead of specifying the velocity or stress themselves. Because longitudinal stress gradients will cause the thickness of the layer to change with time, this method is not favourable for transient calculations. In that case, the layer should be maintained at constant thickness. Here we are interested in obtaining snapshots of the velocity field for a given glacier geometry and thus we do not allow the surface or other boundaries within the finite-element mesh to evolve with time.

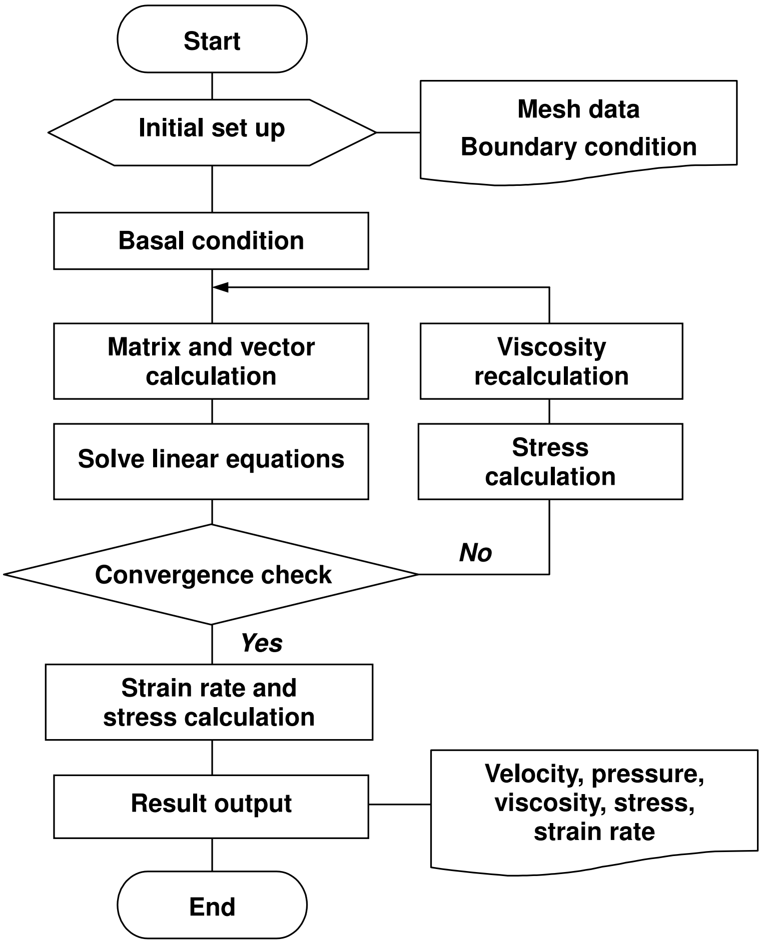

Figure 4.2: *Flow diagram of the finite-element glacier flow model.*

Stress free conditions at the surface boundary is written as

$$\tau_{ij} n_j = 0, \tag{4.7}$$

where n_j is a surface normal vector component and atmospheric pressure is neglected. The lower end of the modeled domain ($x = 8000$ m) was connected to the upper end ($x = -8000$ m) so that the glacier is assumed to be infinitely long (periodical boundary condition).

4.1.4 Model performance

In order to test and verify the constructed flow model, some of the computation results are compared with analytical solution and another flow model using finite-difference scheme.

The discretization error was evaluated by comparing the numerical results with the analytical solution for plane-slab flow under the non-slip condition. The largest error of 1.2% occurred in the horizontal surface velocity. By comparing the velocity profiles, it was found that the main source of the error was near the bed where the largest velocity gradient exists.

A computation result for the basal condition with a slippery zone was compared with the finite-difference numerical flow model developed and coded by Blatter (personal communication, September 2002), following the method proposed by Colinge and Rappaz (1999). This finite-difference model solves two dimensional Stokes problem in a longitudinal section including first order stress components (Blatter, 1995; Blatter and others 1998). Grid sizes of 200 m in horizontal and 20 m in vertical direction are used in the experiment for comparison. Basal velocity distribution was adjusted similar to that obtained with the presented model by giving the basal velocity as a linear function of the basal shear stress. Basal and surface horizontal velocities, and basal shear stresses computed with the two models are compared in Figure 4.3. Agreement in the surface velocities distribution is reasonably good. Only the difference in the surface velocities is the bulges at the outside of the slippery zone observed in the finite-element model. Because the used finite-element mesh is horizontally uniform in the compared region, the reason of the bulges are not clear. The discrepancy in the basal shear stress shows the characters of the two numerical schemes. While the finite-difference scheme gives stresses exactly at the grid points on the basal boundary, stresses in finite-element scheme are obtained for the elements that are facing the bed. Accordingly, basal stresses obtained in the presented model give diffused information because they are mean values of marginal elements. This characteristic feature of the finite-element method turns to an advantage when it deals with complicated boundary geometry.

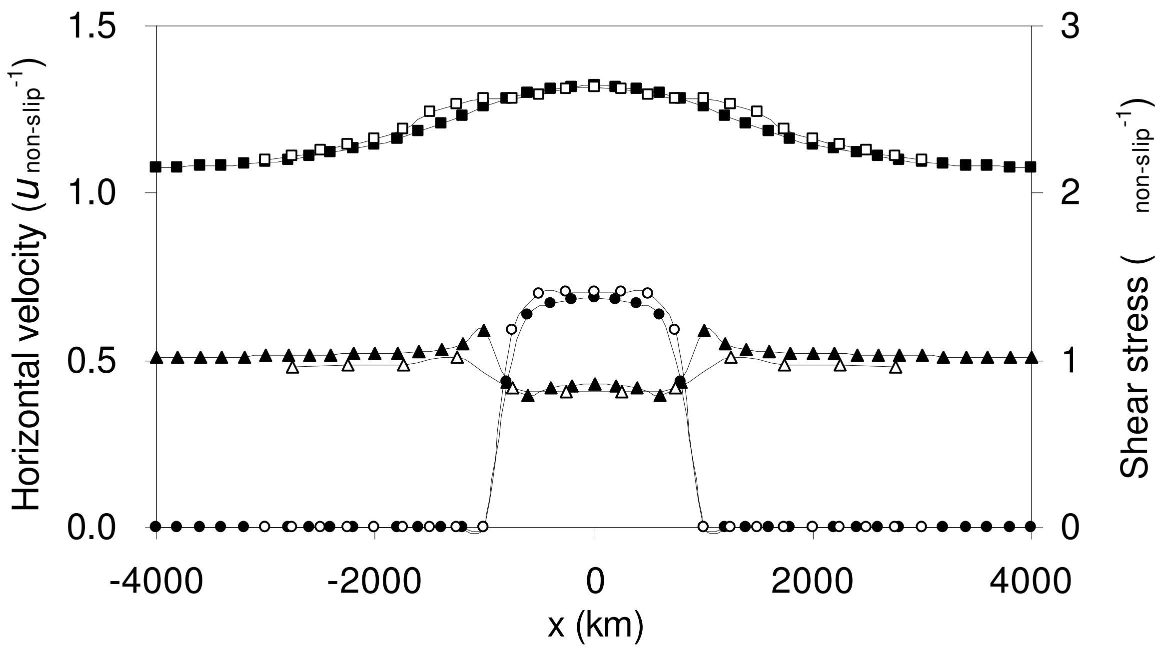

Figure 4.3: *The comparison of the results obtained by the presented finite-element model and the finite-difference model developed by Blatter. A slippery zone is set at* $-1000 < x < 1000$ *m so as to obtain similar basal velocities in the two models. Basal velocities (circle), surface velocities (square), and basal shear stress (triangle) are compared. Open symbols are the results of the finite-element model, and solid symbols are of the finite-difference model.*

4.2 Effects of Basal Lubrication on the Flow Field

4.2.1 Transmission of basal motion to the surface

Figure 4.4 shows model results for which the basal flow coefficient $c(x)$ is set to 50 m a^{-1} MPa^{-1} for the slippery zone within $-1000 < x < 1000$ m, and 10^{-3} m a^{-1} MPa^{-1} elsewhere. Introducing this slippery zone in the model increased the horizontal velocity component at the surface directly above the center of the zone by about 30% (Fig. 4.4a). With increasing distance up and down glacier, the magnitude of the velocity perturbation decreases. For example, five ice-thicknesses away from the boundaries of the slippery zone ($x = -3000$ and 3000 m), the increase in surface velocities is only 8%. The calculated vertical velocity components show extending and compressive flows at the upper and lower boundaries of the slippery zones, respectively (Fig. 4.4b). Furthermore, tensile and compressive deviatoric stresses occur throughout the entire glacier but are strongest near the surface (Fig. 4.4c). Because the

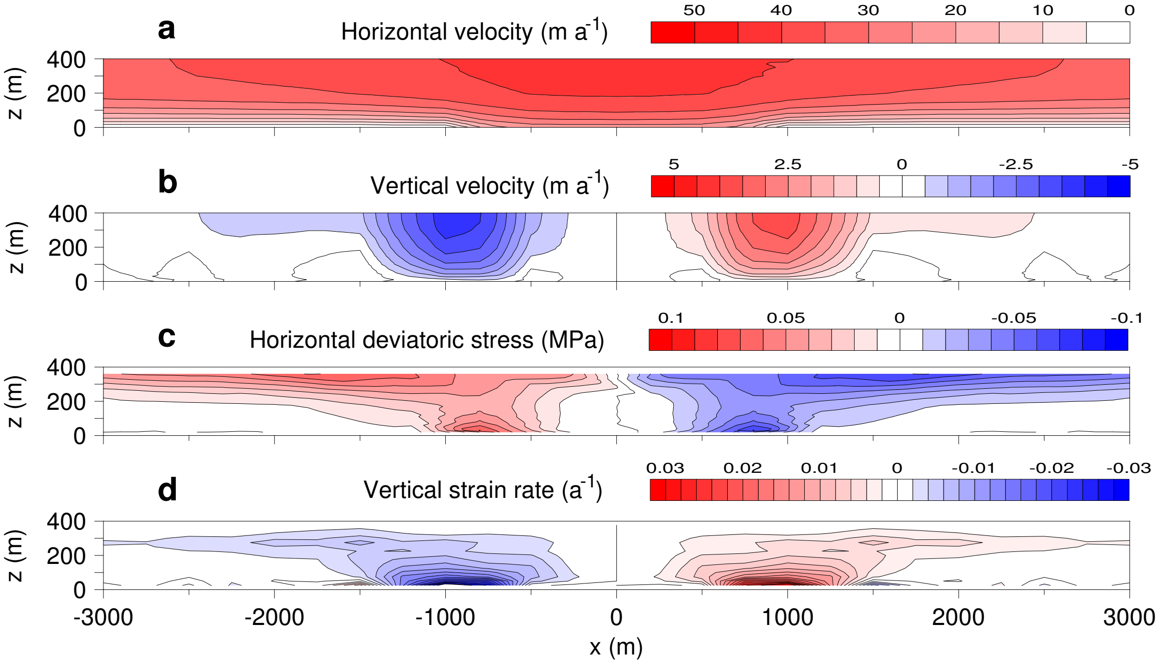

Figure 4.4: *Computed fields of (a) horizontal velocity, (b) vertical velocity, (c) longitudinal deviatoric stress component, and (d) vertical strain rate. Only the central domain of the modeled field ($-3000 < x < 3000$ m) is shown. Contour lines were established using the method of triangulation with linear interpolation.*

deviatoric stress is related to the vertical strain rate by Equations (4.1) and (4.3), vertical strain rate can be computed as shown in Figure 4.4d. The fairly large vertical strain rate near the surface helps to explain the observed vertical strain fluctuations that are discussed in the section 4.3.2. Analytical solutions for small-amplitude slipperiness perturbations also show a similar increase in deviatoric stress and strain with distance away from the source of the disturbance (i.e., the slippery zone) (Vonmoos, 1999).

Figure 4.5a shows the longitudinal distribution of basal and surface horizontal velocities calculated from the same basal condition as used in Figure 4.4 (c = 50 m a^{-1} MPa^{-1} at $-1000 < x < 1000$ m). To evaluate the transmission of basal velocity to the surface, the transmission factor of horizontal velocity is defined as

$$f_u = \frac{\triangle u_s}{u_b}, \tag{4.8}$$

where $\triangle u_s$ is the difference in horizontal surface velocity between non-slip and slip conditions and u_b is the basal velocity at the same position (Fig. 4.5a). Calculations were performed

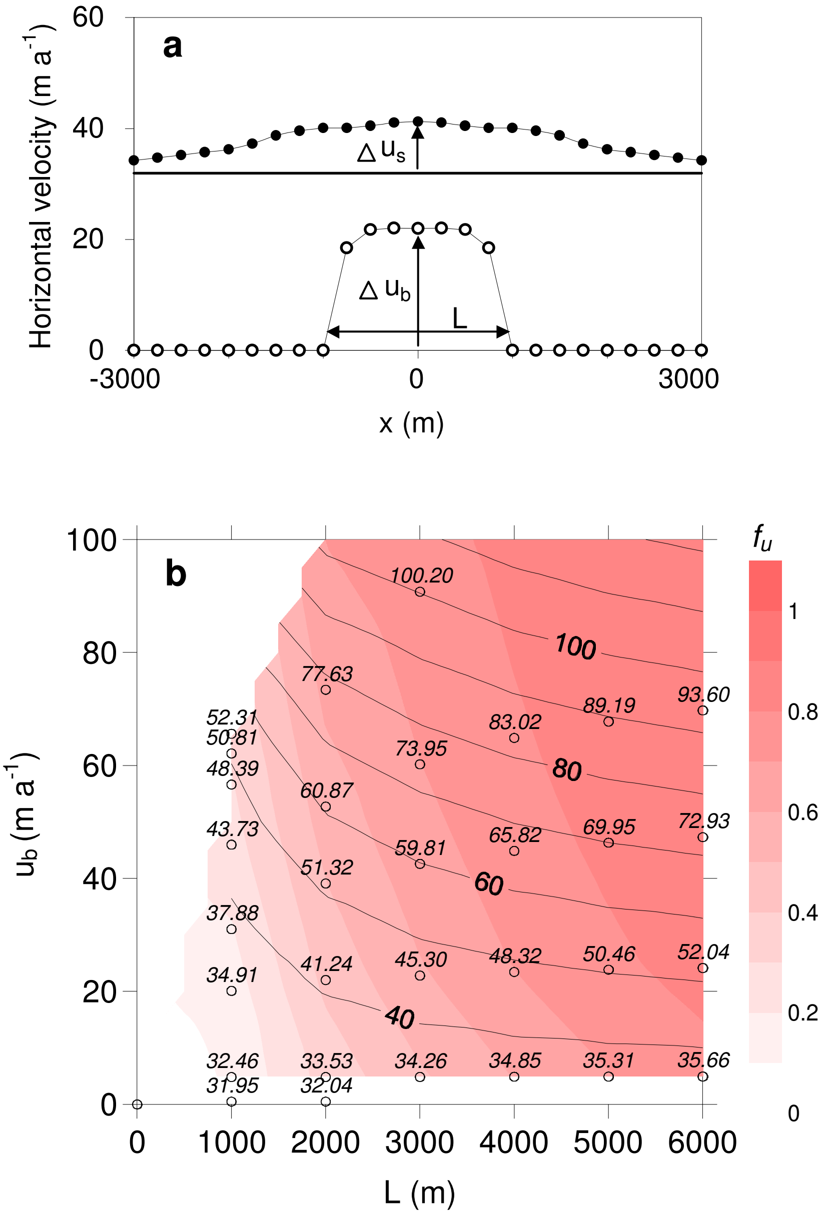

Figure 4.5: *(a) Longitudinal distribution of the horizontal velocity obtained for the sliding condition described in the text. Surface (solid circle) and basal velocities (open circle) were computed at nodes and mid points of the finite-element mesh. Solid line indicates the surface velocity for the non-slip condition. (b) Horizontal surface velocities at $x = 0$ m plotted against the basal velocity u_b at $x = 0$ m and the length of the slippery zone L. The surface velocity is indicated for each experiment with a unit of m a^{-1} and contoured with solid lines. The shaded contours show the transmission factor of horizontal velocity f_u.*

for various sets of viscosity of the sub-basal layer and different lengths of the slippery zone (L). Results are summarized in Figure 4.5b, which shows the horizontal surface velocity u_s and transmission factor of horizontal velocity f_u at $x = 0$ m as functions of L and the basal velocity u_b. As expected, the surface velocity increases with L. The transmission factor of horizontal velocity f_u also increases with L, and becomes larger than 0.75 for $u_b > 5$ m a^{-1} when $L = 6000$ m. In general, f_u varies with L similarly to the analytical solution for a linear medium which was reported by Balise and Raymond (1985), although the values of f_u calculated in this work are slightly smaller. This discrepancy might be caused by an effective material softening close to the glacier bed that introduces non-linearity into the flow law. Blatter and others (1998) used the boundary condition of zero basal shear traction (free slip) in their numerical model and obtained much larger transmission factor than this study.

4.2.2 Transmission of basal strain rate to the surface

In order to examine the transfer of strain rate from the bed to the surface, we assumed the rate factor of the sub-basal layer to vary linearly with x within a region of length L in further numerical experiments. Figure 4.6a shows the longitudinal distribution of the horizontal surface and basal velocities for A' given by

$$c(x) = -0.02x + 50 \quad (\mathrm{m\ a^{-1}\ MPa^{-1}}) \quad -2500 < x < 2500\ (\mathrm{m}). \tag{4.9}$$

Both the longitudinal gradients of horizontal basal and surface velocities were calculated at $x = 0$ m, as well as the transmission factor of longitudinal velocity gradient defined as

$$f_{grad} = \frac{du_s}{dx} / \frac{du_b}{dx}. \tag{4.10}$$

Figure 4.6b shows a contour plot of the surface velocity gradient du_s/dx and f_{grad} for a range of lengths L and basal velocity gradient du_b/dx. The surface velocity gradient increases as the basal gradient and L increase, but the transmission factor is rather small. In this case, the maximum value of f_{grad} is about 0.5 and almost no transmission occurs for L less than 3000 m. This result indicates that observations on a glacier surface cannot be used to determine a small strain rate perturbation at the bed.

4.3 Verification of the Hypotheses Proposed for the Field Observations

4.3.1 Bimodal velocity change against water pressure

The interpretation proposed for the observed bimodal velocity change (hysteresis) against water pressure suggests that ice flow conditions interact across 1.5 km or more in Lauteraargletscher. The credibility of this hypothesis depends on how much a change in basal motion at a point of a glacier influences on surface flow velocity at a horizontal distance of four to five ice thickness. This point was tested with the constructed glacier flow model.

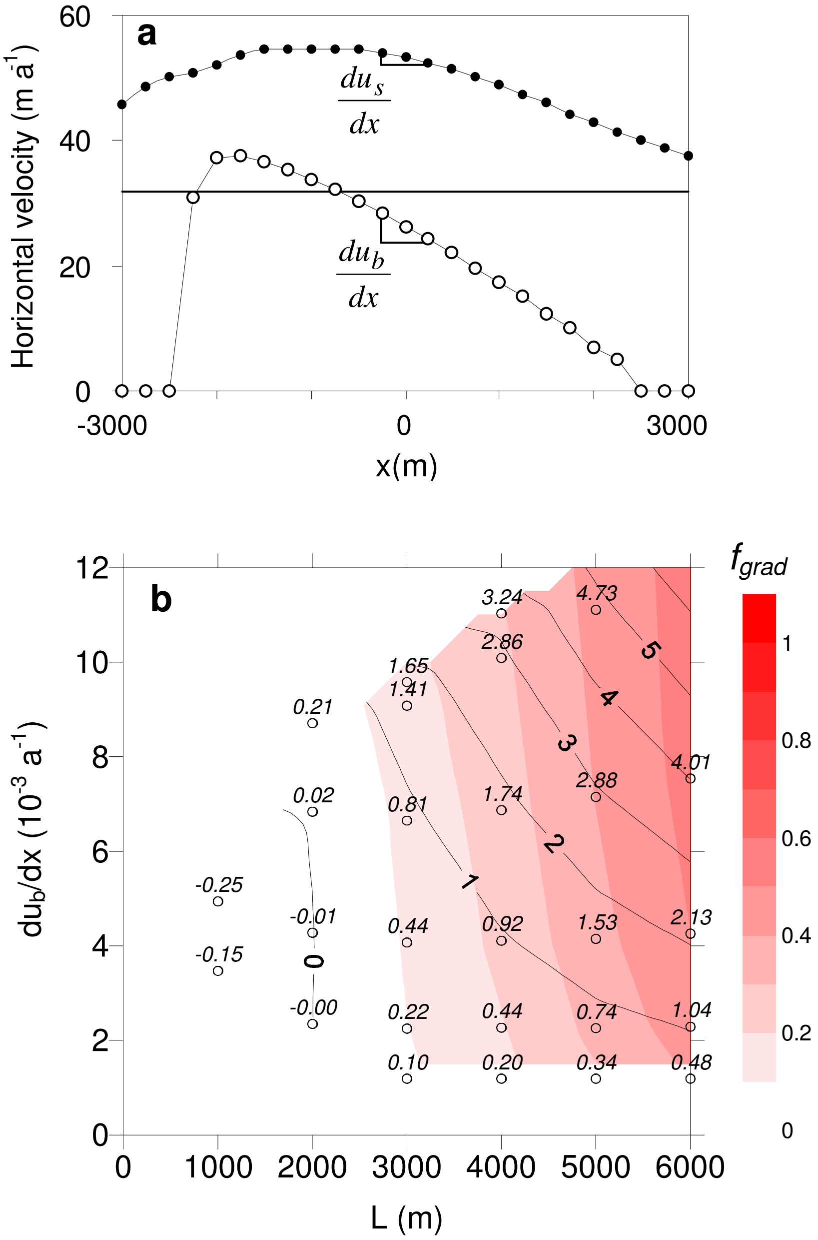

Figure 4.6: *(a) Longitudinal distribution of the surface (solid circle) and basal velocities (open circle) obtained for the sliding condition given by Equation (4.9). The solid line is the surface velocity for the non-slip condition. (b) Longitudinal gradient of the horizontal surface velocity at* $x = 0$ *m plotted against the basal velocity gradient* du_b/dx *at* $x = 0$ *m and the length of the slippery zone* L*. The surface velocity gradient is denoted for each experiment with a unit of* 10^{-3} a^{-1} *and contoured with solid lines. The shaded contours are the transmission factor of longitudinal velocity gradient* f_{grad}*.*

To investigate the influence of basal motion in the upper reach of the glacier on the surface flow at the study site ($x = 0$ m), two different basal flow coefficients were set as constants for $-1000 < x < 1000$ m and $-3000 < x < -1000$ m, and a condition of $u_b = 0$ was given for other regions. These conditions simulate the basal slipperiness distribution along Lauteraargletscher expected during the diurnal velocity variation.

Figure 4.7a shows surface and basal velocity distributions with basal conditions of $c(-1000 < x < 1000) = 100$ and $c(-3000 < x < -1000) = 50$ m a^{-1} MPa^{-1}. Computations were repeated with various sets of the two c values, and then the computed $u_s(x = 0)$ are plotted in Figure 4.7b against basal velocities, $u_b(0)$ and $u_b(-2000)$. The numerical experiments indicate that the surface velocity at a point on the glacier is considerably influenced by the basal motion at 2000 m upglacier. For example, when $u_b(0) = 40$ and $u_b(-2000) = 0$ m a^{-1}, surface velocity is about 50 m a^{-1} which is nearly equivalent to the mean velocity during the observation period in July. If $u_b(-2000)$ increases to 80 m a^{-1} with the same $u_b(0)$, surface velocity $u_s(0)$ is more than 70 m day^{-1}. The almost 50% increase in $u_s(0)$ confirms that local surface velocity can be affected considerably by neighbouring basal motion. To illustrate the effect of neighbouring basal condition, horizontal velocity fields computed for fixed $c(-1000 < x < 1000) = 100$ m a^{-1} MPa^{-1} and various $c(-3000 < x < -1000)$ are shown in Figure 4.8.

Most of the proposed empirical relations between basal velocity, basal shear stress, and the effective pressure are of the form

$$u_b = k\frac{\tau^p}{{P_e}^q}, \tag{4.11}$$

where k is an adjustable parameter, p and q are constants (Budd and others, 1979; Bindschadler, 1983). The comparison of Equation (4.11) with Equation (4.6) yields the relationship between the basal flow coefficient $c(x)$ and the effective pressure. Because q is usually taken as 1, c can be assumed to be directly proportional to ${P_e}^{-1}$. Following the foregoing discussion, another plot of the numerical experiments was made to reproduce the hysteresis in the velocity variation. Figure 4.9 shows the dependences of the surface velocity on the basal condition directly beneath, which are computed for various basal conditions at 2000 m upglacier. The c^{-1} used for abscissa is referred to the local effective pressure to compare the plot with Figure 3.1b. The 20-30% of hysteresis is reproduced as an effect of neighboring basal condition in the realistic velocity range. This result supports the hypothesis that the larger acceleration in the upper reach during the daytime caused the bimodal velocity variation at the study site.

4.3.2 Diurnal variations in the vertical strain

From 26 to 31 July and from 22 to 27 August, clear diurnal variations are observed in vertical strain (Figs. 3.4b and 3.5b). Two-dimensional surface strain rate (Fig. 3.6) also confirms

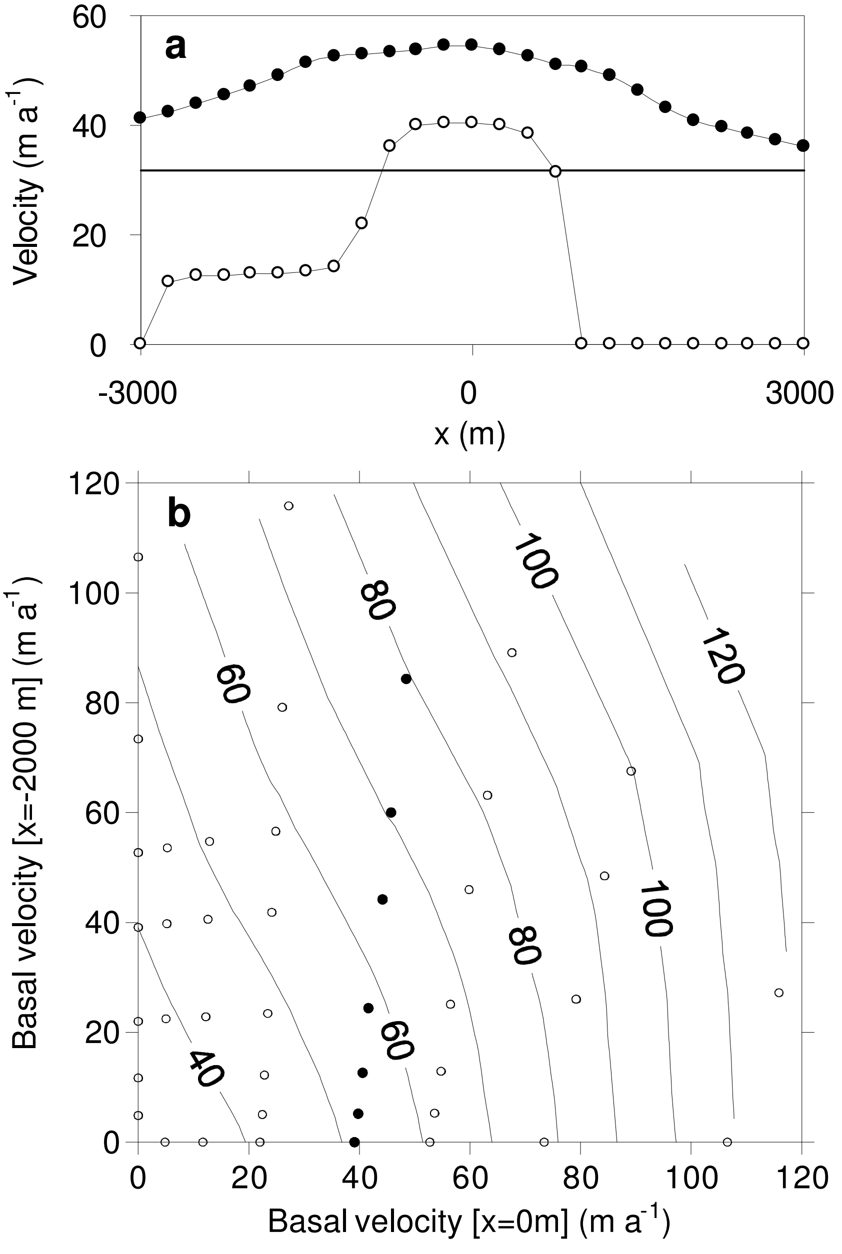

Figure 4.7: *(a) Surface (solid circle) and basal velocity (open circle) distribution computed for the spatially non-uniform basal condition described in the text. (b) Contour line shows the surface velocity at $x = 0$ m in m a^{-1} which are computed for each set of basal velocity at $x = 0$ and -2000 m. Numerical experiments are performed at the conditions shown in (b) with the circles, and the computed horizontal velocity fields at the solid circles are shown in Figure 4.8*

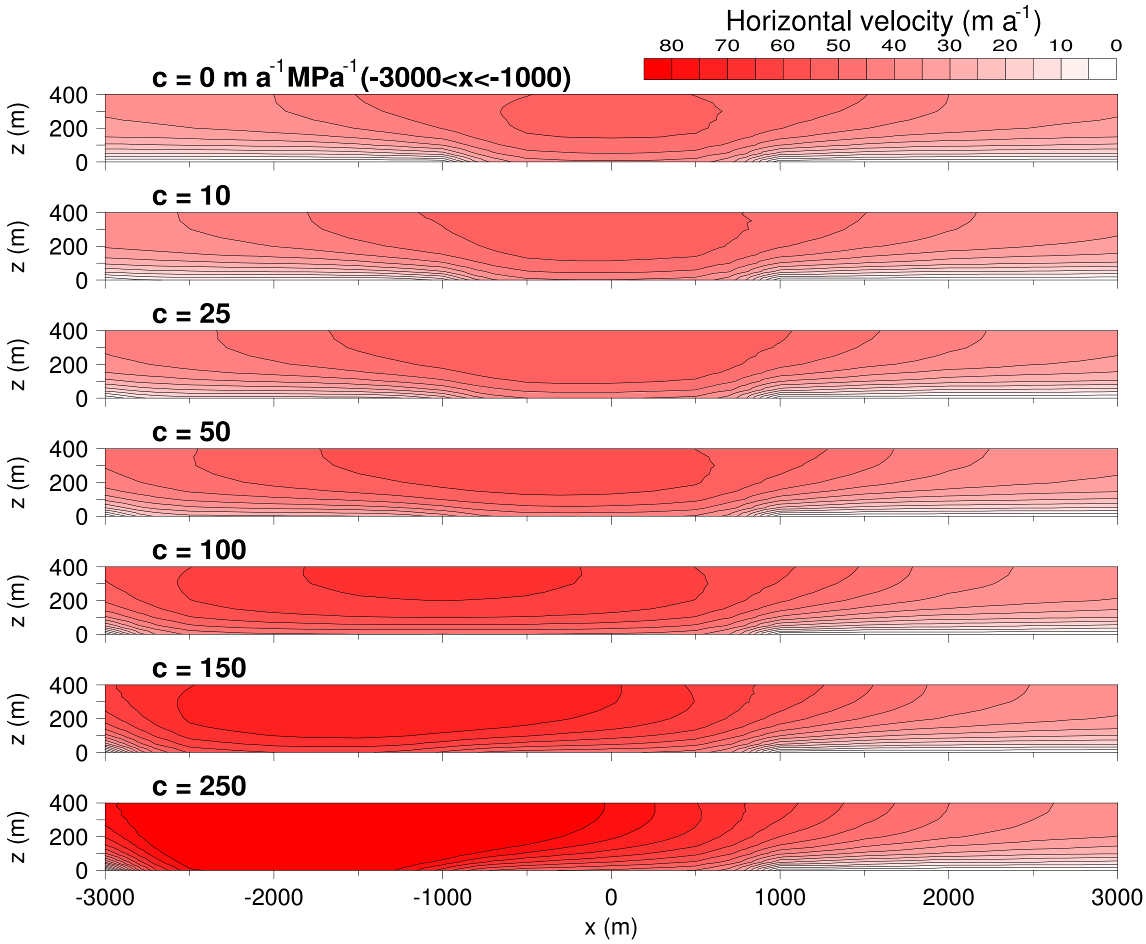

Figure 4.8: *Horizontal velocity fields computed with the basal conditions shown with solid circles in Figure 4.7.* $c(-1000 < x < 1000)$ *is fixed at 100 m* a^{-1} MPa^{-1}*, and* $c(-3000 < x < -1000)$ *is varied in each experiment.*

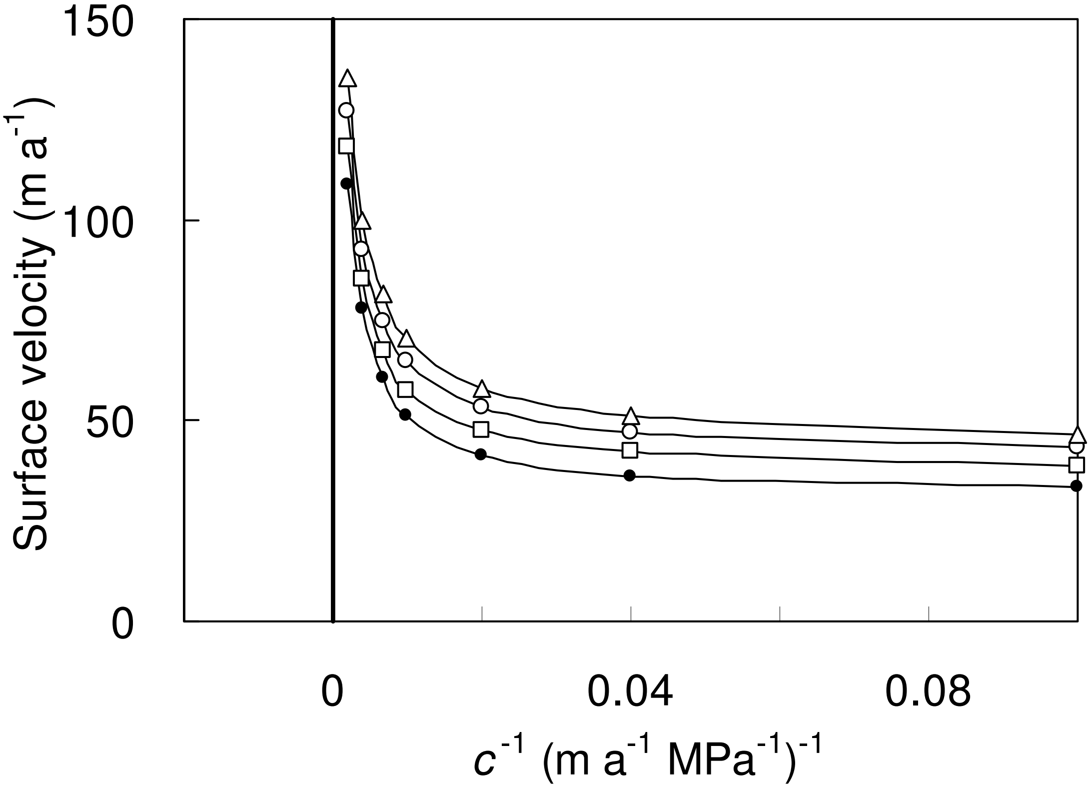

Figure 4.9: *The dependences of surface velocity on the local basal condition represented by* c^{-1}*. The velocities are computed with four different basal conditions at 2000 m upglacier,* $c = 0.0$ *(dot), 100 (square), 200 (circle), and 300 m* a^{-1} MPa^{-1} *(triangle).*

the diurnal changes in the strain regime, and the diurnal vertical displacement of the surface (Fig. 2.8a) is consistent with the measured vertical strain. Because the amplitude of the diurnal variations in the horizontal surface velocity was larger in the upper reach (Fig. 3.2), it is hypothesized in the previous chapter that compressive flow caused the vertical tensile strain during the daytime. ! !

The depth changes of the 283-m-deep borehole by 30-50 mm in July and of the 174-m-deep borehole by 30-40 mm in August are equivalent to vertical strain of 1-2$\times10^{-4}$. These are fairly large deformations corresponding to strain rate of more than 10^{-1} a^{-1}. By using the flow model, the basal conditions required to establish the observed vertical extension and compression are estimated in this section.

As a primary estimate, one can determine the necessary basal velocity gradient to produce the observed strain rate near the surface from Figure 4.6b. However, the observed strain rate is too large to be generated by the velocity gradients in Figure 4.6b. This suggests that the perturbation of slipperiness during the observation periods was even larger than the one used to make Figure 4.6b.

The observed diurnal variations in horizontal surface velocity and its relation to basal pressure variations suggests that the glacier became partly decoupled from the bed during the daytime. This may be due to increased basal cavity formation or due to the failure of a thin till layer. If such a decoupled zone begins to develop upstream of the measurement site and subsequently expands downglacier with increasing sliding velocity in the course of the day, large deviatoric stresses and vertical strain rates can develop near the surface as observed in Figures 4.4c and d. Such temporal evolution of a decoupled zone can be simulated by prescribing corresponding basal conditions in the flow model. The sliding magnitude, spatial size, and the position of the slippery zone were varied to fit the observed velocities and strain rates at the study site as close as possible. Because the observed diurnal changes in thickness are only a few centimeters at most, changes in thickness and surface slopes can be ignored in the modeling calculations, and the diurnal variations can be analyzed without changing the model geometry.

The vertical strain rate and surface velocity variations measured on 25 August 2001 are chosen as an example, and simulated by numerical experiments. A slippery zone is introduced upstream of the observation site by changing the rate factor of the sub-basal layer. By subsequently changing the slipperiness, size and position of the slippery zone, the observed spatial and temporal pattern in vertical strain rate could be reproduced qualitatively. Figures 4.10 and 4.11 show the evolution of horizontal velocity and vertical strain rate fields calculated for the slippery zones prescribed for each time of the day. Surface and basal velocity distribution is summarized in Figures 4.12a and b. The condition of the slippery zone at each time of the day was determined by adjusting the distribution of c to fit the observed surface velocity at the study site. The temporal evolution of the slippery zone is explained as follows. The slippery zone starts to develop upstream of the observation site at about 8:00 when the surface melting starts. Then it increases in extent and magnitude, and forms a sliding boundary beneath the study site at 15:00. In the evening, when the surface-melting rate decreases, the basal velocity starts to decrease and the zone moves downglacier during the period of 18:00-0:00. This downglacier propagation is due to the subglacial water drainage towards the glacier terminus. Eventually, compressive flow at the study site is replaced with a weaker extending flow (3:00-6:00).

Figure 4.13 compares the field measurements on 25 August with the computed temporal variations of horizontal surface velocity and vertical strain rate in the upper 200 m of the ice at the study site ($x = 0$ m). Even though the computed strain rates are still considerably smaller than the measured ones, they are an order of magnitude larger than those obtained

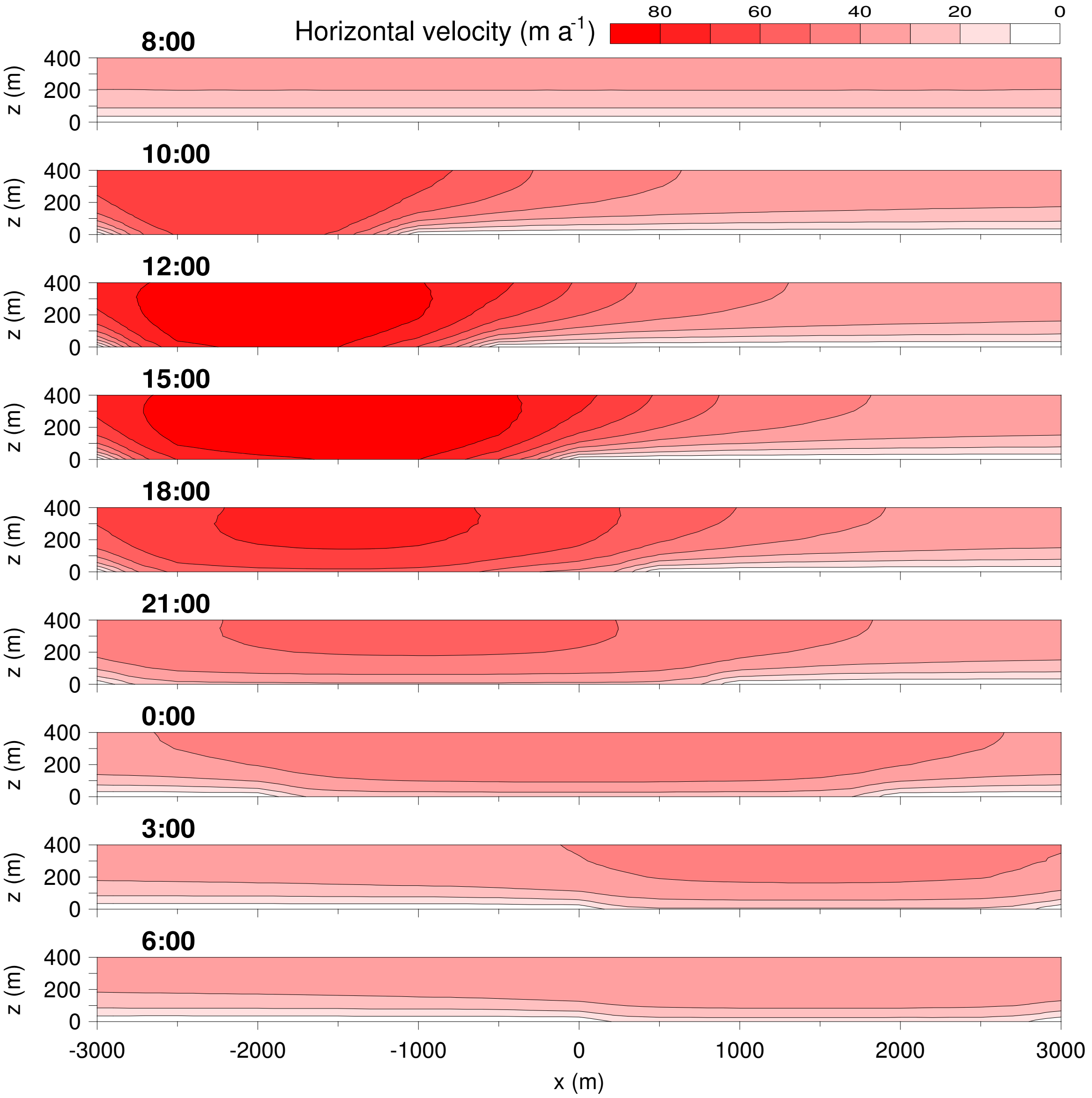

Figure 4.10: *Diurnal evolution of horizontal velocity fields computed for the basal condition scenario described in the text.*

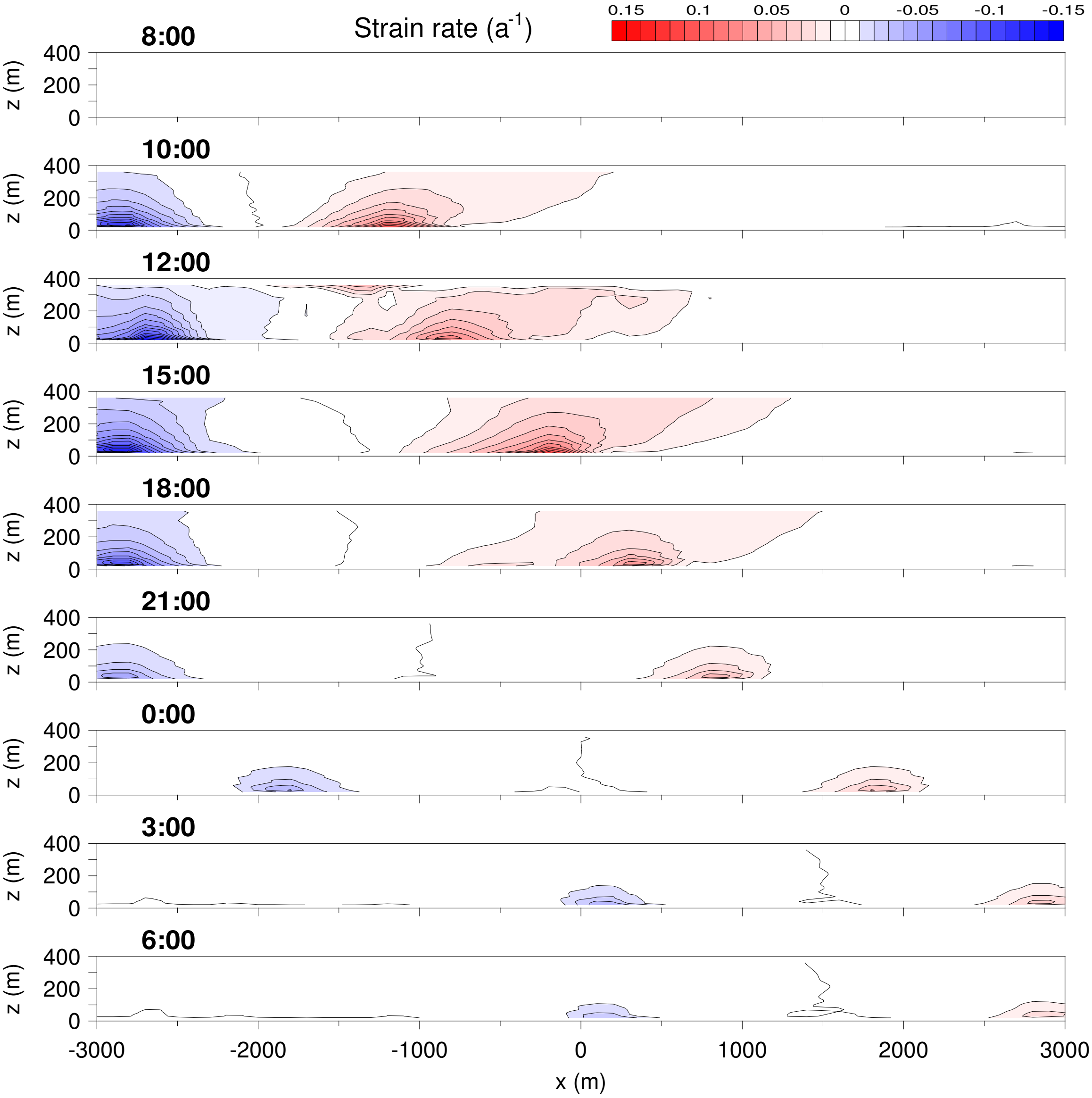

Figure 4.11: *Diurnal evolutions of vertical strain rate fields computed for the basal condition scenario described in the text.*

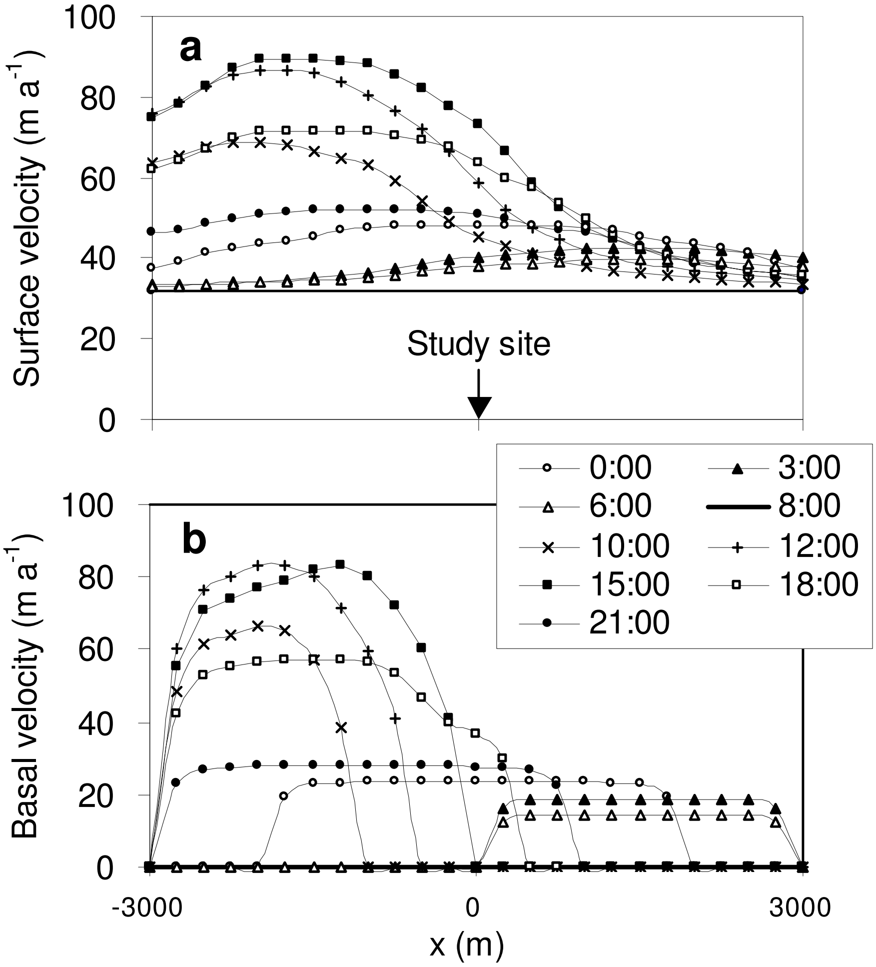

Figure 4.12: *Diurnal evolutions of (a) surface and (b) basal velocity distributions computed for the basal condition scenario described in the text.*

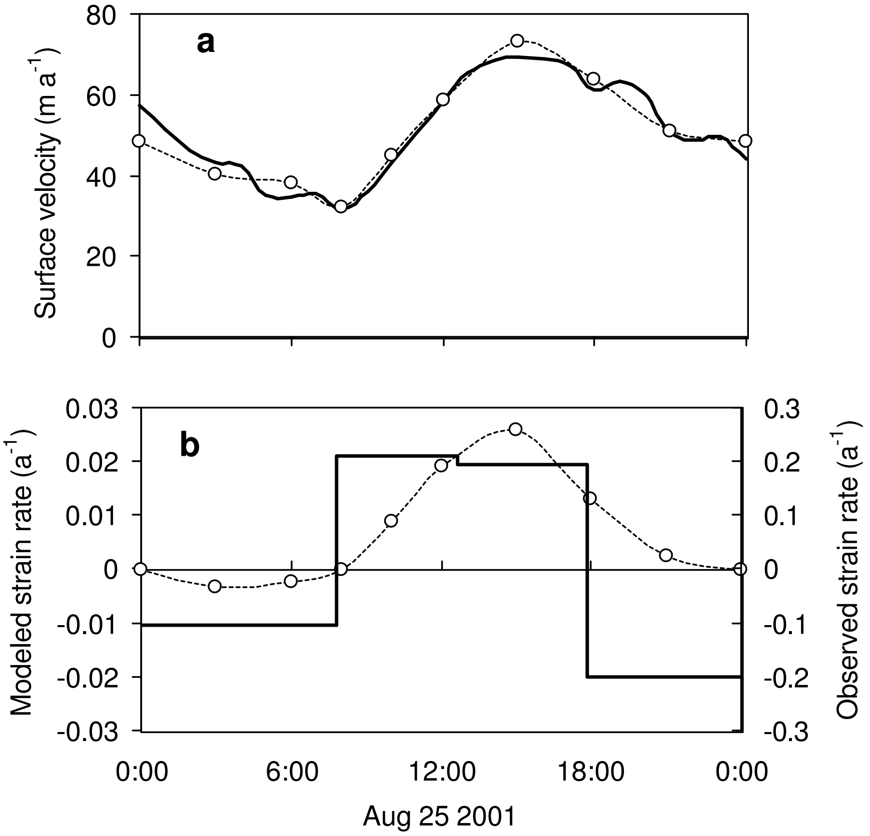

Figure 4.13: *(a) Diurnal variations of (a) horizontal surface velocity and (b) vertical strain rate. Open circles with the dashed line are model results and the solid lines are measurements data taken on Unteraargletscher on August 25 2001. Vertical strain rate is computed as the mean for the upper 200-m of the glacier, and measurements were taken from a 174-m deep borehole and plotted with the scale magnified 10 times.*

in Figure 4.6b.

The fact that the computed strain rate accounts for only about 10% of the measured borehole depth change shows that some important aspects of the flow are not described adequately by the model. To obtain larger strain rates, the model could assume higher flow velocities in the upper region, but this assumption would contradict observed surface velocities. Another possibility is that the flow law used is incorrect. In the present model, stress concentration near the surface in Figure 4.4c does not generate clear strain rate concentration in Figure 4.4d. This is because Glen's flow law (Equation (4.3)) gives much higher effective viscosity as the effective stress decreases near the glacier surface. To assess the influence of effective viscosity near the surface, another experiment was carried out with a modified Glen's flow law,

$$\dot{\varepsilon}_{ij} = A(\tau_e^{n-1} + \tau_0^{n-1})\tau_{ij}. \tag{4.12}$$

Here, as elsewhere, an arbitrary small constant value τ_0 has been introduced in the flow law to avoid mathematical singularity where the effective viscosity is infinite when the effective stress vanishes (Hutter, 1983; Blatter, 1995). It was confirmed that the influence of τ_0 is negligible when $\tau_0 \leq 10^{-2}$ MPa, and $\tau_0 = 10^{-2}$ MPa has been taken in the numerical experiments so far. Now, τ_0 is set to be 0.1 MPa so that ice becomes less viscous near the glacier surface. In Equation (4.12), strain rate components are linear functions of corresponding stress components when the effective stress is very small, while it obeys Glen's flow law under a high stress condition. This modified flow law was applied to the basal conditions identical to those used for Figure 4.4. Computed fields of flow velocities, stress, and strain rate are shown in Figure 4.14 and compared with Figure 4.4. It is interesting to see the vertical strain increases near the surface while the deviatoric stress decreases (Fig. 4.14c and d). The stress near the surface seems to be transfered to the deeper region where ice becomes more viscous after the flow law was modified. The results suggests that the modeled vertical strain is improved by Equation (4.12), but the improvement is still insufficient owing to the reduction in the stress. Further study on the flow-law exponent or flow law itself is required to interpret the field data sufficiently. The model will be also improved including the average longitudinal strain and transverse stresses over the area in question.

The studied velocity variation accompanied by a strain rate anomaly is similar in nature to the *mini-surges* or propagation of enhanced motion waves observed in Variegated Glacier (Raymond and Malone, 1986; Kamb and Engelhardt, 1987). Balise and Raymond (1985) applied their analytical analysis of a linear viscous flow to interpret the measurements on the surface of Variegated Glacier by a propagation of basal velocity anomaly that was much sharper than the one used in this study for Figure 4.12b. They suggest that the vertical straining of ice might also explain uplift events observed during fast flow periods. In order to apply the flow model used in this work to uplift events, quantitative discussion described

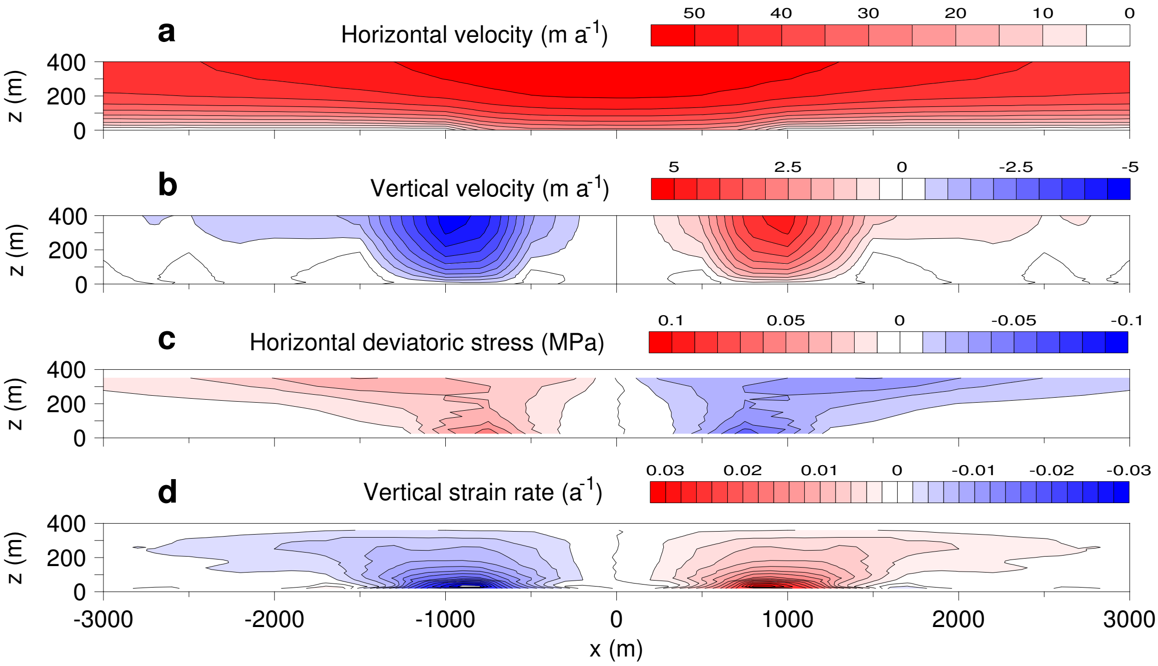

Figure 4.14: *Computed fields of (a) horizontal velocity, (b) vertical velocity, (c) longitudinal deviatoric stress component* τ_{xx}*, and (d) vertical strain rate. Modified flow law (Equation (4.12)) was used with the basal conditions identical to those in Figure 4.4.*

above is crucial. It is because the uplift rates measured in this study, in Variegated Glacier (Kamb and Engelhardt, 1987) and in Unteraargletscher by Iken and others (1983) are all in the same order of $\sim 10^{-4}$ day^{-1} if they are converted to the vertical strain rate over the ice thickness, which is larger than the modelled result in Figure 4.13b.

4.4 Summary

A finite-element non-linear viscous flow model was developed to simulate two dimensional glacier flow fields under the influence of spatially distributed basal slipperiness. A basal motion was introduced by a conceptional sub-glacial deformable thin layer, and the slipperiness was prescribed with a rate factor of the layer. The model was used to study the effects of local perturbation in basal slipperiness on the surface velocity and the englacial strain-rate distribution.

The numerical experiments show that the transmission of the basal motion to the surface is strongly dependent on the horizontal spatial scale of the basal perturbation. Influence of the basal motion reaches out of the slippery zone to approximately 10 times ice thickness. Near the boundary of slip/non-slip conditions, a significant stress field is established and the stress is strongest near the glacier surface.

The model results were compared with the measurements of surface velocity and vertical strain rate variations at Lauteraargletscher. It is shown that the surface velocity cannot be determined by the local basal slipperiness alone but is considerably affected by the neighbouring basal conditions. The hysteresis of 20-30% observed in the surface velocity against water pressure was reproduced by assuming different basal slipperiness at 2000 m upper reach from the study site.

The downglacier propagation of a slippery zone is able to qualitatively explain the observed temporal variations in the surface velocity and the vertical strain rate. However, quantitative comparison between the model prediction and the field measurement show that calculated vertical strain rates are about an order-of-magnitude too small. The reason for this discrepancy remains unclear, but a possible reason for the discrepancy is that the modeled ice near the surface is too stiff. This stiffness may arise from ignoring the average longitudinal strain which is established by the real glacier geometry, or because the flow-law exponent of ice varies with stress.

CHAPTER 5

CONCLUSION

5.1 Field Measurements

Field measurements were carried out intensively in a temperate valley glacier during the ablation season to investigate flow variations under the control of basal conditions. The measurements were conducted with high temporal resolution focusing on short-term variations in horizontal surface velocity, surface vertical displacement (uplift), and vertical strain.

Surface velocity was well correlated with subglacial water pressure in July and August (Figs. 3.4a, 3.5a). It is shown that the water pressure is the most important factor which controls short-term glacier flow variation in the ablation season. There is a clear relationship between surface velocity and water pressure, in which the velocity increases as a power function (Equation (3.2)) of the effective pressure with an asymptote at $P_e = 0$. This result agrees with the previously reported field observations and theoretical predictions. Pressure dependence of the surface velocity was not identical in pressure increasing and decreasing phase. This bimodal velocity variation suggests that the study site flows under the influence of surrounding basal conditions.

Surface uplifts of as much as 100 mm were observed from June to August over time scales of an hour to a few days. They occurred in the periods of fast glacier flow associated with high water pressure, and the detail analysis with borehole depth measurement (Fig. 3.7) indicates two different mechanisms of the uplifts. Most of the uplifts were caused by vertical straining due to a compressive flow established by spatially non-uniform basal condition. In the case of the motion event observed in June, however, the volume of the basal water cavities increased and it lifted the glacier upward.

Short-term variations in vertical strain, including diurnal variations, were observed. During the observation in the late July and August, vertical strain was tensile in the daytime and compressive at night (Figs. 3.4b and 3.5b). Two-dimensional surface strain also showed diurnal changes in the strain regime, and the horizontal compression along the flow line during the daytime is consistent with the tensile vertical strain (Fig. 3.6). These observations are interpreted as the results of compressive flow which is enhanced by the larger acceleration in the upper reach during the daytime. It is concluded that internal ice deformation is not a constant component in glacier flow within time scales of hours to days.

Subglacial water pressure is shown to be the most influential factor of flow variations during the ablation season. Short-term water pressure variations at Lauteraargletscher showed two distinctive manners in the field observation operated throughout the summer. Diurnal variation is not prominent and sudden water input by precipitation raises the pressure up to the overburden level in the early summer, while the amplitude in the diurnal variation is large and the pressure is insensitive to precipitation in the late summer. The transition from one to the other pattern originates from the seasonal evolution in the subglacial hydraulic condition. It is suggested that the subglacial drainage efficiency increases after the seasonal snow line ascends upglacier, and subsequent increase in the drainage efficiency enhances diurnal pressure variation.

5.2 Numerical Investigation

A glacier flow model was developed to compute two-dimensional flow fields with various basal boundary conditions. Experiments with a basal slippery zone indicate that the influence of local basal motion can reach as far as 10 times ice thickness. This result verifies the hypothesis that the hysteresis of the surface velocity against the local water pressure is caused by the pushing force conveyed from a few kilometers upper reach, where ice flows faster when water pressure increases at the study site. The effect of the spatial distribution of slipperiness on englacial vertical strain is also investigated with numerical experiments. By setting a slippery zone in the upper reach of the glacier and shifting it downglacier with a diurnal cycle, the observed diurnal variations in vertical strain rate was reproduced qualitatively (Fig. 4.13). Inspection of the stress and strain fields shows that significant deviatoric stress is generated near the surface by the slippery zone (Fig. 4.4c), and it takes an important role in the strain regime in a glacier.

5.3 Future Prospects of the Study

The methods of high resolution glacier flow measurements were developed in this work. As the next step of the study, it is beneficial to carry out similar measurements at a number of sites on a glacier. The distance between the measurement sites should be determined from the objective of the study. According to the results of the presented numerical investigation, intervals of about 10 times ice thickness are adequate to view the general flow distribution in a glacier, whereas shorter intervals are required to look into the details of the local flow regime. The observations in this study showed that the most dramatic change in the flow regime takes place at the altitude of the seasonal snow line. This is due to the change in the surface condition from snow to ice and rapid development of subglacial drainage efficiency. Thus, measurements can be focused on such region on a glacier by setting instruments with shorter spatial intervals near the snow line. This effort may reveal the distinctive flow regimes below and above the snow line altitude, and show the boundary of the regimes ascend upglacier with the snow line.

Because it was shown that subglacial water pressure takes the most important role in short-term flow variations during the ablation season, hydrological experiments in conjunction with flow measurements are recommended. Measurement of water drainage from the glacier and tracer experiment will give information on the development of the subglacial drainage system. The spatial distribution of subglacial water pressure should be measured to confirm the difference in the subglacial condition below and above the snow line.

The development of a three-dimensional version of the flow model is a challenging task but worthwhile to be accomplished. The surface strain regime measured in this study requires further examination of transverse stress and strain components. Moreover, effect of side drag becomes more important for the flow regime when the bed is lubricated. Truffer and others (2001) suggested that the basal stress is transfered to the glacier side margins when a valley glacier is lubricated at the bed. The influence of side drag is also important in ice streams (Raymond, 1996; Jackson and Kamb, 1997; Tulaczyk and others, 2000b). Thus, inclusion of the transverse components makes the model applicable not only for valley glaciers but also for the streaming flow in ice sheets.

Owing to its flexibility to deal with uneven boundaries and non-uniform grid spacings, the finite-element method is an ideal tool to solve the flow field with a realistic bed and surface topography. Gudmudsson (1999) developed a three dimensional finite-element glacier flow model with topographical information of Unteraargletscher, and investigated the flow feature in the confluence area. Combined with the realistic basal boundary condition used in this study, a three dimensional finite-element flow model acquires a potential to solve problems in a wide range from a mountain glacier flow in a narrow valley to a streaming flow in ice sheets.

The simulation of the diurnal vertical strain rate suggested the possibility that Glen's flow law is not always the correct form of the constitutive equation. Stress-strain relationship should be further studied under low stress condition to find a more adequate flow law. The quality of a glacier flow modelling will be further improved by including the effect of ice anisotropy (Azuma, 1995; Thorsteinsson, 2001), water concentration, sediment and impurity inclusions (Hooke and others, 1972; Lawson 1996).

REFERENCES

Agassiz, L. 1840. *Études sur Glaciers.* (English translated version is published from Hafner Publishing Company, New York and London).

Azuma, N. 1995. A flow law for anisotropic polycrystalline ice under uniaxial compressive deformation. *Cold Reg. Sci. Technol.*, **23**(2), 137-147.

Bahr, D. B., W. T. Pfeffer and M. F. Meier. 1994. Theoretical limitations to englacial velocity calculations. *J. Glaciol.*, **40**(136), 509-518.

Balise, M. J. and C. F. Raymond. 1985. Transfer of basal sliding variations to the surface of a linearly viscous glacier. *J. Glaciol.*, **31**(109), 308-318.

Bassi, A. 1999. Messungen der Oberflächengeschwindigkeitsänderungen des Unteraargletschers, Berner Alpen mit hoher räumlicher und zeitlicher Auflösung. (Diplomarbeit, Abteilung fü Erdwissenschaften, ETH, Zürich.) (In German).

Bauder, A. 2001. Bestimmung der Massenbilanz von Gletschern mit Fernerkundungsmethoden und Fliessmodellierungen: Eine Sensitivitätsstudie auf dem Unteraargletscher. *Mitteilung*, **169**, Versuchsanstalt für Wasserbau, Hydrology und Glaziologie der ETH Zürich.

Bindschadler, R. 1983. The importance of pressurized subglacial water in separation and sliding at the glacier bed. *J. Glaciol.*, **29**(101), 3-19.

Blake, E. W., U. H. Fisher, and G. K. C. Clarke. 1994. Direct measurement of sliding at the glacier bed. *J. Glaciol.*, **40**(136), 595-599.

Blankenship, D. D., R. Bentley, S. T. Rooney and R. B. Alley. 1986. Seismic measurements reveal a saturated, porous layer beneath an active Antarctic ice stream. *Nature*, **322**, 54-57.

Blatter, H. 1995. Velocity and stress fields in grounded glaciers: a simple algorithm for including deviatoric stress gradients. *J. Glaciol.*, **41**(138), 333-344.

Blatter, H., G. K. C. Clarke and J. Colinge. 1998. Stress and velocity fields in glaciers: part II. Sliding and basal stress distribution. *J. Glaciol.*, **44**(148), 457-466.

Boulton, G. S. and R. C. A. Hindmarsh. 1987. Sediment deformation beneath glaciers: rheology and geological consequences. *J. Geophys. Res.*, **92**(B9), 9059-9082.

Budd, F., P. L. Keage and N. A. Blundy. 1979. Empirical studies of ice sliding. *J. Glaciol.*, **23**(89), 157-170.

Colinge, J. and J. Rappaz. 1999. A strongly nonlinear problem arising in glaciology. *Rairo-Math. Model Num.*, **33**(2), 395-406.

Copland, L., J. Harbor and M. Sharp. 1997. Borehole video observation of englacial and basal ice conditions in a temperate valley glacier. *Ann. Glaciol.*, **24**, 277-282.

Engelhardt, H. and B. Kamb. 1997. Basal hydraulic system of a West Antarctic ice stream: constraints from borehole observations. *J. Glaciol.*, **43**(144), 207-230.

Engelhardt, H. and B. Kamb. 1998. Basal sliding of Ice stream B, West Antarctica. *J. Glaciol.*, **44**(147), 223-230.

Fischer, U. H., P. R. Porter, T. Schuler, A. J. Evans and G. H. Gudmundsson. 2001. Hydraulic and mechanical properties of glacial sediments beneath Unteraargletscher, Switzerland: implications for glacier basal motion. *Hydrol. Process*, **15**(18), 3525-3540.

Funk, M., G. H. Gudmundsson and F. Hermann. 1994. Geometry of the glacier bed of the Unteraargletscher, Bernese Alps, Switzerland. *Z. Gletscherkd. Glazialgeol.*, **30**, 187-194.

Glen, J. W. 1952. Experiments on the deformation of ice. *J. Glaciol.*, **2**, 111-114.

Glen, J. W. 1955. The creep of polycrystalline ice. *Proc. R. Soc. London Ser. A*, **228**(1175), 519-538.

Gudmundsson, G. H. 1999. A three-dimensional numerical model of the confluence area of Unteraargletscher, Bernese Alps, Switzerland. *J. Glaciol.*, **45**(150), 219-230.

Gudmundsson, G. H. 2002. Observations of a reversal in vertical and horizontal strain-rate regime during a motion event on Unteraargletscher, Bernese Alps, Switzerland. *J. Glaciol.*, in press.

Gudmundsson, G. H. 2003. Transmission of basal variability to a glacier surface. *J. Geophys. Res.*, in press.

Gudmundsson, G. H. and A. Bauder. 1999. Towards an indirect determination of the mass-balance distribution of glaciers using the kinematic boundary condition, *Geogr. Ann.*, **81A**, 575-583.

Gudmundsson, G. H., A. Iken and M. Funk. 1997. Measurements of ice deformation at the confluence area of Unteraargletscher, Bernese Alps, Switzerland. *J. Glaciol.*, **43**(145), 548-556.

Gudmundsson, G. H., C. F. Raymond and R. Bindschadler. 1998. The origin and longevity of flow stripes on Antarctic ice streams. *Ann. Glaciol.*, **27**, 145-152.

Gudmundsson, G. H., A. Bauder, M. Lüthi, U. H. Fischer and M. Funk. 1999. Estimating rates of basal motion and internal ice deformation from continuous tilt measurements. *Ann. Glaciol.*, **28**, 247-252.

Gudmundsson, G. H., A. Bassi, M. Vonmoos, A. Bauder, U. H. Fischer and M. Funk. 2000. High-resolution measurements of spatial and temporal variations in surface velocities of Unteraargletscher, Bernese Alps, Switzerland. *Ann. Glaciol.*, **31**, 63-68.

Haefeli, R. 1970. Changes in the behaviour of the Unteraargletscher in the last 125 years. *J. Glaciol.*, **9**(56), 195-212.

Hanson, B., R. L. Hooke and E. M. Grace, Jr. 1998. Short-term velocity and water pressure variations down-glacier from a riegel, Storglaciären, Sweden. *J. Glaciol.*, **44**(147), 359-367.

Harper, J. T., N. F. Humphrey and W. T. Pfeffer. 1998. Three-dimensional deformation measured in an Alaskan glacier. *Science*, **281**, 1340-1342.

Harrison, W. D., K. A. Echelmeyer and H. Engelhardt. Short-period observations of speed, strain and seismicity on Ice Stream B, Antarctica. *J. Glaciol.*, **39**(133), 463-470.

Hofmann-Wellenhof, B., H. Lichtenegger and J. Collins. 2000. *GPS theory and practice. Fifth edition.* Wien New York, Springer-Verlag.

Hooke, R. L., B. B. Dahlin and M. Kauper. 1972. Creep of ice containing dispersed fine sand. *J. Glaciol.*, **11**(63), 327-336.

Hooke, R. L., P. Calla, P. Holmlund, M. Nilsson and A. Stroeven. 1989. A 3 year record of seasonal variations in surface velocity, Storglaciären, Sweden. *J. Glaciol.*, **35**(120), 235-247.

Hooke, R. L., B. Hanson, N. R. Iverson, P. Jansson and U. H. Fischer. 1997. Rheology of till beneath Storglaciären, Sweden. *J. Glaciol.*, **43**(143), 172-179.

Hubbard, A., H. Blatter, P. Nienow, D. Mair and B. Hubbard. 1998. Comparison of a three-dimensional model for glacier flow with field data from Haut Glacier d'Arolla, Switzerland. *J. Glaciol.*, **44**(147), 368-378.

Hutter, K. 1983. *Theoretical glaciology: material science of ice and the mechanics of glaciers and ice sheets.* Dordrecht, etc., D. Reidel Publishing Co./ Tokyo, Terra Scientific Publishing Co.

Iken, A. 1981. The effect of the subglacial water pressure on the sliding velocity of a glacier in an idealized numerical model. *J. Glaciol.*, **27**(97), 407-421.

Iken, A. 1988. Adaption of the hot-water-drilling method for drilling to great depth. *Mitteilung*, **94**, pp. 211-229, Versuchsanstalt für Wasserbau, Hydrology und Glaziologie der ETH Zürich.

Iken, A. and R. A. Bindschadler. 1986. Combined measurements of subglacial water pressure and surface velocity of Findelengletscher, Switzerland: conclusions about drainage system and sliding mechanism. *J. Glaciol.*, **32**(110), 101-119.

Iken, A., H. Röthlisberger, A. Flotron and W. Haeberli. 1983. The uplift of Unteraargletscher at the beginning of the melt season —a consequence of water storage at the bed? *J. Glaciol.*, **29**(101), 28-47.

Iverson, N. R., B. Hanson, R. L. Hooke and P. Jansson. 1995. Flow mechanism of glaciers on soft beds. *Science*, **267**, 80-81.

Iverson, N. R., T. S. Hooyer and R. W. Baker. 1998. Ring-shear studies of till deformation: Coulomb-plastic behavior and distributed strain in glacier beds. *J. Glaciol.*, **44**(148), 634-642.

Iverson, N. R., R. W. Baker, R. L. Hooke, B. Hanson and P. Jansson. 1999. Coupling between a glacier and a soft bed: I. A relation between effective pressure and local shear stress determined from till elasticity. *J. Glaciol.*, **45**(149), 31-40.

Jackson, M. and B. Kamb. 1997. The marginal shear stress of Ice Stream B, West Antarctica. *J. Glaciol.*, **43**(145), 415-426.

Jaeger, J. C. 1969. *Elasticity, fracture and flow: with engineering and geological applications. Third edition.* pp. 23-33, Methuen & Co. Ltd., London.

Jansson, P. 1995. Water pressure and basal sliding on Storglaciären, northern Sweden. *J. Glaciol.*, **41**(138), 232-240.

Kamb, B. 1970. Sliding motion of glaciers: theory and observation. *Rev. Geophys. Space Phys.*, **8**(4), 673-728.

Kamb, B. 2001. Basal zone of the West Antarctic ice streams and its role in lubrication of their rapid motion. *The west Antarctic ice sheet, behavior and environment. ed. by R. B. Alley and R. A. Bindschadler*, Antarctic research series, **77**, American Geophysical Union, Washington, D. C.

Kamb, B. and H. Engelhardt. 1987. Waves of accelerated motion in a glacier approaching surge: the mini-surges of Variegated Glacier, Alaska, U.S.A. *J. Glaciol.*, **33**(113), 27-46.

Knecht, H. and A. Süsstrunk, 1952. Bericht über die seismischen Sondierungen der schweizerischen Gletscherkommission auf dem Unteraargletscher, 1936-1950. Sion, Switzerland, Grande Dixence S.A. (Bericht No. 512.)

Lawson, W. 1996. The relative strength of debris-laden basal ice and clean ice: some evidence from Taylor Glacier, Antarctica. *Ann. Glaciol.*, **23**, 270-276.

Lliboutry, L. 1968. General theory of subglacial cavitation and sliding of temperate glaciers. *J. Glaciol.*, **7**(49), 21-58.

Mair, D., P. Nienow, I. Willis and M. Sharp. 2001. Spatial patterns of glacier dynamics during a high-velocity event: Haut Glacier d'Arolla, Switzerland. *J. Glaciol.*, **47**(156), 9-20.

Mair, D. W. F., M. J. Sharp and I. C. Willis. 2002. Evidence for basal cavity opening from analysis of surface uplift during a high-velocity event: Haut Glacier d'Arolla, Switzerland. *J. Glaciol.*, **48**(161), 208-216.

Naruse, R., H. Fukami and M. Aniya. 1992. Short-term variations in flow velocity of Glacier Soler, Patagonia, Chile. *J. Glaciol.*, **38**(128), 152-156.

Nienow, P. W., M. J. Sharp and I. C. Willis. 1998. Seasonal changes in the morphology of the subglacial drainage system, Haut Glacier d'Arolla, Switzerland. *Earth Surf. Process. Land.*, **23**, 825-843.

Nolan, M. and K. Echelmeyer. 1999. Seismic detection of transient changes beneath Black Rapids Glacier, Alaska, U.S.A.: I. Techniques and observations. *J. Glaciol.*, **45**(149), 119-131.

Nye, J. F. 1953. The flow law of ice from measurements in glacier tunnels, laboratory experiments and the Jungfraufirn borehole experiment. *Proc. R. Soc. London Ser. A*, **219**, 477-489.

Nye, J. F. 1965. The flow of a glacier in a channel of rectangular, elliptic or parabolic cross-section. *J. Glaciol.*, **5**(41), 661-690.

Nye, J. F. 1969. A calculation of the sliding of ice over a wavy surface using a Newtonian viscous approximation. *Proc. R. Soc. London Ser. A*, **311**, 445-467.

Paterson, W. S. B. 1994. *The physics of glaciers. Third edition.* pp. 251, Butterworth-Heinemann, Oxford.

Pohjola, V. A. 1993. TV-video observation of bed and basal sliding on Storglaciären, Sweden. *J. Glaciol.*, **39**(131), 111-118.

Raymond, C. F. 1971. Flow in a transverse section of Athabasca Glacier, Alberta, Canada. *J. Glaciol.*, **10**(58), 55-84.

Raymond, C. F. 1996. Shear margins in glaciers and ice sheets. *J. Glaciol.*, **42**(140), 90-102.

Raymond, C. F. and S. Malone. 1986. Propagating strain anomalies during mini-surges of Variegated Glacier, Alaska, U.S.A. *J. Glaciol.*, **32**(111), 178-191.

Röthlisberger, H. and A. Iken. 1981. Plucking as an effect of water-pressure variations at the glacier bed. *Ann. Glaciol.*, **2**, 57-61.

Schweizer, J. and A. Iken. 1992. The role of bed separation and friction in sliding over an undeformable bed. *J. Glaciol.*, **38**(128), 77-92.

Sugiyama, S. 2003. Influence of surface debris on summer ablation in Unteraar- and Lauteraargletscher, Switzerland. *Bulletin of Glaciological Research*, **20**, 41-47.

Sugiyama, S. and G. H. Gudmundsson. 2003. Diurnal variations in vertical strain observed in a temperate valley glacier. *Geophys. Res. Lett.*, **30**(20), 1090.

Sugiyama, S., G. H. Gudmundsson and J. Helbing. 2003. Numerical investigation of the effects of temporal variations in basal lubrication on englacial strain-rate distribution. *Ann. Glaciol.*, **37**, in press.

Thorsteinsson, T. 2001. Deformation of strongly anisotropic materials. *J. Glaciol.*, **47**(158), 507-516.

Truffer, M. and A. Iken. 1998. The sliding velocity over a sinusoidal bed at high water pressure. *J. Glaciol.*, **44**(147), 379-382.

Truffer, M., K. Echelmeyer and W. D. Harrison. 2001. Implications of till deformation on glacier dynamics. *J. Glaciol.*, **47**(156), 123-134.

Tulaczyk, S., W. B. Kamb and H. F. Engelhardt. 2000a. Basal mechanics of Ice Stream B, West Antarctica, 1. Till mechanics. *J. Geophys. Res.*, **105**(B1), 463-481.

Tulaczyk, S., W. B. Kamb and H. F. Engelhardt. 2000b. Basal mechanics of Ice Stream B, West Antarctica, 2. Undrained plastic bed model. *J. Geophys. Res.*, **105**(B1), 483-494.

Vieli, A., M. Funk and H. Blatter. 2000. Tide water glaciers: frontal flow acceleration and basal sliding. *Ann. Glaciol.*, **31**, 217-221.

Vonmoos, M. 1999. Auswirkungen basaler Störungen auf das Geschwindigkeitsfeld und die Oberfläche eines Gletschers. (Diplomarbeit, Versuchsanstalt für Wasserbau Hydrologie und Glaziologie (VAW), ETH, Zürich.) (In German).

Weertman, J. 1957. On the sliding of glaciers. *J. Glaciol.*, **3**, 33-38.

Willis, I. C. 1995. Intra-annual variations in glacier motion: a review. *Prog. Phys. Geogr.*, **19**(1), 61-106.

Zienkiewicz, O. C. and R. L. Taylor 2000. *The finite element method. Fifth edition. vol. 1: The basis*, Butterworth-Heinemann, Oxford.

APPENDIX A

Strain Ellipse Calculation

Two dimensional surface strain on the glacier was analysed with the method described by Jaeger (1969). Assuming that the strain on a glacier surface is homogeneous within a limited area, the surface strain field is expressed by a linear transformation written as,

$$x' = ax + by, \qquad y' = cx + dy. \tag{A.1}$$

$(x,\ y)$ and $(x',\ y')$ are the coordinates before and after the transformation. To determine the four coefficients in Equation (A.1), three poles should be surveyed twice on the glacier. Taking a coordinate relative to one of the three poles, Equation (A.1) can be solved for the coefficients,

$$a = \frac{x'_2 y_1 - x'_1 y_2}{x_2 y_1 - x_1 y_2} \qquad b = \frac{x'_1 x_2 - x_1 x'_2}{x_2 y_1 - x_1 y_2} \qquad c = \frac{y_1 y'_2 - y'_1 y_2}{x_2 y_1 - x_1 y_2} \qquad d = \frac{x_2 y'_1 - x_1 y'_2}{x_2 y_1 - x_1 y_2}, \tag{A.2}$$

where $(x_1,\ y_1)$ and $(x_2,\ y_2)$ are the original positions of two poles relative to the reference pole, and $(x'_1,\ y'_1)$ and $(x'_2,\ y'_2)$ are the positions after the deformation.

Equations (A.1) are solved for x and y to have

$$x = \frac{dx' - by'}{h^2}, \qquad y = \frac{-cx' + ay'}{h^2} \tag{A.3}$$

$$h^2 = ad - bc. \tag{A.4}$$

A circle of unit radius,

$$x^2 + y^2 = 1, \tag{A.5}$$

is transformed by Equation (A.1) into an ellipse. The ellipse after the transformation is obtained by the substitutions of Equations (A.3) into Equation (A.5), and it results

$$\frac{c^2 + d^2}{h^4} x'^2 - \frac{2(ac + bd)}{h^4} x'y' + \frac{a^2 + b^2}{h^4} y'^2 = 1. \tag{A.6}$$

When the original circle is deformed under the strain field represented by Equation (A.1), the resulting ellipse is called the *strain ellipse.*

The directions of the axes of the ellipse, α and $\alpha + \pi/2$, are found from

$$\tan 2\alpha = \frac{2(ab+cd)}{a^2+c^2-b^2-d^2}. \tag{A.7}$$

The lengths of the axes are the solutions of the quadratic equation,

$$R^4 - (a^2+b^2+c^2+d^2)R^2 + h^4 = 0. \tag{A.8}$$

Writing two positive solutions as A and B ($A \geq B$), Equation (A.8) gives

$$A^2 + B^2 = a^2+b^2+c^2+d^2, \tag{A.9}$$

$$AB = h^2. \tag{A.10}$$

By using Equation (A.4), Equations (A.9) and (A.10) yield

$$(A+B)^2 = (a+b)^2 + (b-c)^2, \tag{A.11}$$

$$(A-B)^2 = (a-d)^2 + (b+c)^2. \tag{A.12}$$

The lengths of major and minor axes, A and B of the strain ellipse can be calculated from Equations (A.11) and (A.12). The change in surface area after the deformation is written as

$$\Delta S = \pi AB - \pi = \pi(h^2-1). \tag{A.13}$$

The quantity $h^2 - 1$ is called the *dilatation*, and h^2 is equivalent to the fraction of the areas before and after the deformation.

APPENDIX B

Stokes Equations

The numerical flow model used in this study is based on the steady state Stokes equations. Stokes equations are derived from the following procedure under the assumptions of material incompressibility, negligibly small Reynolds number, and steady state condition.

Taking $\mathbf{x} = (x_1, x_2)$ as two dimensional Cartesian coordinates, and t as a time variable, the equation of mass conservation is,

$$\frac{\partial \rho}{\partial t} + \frac{\partial \rho u_j}{\partial x_j} = 0. \tag{B.1}$$

ρ is the density of the material, $\mathbf{u} = (u_1, u_2)$ is the flow velocity vector, and the summation convention is employed. Momentum balance equation is,

$$\frac{\partial \rho u_i}{\partial t} + \frac{\rho u_i u_j}{\partial x_j} - \frac{\partial \sigma_{ij}}{\partial x_j} = \rho g_i, \tag{B.2}$$

where $\mathbf{g} = (g_1, g_2)$ is the gravitational force vector and

$$\sigma = \begin{pmatrix} \sigma_{11} & \sigma_{12} \\ \sigma_{21} & \sigma_{22} \end{pmatrix} \tag{B.3}$$

is the stress tensor. When the material is incompressible, the first term in Equation (B.1) is zero. The first term in Equation (B.2) (inertia term) is omitted due to the steady state condition, and the second term (advection term) is negligible when the Reynols number $R_e = UL/\nu = \rho UL/\mu$ is small. Here, U and L are the velocity and the length scales, μ and ν are the viscosity and the kinematic viscosity. Consequently, Equations (B.1) and (B.2) reduce to

$$\begin{aligned} -\frac{\partial \sigma_{ij}}{\partial x_j} &= \rho g_i & \text{(B.4)} \\ \frac{\partial u_j}{\partial x_j} &= 0. & \text{(B.5)} \end{aligned}$$

Equations (B.4) and (B.5) are Stokes equations in a steady state condition. In the case of an incompressible isotropic material, stress components are related to strain rate components with Equation (B.6).

$$\sigma_{ij} = -p\delta_{ij} + 2\mu D_{ij} \tag{B.6}$$

Here, the material is treated as a Newtonian fluid by taking a constant μ, but non-linear effects are introduced into the presented flow model by taking μ as a function of stress or strain components in the numerical scheme. p is the hydrostatic pressure, and $\mathbf{D}$ is the strain rate tensor defined by

$$D = \begin{pmatrix} D_{11} & D_{12} \\ D_{21} & D_{22} \end{pmatrix} \tag{B.7}$$

$$D_{ij}(\mathbf{u}) = \frac{1}{2}\left(\frac{\partial u_i}{\partial x_j} + \frac{\partial u_j}{\partial x_i}\right). \tag{B.8}$$

Equation (B.6) is substituted in Equation (B.4) to eliminate the stress components, and then the Stokes equations are expressed with velocity components and pressure as

$$\frac{\partial}{\partial x_j}(p\delta_{ij} - 2\mu D_{ij}) = \rho g_i \tag{B.9}$$

$$\frac{\partial u_j}{\partial x_j} = 0, \tag{B.10}$$

or in the explicit forms,

$$\frac{\partial p}{\partial x_1} - \mu\left(\frac{\partial^2 u_1}{\partial x_1^2} + \frac{\partial^2 u_1}{\partial x_2^2}\right) = \rho g_1 \tag{B.11}$$

$$\frac{\partial p}{\partial x_2} - \mu\left(\frac{\partial^2 u_2}{\partial x_1^2} + \frac{\partial^2 u_2}{\partial x_2^2}\right) = \rho g_2 \tag{B.12}$$

$$\frac{\partial u_1}{\partial x_1} + \frac{\partial u_2}{\partial x_2} = 0. \tag{B.13}$$

APPENDIX C

Finite-Element Method

To solve the Stokes equations, the finite-element method was employed. This method has an advantage to finite-difference scheme for its flexibility to use nonuniform grid spacings to focus on key areas, and to fit the mesh to irregular boundaries. There are several different techniques in each step of the finite-element method. In this study, linear and quadratic functions are used as the shape functions for pressure and velocity fields. Galerkin method was employed for discretization of the weighting functions. For the discretization of the field, triangle shaped finite elements were used. By showing the basis of the finite-element method briefly, the matrix to be solved is derived in the following.

C.1 Weak Form

A two dimensional field Ω is given and its boundary $\partial\Omega$ is divided into two regions, Γ_1 and Γ_2. At the boundary Γ_1, velocity $\mathbf{u} = (u_1, u_2)$ satisfies the condition of

$$u_i = \hat{u}_i. \tag{C.1}$$

At the boundary Γ_2, surface stress $\tau = (\tau_1, \tau_2)$ satisfies

$$\tau_i = \hat{\tau}_i \tag{C.2}$$

where the surface stress is a dot product of the stress tensor and the surface normal unit vector $\mathbf{n} = (n_1, n_2)$,

$$\tau_i = \sigma_{ij} n_j. \tag{C.3}$$

$\hat{\mathbf{u}} = (\hat{u}_1, \hat{u}_2)$ and $\hat{\tau} = (\hat{\tau}_1, \hat{\tau}_2)$ should be prescribed. The two types of boundary conditions, Equations (C.1) and (C.2), are called *essential* and *natural boundary conditions.*

Then, a steady state Stokes flow in the field Ω under the conditions of Equations (C.1) and (C.2) is considered. In the finite-element method, differential equations are transformed into integral forms so called *weak forms.* Equation (B.4) and (B.5) are integrated within the field Ω.

$$-\int_\Omega u_i^* \frac{\partial \sigma_{ij}}{\partial x_j} d\Omega = \int_\Omega g_i u_i^* d\Omega \tag{C.4}$$

$$\int_\Omega p^* \frac{\partial u_j}{\partial x_j} d\Omega = 0 \tag{C.5}$$

u_i^* and p^* are weighting functions. For functions f and g, Gauss-Green theorem is denoted as below.

$$\int_\Omega \frac{\partial f}{\partial x_i} g \, d\Omega = \int_{\partial\Omega} f g n_i \, d\Gamma - \int_\Omega f \frac{\partial g}{\partial x_i} d\Omega \tag{C.6}$$

Equation (C.6) is applied for Equation (C.5) and partial integration is operated.

$$\begin{aligned} -\int_\Omega u_i^* \frac{\partial \sigma_{ij}}{\partial x_j} d\Omega &= -\int_{\partial\Omega} \sigma_{ij} n_j u_i^* d\Gamma + \int_\Omega \frac{\partial u_i^*}{\partial x_j} \sigma_{ij} d\Omega \\ &= -\int_{\Gamma_2} \hat{\tau}_i u_i^* d\Gamma + \int_\Omega \frac{\partial u_i^*}{\partial x_j} \sigma_{ij} d\Omega \end{aligned} \tag{C.7}$$

Therefore,

$$\int_\Omega \frac{\partial u_i^*}{\partial x_j} \sigma_{ij} d\Omega = \int_\Omega g_i u_i^* d\Omega + \int_{\Gamma_2} \hat{\tau}_i u_i^* d\Gamma \tag{C.8}$$

Equation (B.6) is applied for the left hand side of Equation (C.8) to eliminate the stress components, and the equation

$$\frac{\partial u_i}{\partial x_j} D_{ij}(\mathbf{v}) = D_{ij}(\mathbf{u}) D_{ij}(\mathbf{v}) \tag{C.9}$$

is used to yield

$$2\nu \int_\Omega D_{ij}(\mathbf{u}^*) D_{ij}(\mathbf{u}) d\Omega - \int_\Omega \frac{\partial u_i^*}{\partial x_i} p d\Omega = \int_\Omega g_i u_i^* d\Omega + \int_{\Gamma_2} \hat{\tau}_i u_i^* d\Gamma. \tag{C.10}$$

Equation (C.10) is the weak form of the original problem of a Stokes flow. Equations (C.10) and (C.5) are solved for $\mathbf{u}$ and p under the conditions of Equations (C.1) and (C.2).

C.2 Finite-Element Approximation

Distribution of pressure p in the field is approximated with linear shape functions ψ_κ,

$$p = p_\kappa \psi_\kappa \tag{C.11}$$

where p_κ is the pressure value at each node and ψ_κ satisfies the following equation.

$$\psi_\kappa(R_\lambda) = \delta_{\kappa\lambda} \tag{C.12}$$

$R_1, ..., R_{N_p}$ represent the nodes at the corners of all elements in the field, and $\kappa = 1, ..., N_p$. For the velocity components, quadratic shape function, ϕ_α, satisfies the condition

$$\phi_\alpha(Q_\beta) = \delta_{\alpha\beta}. \tag{C.13}$$

$Q_1, ..., Q_{N_u}$ are all nodes in the field including those at the mid sides, and $\beta = 1, ..., N_u$. Flow velocity components are

$$u_i = u_{i\alpha}\phi_\alpha. \tag{C.14}$$

$i = 1, 2$ in the two dimensional case. Weighting function u_i^* and p^* are discretized by Galerkin method.

$$u_i^* = u_{i\alpha}^*\phi_\alpha \tag{C.15}$$

$$p^* = p_\kappa^*\psi_\kappa \tag{C.16}$$

Substitutions of Equations (C.11), (C.14), (C.15), and (C.16) in Equations (C.5) and (C.10) yield,

$$\begin{aligned} 2\nu \int_\Omega D_{kl}(u_{i\alpha}^*\phi_\alpha \mathbf{e}_i) D_{kl}(u_{j\beta}\phi_\beta \mathbf{e}_j) d\Omega - \int_\Omega \frac{\partial(u_{i\alpha}^*\phi_\alpha)}{\partial x_i}(p_\lambda\psi_\lambda) d\Omega \\ = \int_\Omega g_i(u_{i\alpha}^*\phi_\alpha) d\Omega + \int_{\Gamma_2} \hat{\tau}_i(u_{i\alpha}\phi_\alpha) d\Gamma, \end{aligned} \tag{C.17}$$

and

$$\int_\Omega (p_\kappa^*\psi_\kappa)\frac{\partial(u_{j\beta}\phi_\beta)}{\partial x_j} d\Omega = 0. \tag{C.18}$$

$\mathbf{e}_i$ is a unit vector. Since $u_{j\beta}$, p_λ, $u_{i\alpha}^*$, and p_κ^* are values at nodes but not variables, they can be excluded from the differentiation and integration.

$$u_{i\alpha}^* \left\{ 2\nu u_{j\beta} \int_\Omega D_{kl}(\phi_\alpha \mathbf{e}_i) D_{kl}(\phi_\beta \mathbf{e}_j) d\Omega - p_\lambda \int_\Omega \frac{\partial \phi_\alpha}{\partial x_i}\psi_\lambda d\Omega - \int_\Omega g_i\phi_\alpha d\Omega - \int_{\Gamma_2} \hat{\tau}_i\phi_\alpha d\Gamma \right\} = 0 \tag{C.19}$$

$$p_\kappa^* \left\{ u_{j\beta} \int_\Omega \psi_\kappa \frac{\partial \phi_\beta}{\partial x_j} d\Omega \right\} = 0 \tag{C.20}$$

In order to satisfy Equations (C.19) and (C.20) with any values of $u_{i\alpha}^*$ and p_κ^*, the inside of the brackets are zero. Thus,

$$2\nu u_{j\beta} \int_\Omega D_{kl}(\phi_\alpha \mathbf{e}_i) D_{kl}(\phi_\beta \mathbf{e}_j) d\Omega - p_\lambda \int_\Omega \frac{\partial \phi_\alpha}{\partial x_i}\psi_\lambda d\Omega = \int_\Omega g_i\phi_\alpha d\Omega + \int_{\Gamma_2} \hat{\tau}_i\phi_\alpha d\Gamma \tag{C.21}$$

$$u_{j\beta} \int_\Omega \psi_\kappa \frac{\partial \phi_\beta}{\partial x_j} d\Omega = 0. \tag{C.22}$$

Equations (C.22) and (C.22) are finite-element equations and they form a set of spontaneous linear equations. It is written in a matrix form as,

$$\begin{pmatrix} K^{ij}_{\alpha\beta} & C^{i}_{\lambda\alpha} \\ C^{j}_{\kappa\beta} & 0 \end{pmatrix} \begin{pmatrix} u_{j\beta} \\ p_{\lambda} \end{pmatrix} = \begin{pmatrix} \hat{\Omega}_{i\alpha} \\ 0 \end{pmatrix}. \tag{C.23}$$

$$K^{ij}_{\alpha\beta} = 2\nu \int_{\Omega} D_{kl}(\phi_\alpha \mathbf{e}_i) D_{kl}(\phi_\beta \mathbf{e}_j) d\Omega \tag{C.24}$$

$$C^{i}_{\lambda\alpha} = -\int_{\Omega} \frac{\partial \phi_\alpha}{\partial x_i} \psi_\lambda d\Omega \tag{C.25}$$

$$\hat{\Omega}_{i\alpha} = \int_{\Omega} g_i \phi_\alpha d\Omega + \int_{\Gamma_2} \hat{\tau}_i \phi_\alpha d\Gamma \tag{C.26}$$

This matrix (C.23) is solved numerically for the flow velocity and pressure fields, $u_{j\beta}$ and p_λ.

C.3 Calculation of Matrix Components

The components of the matrix (C.23) are calculated from Equations (C.24)–(C.26) by using area coordinates. A point $P(x_1, x_2)$ in one of the triangular elements $P_1P_2P_3$ is considered (Fig. C.1a). $P_1(x_1^1, x_2^1)$, $P_2(x_1^2, x_2^2)$, and $P_3(x_1^3, x_2^3)$ are nodes of the element taken counter-clockwise order. The area coordinates of the point $P(\xi_1, \xi_2, \xi_3)$ are defined by,

$$\xi_i = \frac{\triangle P P_j P_k}{\triangle P_1 P_2 P_3} \qquad (i, j, k) = (1, 2, 3), (2, 3, 1), (3, 1, 2) \tag{C.27}$$

$\triangle$ indicates the area of the triangle. Two basic rules are derived from Equation (C.27).

$$\xi_i(P_j) = \delta_{ij} \tag{C.28}$$

$$\xi_1 + \xi_2 + \xi_3 = 1 \tag{C.29}$$

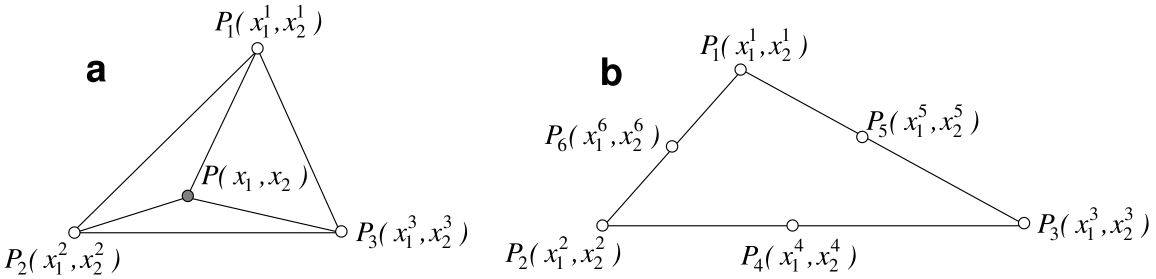

Figure C.1: *(a) The area coordinate system, and (b) the nodes of a quadratic triangular element.*

There are linear relationships between the area coordinates (ξ_1, ξ_2, ξ_3) and the Cartesian coordinates (x_1, x_2),

$$\xi_i = a_i + b_i x + c_i y \qquad (i,j,k) = (1,2,3), (2,3,1), (3,1,2). \tag{C.30}$$

Equations (C.28) and (C.30) give a set of simultaneous linear equations for a_i, b_i, and c_i when i is fixed, and the solutions are

$$\begin{aligned} a_i &= \frac{1}{2 \triangle P_1 P_2 P_3}(x_1^j x_2^k - x_1^k x_2^j) && \text{(C.31)} \\ b_i &= \frac{1}{2 \triangle P_1 P_2 P_3}(x_2^j - x_2^k) && \text{(C.32)} \\ c_i &= \frac{1}{2 \triangle P_1 P_2 P_3}(x_1^k - x_1^j) && \text{(C.33)} \\ (i,j,k) &= (1,2,3), (2,3,1), (3,1,2) \end{aligned}$$

The area of the triangular element is calculated from the coordinates of the corner nodes.

$$\triangle P_1 P_2 P_3 = \frac{1}{2}\{(x_1^2 - x_1^1)(x_2^3 - x_2^1) - (x_1^3 - x_1^1)(x_2^2 - x_2^1)\} \tag{C.34}$$

Thus, the area coordinates in an element are obtained from the Cartesian coordinates of the corner nodes of the element. From Equation (C.30), the derivatives of the area coordinates are

$$\frac{\partial \xi_i}{\partial x_1} = b_i, \qquad \frac{\partial \xi_i}{\partial x_2} = c_i, \tag{C.35}$$

and the integration of the polynomial of the area coordinates can be carried out with a convenient equation,

$$\int_{\Omega_e} \xi_1^i \, \xi_2^j \, \xi_3^k \, d\Omega = \frac{2\, i!\, j!\, k!\, \triangle P_1 P_2 P_3}{(2 + i + j + k)!}. \tag{C.36}$$

The area coordinates are also applied for the shape functions, ψ_κ and ϕ_α, to compute Equations (C.24)–(C.25). An element Ω_e and six nodes are taken as shown in Figure C.1b. This type of element is called a quadratic element, and the area coordinates of the nodes $P_1 - P_6$ are, $(1,0,0)$, $(0,1,0)$, $(0,0,1)$, $(1, 1/2, 1/2)$, $(1/2, 0, 1/2)$, $(1/2, 1/2, 0)$, respectively. The shape functions give unity at one of the nodes and zero at the others following the conditions written in Equations (C.13) and (C.12). Linear shape functions for the pressure is given with the area coordinates (Fig. C.2a).

$$\psi_i^e = A_1 \xi_1 + A_2 \xi_2 + A_3 \xi_3 \tag{C.37}$$

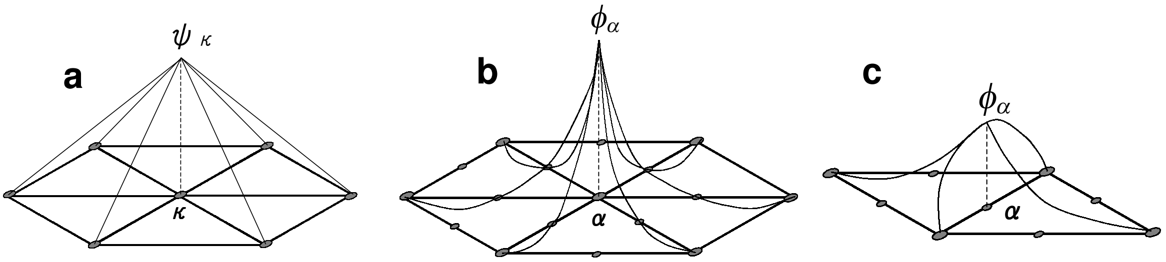

Figure C.2: *Shape functions used for pressure (a), and velocity (b and c).*

$$\begin{pmatrix} \psi_1^e \\ \psi_2^e \\ \psi_3^e \end{pmatrix} = \begin{pmatrix} 1 & 0 & 0 \\ 0 & 1 & 0 \\ 0 & 0 & 1 \end{pmatrix} \begin{pmatrix} \xi_1 \\ \xi_2 \\ \xi_3 \end{pmatrix}. \tag{C.38}$$

Their derivative forms are obtained from Equation (C.30),

$$\begin{aligned} &\frac{\partial \psi_1^e}{\partial x_1} = b_1, \quad \frac{\partial \psi_2^e}{\partial x_1} = b_2, \quad \frac{\partial \psi_3^e}{\partial x_1} = b_3 \\ &\frac{\partial \psi_1^e}{\partial x_2} = c_1, \quad \frac{\partial \psi_2^e}{\partial x_2} = c_2, \quad \frac{\partial \psi_3^e}{\partial x_2} = c_3 \end{aligned} \tag{C.39}$$

Quadratic shape functions are taken for velocity components (Figs. C.2b and c), and the functions and their derivatives are written as follows.

$$\phi_i^e = B_1\xi_1^2 + B_2\xi_2^2 + B_3\xi_3^2 + B_4\xi_2\xi_3 + B_5\xi_3\xi_1 + B_6\xi_1\xi_2 \tag{C.40}$$

$$\begin{pmatrix} \phi_1^e \\ \phi_2^e \\ \phi_3^e \\ \phi_4^e \\ \phi_5^e \\ \phi_6^e \end{pmatrix} = \begin{pmatrix} 1 & 0 & 0 & 0 & -1 & -1 \\ & 1 & 0 & -1 & 0 & -1 \\ & & 1 & -1 & -1 & 0 \\ & & & 4 & 0 & 0 \\ & 0 & & & 4 & 0 \\ & & & & & 4 \end{pmatrix} \begin{pmatrix} \xi_1^2 \\ \xi_2^2 \\ \xi_3^2 \\ \xi_2\xi_3 \\ \xi_3\xi_1 \\ \xi_1\xi_2 \end{pmatrix} \tag{C.41}$$

$$\begin{aligned} \frac{\partial \phi_1^e}{\partial x_1} &= (2b_1 - b_2 - b_3)\xi_1 - b_1\xi_2 - b_1\xi_3, & \frac{\partial \phi_1^e}{\partial x_2} &= (2c_1 - c_2 - c_3)\xi_1 - c_1\xi_2 - c_1\xi_3 \\ \frac{\partial \phi_2^e}{\partial x_1} &= -b_2\xi_1 + (-b_1 + 2b_2 - b_3)\xi_2 - b_2\xi_3, & \frac{\partial \phi_2^e}{\partial x_2} &= -c_2\xi_1 + (-c_1 + 2c_2 - c_3)\xi_2 - c_2\xi_3 \\ \frac{\partial \phi_3^e}{\partial x_1} &= -b_3\xi_1 - b_3\xi_2 + (-b_1 - b_2 + 2b_3)\xi_3, & \frac{\partial \phi_3^e}{\partial x_2} &= -c_3\xi_1 - c_3\xi_2 + (-c_1 - c_2 + 2c_3)\xi_3 \end{aligned}$$

$$\begin{aligned}
&\frac{\partial \phi_4^e}{\partial x_1} = 4b_3\xi_2 + 4b_2\xi_3, \quad \frac{\partial \phi_5^e}{\partial x_1} = 4b_3\xi_1 + 4b_1\xi_3, \quad \frac{\partial \phi_6^e}{\partial x_1} = 4b_2\xi_1 + 4b_1\xi_2 \\
&\frac{\partial \phi_4^e}{\partial x_2} = 4c_3\xi_2 + 4c_2\xi_3, \quad \frac{\partial \phi_5^e}{\partial x_2} = 4c_3\xi_1 + 4c_1\xi_3, \quad \frac{\partial \phi_6^e}{\partial x_2} = 4c_2\xi_1 + 4c_1\xi_2
\end{aligned} \tag{C.42}$$

All terms in Equations (C.24)–(C.25) are now written with the area coordinates ξ_i, and the integration can be carried out with Equation (C.36). Consequently, components of the matrix (C.23) are obtained for each element from the Cartesian coordinate of the corner nodes.

ACKNOWLEDGEMENTS

The author would like to express his gratitude to Professor Takeo Hondo, Chair of the doctoral degree Supervisory Committee, for the encouragement he provided this study. Appreciation goes to Dr. Renji Naruse, who supervised the author throughout the doctoral program, supported this research with frequent discussions, and guided the author in the right direction. Professor Heinz Blatter offered valuable assistance in the theoretical aspects of this work, and Professor Kazuomi Hirakawa encouraged the study and made important comments on the thesis.

Dr. G. Hilmar Gudmundsson, the leader of the field campaign on Unteraargletscher, provided the opportunity to collect all of the field data used in this thesis. He supported this work at every stage, from the measurements on the glacier to the theoretical investigations. Special thanks are also due to Jakob Helbing, who organised the field campaign and helped all activities on the glacier.

Dr. Takayuki Shiraiwa recommended the author join the Unteraar Project, and supported this study with valuable suggestions. For three years, the Glacier Research Group in the Institute of Low Temperature Science, Hokkaido University, was a supportive base for this study: Research plans were developed, many ideas acquired, and theories refined through discussions with group members.

Dr. Martin Funk and members of the Section of Glaciology, Laboratory of Hydraulics, Hydrology and Glaciology (VAW), at the Swiss Federal Institute of Technology (ETH), helped with measurements on the glacier and research work in Zurich, and with wonderful hospitality. Professor Atsumu Ohmura secured the stay at ETH and gave valuable comments on the thesis. Thanks are also due to Dr. Yaroslav D. Muravyev, Professor Tomomi Yamada, and all members of the research project at Koryto Glacier, Kamchatka, in 2000. Successful field measurements on Unteraargletscher were based on experience gained in Kamchatka.

Finally, the author wishes to dedicate this thesis to his most enthusiastic supporters: his parents, sisters and brothers, and Misako Kikuchi.

This study was funded by The Swiss National Science Foundation through grant No. 2100-063770.00 and by the Inoue Scientific Field Study Foundation.